

In vivo Mechanical Metrics for the Quantitative Assessment of Cartilage Health

by

Hattie Christine Cutcliffe

Department of Biomedical Engineering
Duke University

Date: _____

Approved:

Louis E. DeFrate, Advisor

Amy L. McNulty

Roger W. Nightingale

Adam P. Wax

Stefan Zauscher

Dissertation submitted in partial fulfillment of
the requirements for the degree of Doctor
of Philosophy in the Department of
Biomedical Engineering in the Graduate School
of Duke University

2019

ABSTRACT

In vivo Mechanical Metrics for the Quantitative Assessment of Cartilage Health

by

Hattie Christine Cutcliffe

Department of Biomedical Engineering
Duke University

Date: _____

Approved:

Louis E. DeFrate, Advisor

Amy L. McNulty

Roger W. Nightingale

Adam P. Wax

Stefan Zauscher

An abstract of a dissertation submitted in partial
fulfillment of the requirements for the degree
of Doctor of Philosophy in the Department of
Biomedical Engineering in the Graduate School of
Duke University

2019

Copyright by
Hattie Christine Cutcliffe
2019

Abstract

Osteoarthritis (OA) is a common joint disorder, affecting over 27 million Americans. OA is characterized by the degeneration of cartilage tissue, and presents clinically with joint pain, stiffness, and limited range of motion. As such, it is a leading cause of disability in the United States. Current treatment options for OA focus on relieving pain (either pharmacologically or through surgical joint replacement), but do not treat or reverse cartilage degeneration. A main reason for this is that the diagnosis of OA depends on pain and radiographic findings, which are not present until advanced OA. Development of therapies focused on treating or reversing OA degeneration would therefore be enhanced if OA pathology was detectable at earlier stages of the disease. Because changes in mechanical properties (i.e. the stiffness and permeability) occur in OA cartilage before pain and radiographic features are visible, measurement of cartilage mechanics may be used for earlier assessment of OA degeneration. As cartilage mechanics are traditionally measured in the ex vivo environment, the goal of this dissertation was to develop a noninvasive methodology for measuring cartilage mechanical properties in vivo.

Specifically, the methodology consists of a combination of noninvasive magnetic resonance imaging (MRI) techniques to quantify in vivo cartilage composition and mechanical response, as well as a statistical model predicting cartilage stiffness based on

these MRI measurements. Porcine knee joint cartilage was used to develop the statistical model, where stiffness was quantified in the traditional manner using ex vivo mechanical testing. The statistical model was then applied to in vivo data from a cohort of healthy human volunteers, for whom the noninvasive MRI techniques were used to measure the composition and mechanical response of their tibial cartilage. Thus, human tibial cartilage stiffness in vivo was quantified.

Overall, the in vivo estimates of healthy human tibial cartilage stiffness (ranging from 0.39 ± 0.05 MPa to 1.06 ± 0.24 MPa) compare well with ex vivo measurements of human cadaveric tibial cartilage stiffness (ranging from 0.45 ± 0.28 MPa to 0.65 ± 0.25 MPa). This finding supports the validity of the methodology developed in this dissertation. Future work using this in vivo methodology for measuring cartilage mechanical properties has diverse applications regarding cartilage health. For instance, this technique may be used clinically to provide earlier detection of OA pathology, or it may be used in future biomechanics research to evaluate the efficacy of different therapeutic approaches toward ameliorating OA pathology and restoring healthy cartilage mechanics. Therefore, the methodology for measuring cartilage mechanical properties in vivo developed here represents an important contribution to the fields of biomechanics and OA research.

Dedication

This dissertation is dedicated to my cherished family and boyfriend, as well as to any child whose love of sports ignites a passion for science. You can do hard things!

Contents

Abstract	iv
List of Tables.....	xii
List of Figures	xiii
Acknowledgements	xvi
1. Introduction	1
1.1 Motivation	1
1.2 Summary of Purpose.....	2
1.3 Specific Aims and Hypotheses	3
1.3.1 Specific Aim 1	3
1.3.1.1 Hypothesis 1	4
1.3.2 Specific Aim 2	5
1.3.2.1 Hypothesis 2	6
1.4 Novelty of Proposed Research	6
1.5 Dissertation Organization	9
2. Background.....	10
2.1 Cartilage Physiology	10
2.1.1 Cartilage Structure and Function.....	10
2.1.2 Chondrocyte Biology	15
2.2 Osteoarthritis.....	17
2.2.1 Epidemiology and Burden.....	17

2.2.2 Clinical Diagnosis and Treatment.....	18
2.2.3 Pathology	20
2.3 Mechanical Characterization of Cartilage Compressive Properties.....	21
2.3.1 Theoretical Framework.....	21
2.3.1.1 Introduction to Mechanical Characterization	21
2.3.1.2 Biphasic Modeling of Cartilage.....	27
2.3.1.3 Linear Biphasic Theory Governing Equations.....	29
2.3.1.4 Application of Linear Biphasic Theory Governing Equations to Confined Compression Creep	35
2.3.2 Experimental Methodologies.....	40
2.3.3 Mechanical Changes Seen in Osteoarthritis	45
2.4 Magnetic Resonance Imaging of Cartilage	46
2.4.1 Introduction to Magnetic Resonance Imaging.....	46
2.4.2 MRI for Cartilage Geometry Measurements	49
2.4.3 Quantitative MRI (T1rho and T2)	51
2.4.4 Imaging Changes Seen in Osteoarthritis.....	53
3. A New Stress Test for Knee Joint Cartilage.....	56
3.1 Introduction.....	56
3.2 Methods	59
3.2.1 Data Collection	59
3.2.2 Data Analysis.....	63
3.3 Results	67

3.4 Discussion.....	70
3.5 Conclusion.....	75
3.6 Acknowledgements.....	76
3.7 Paper Appendix.....	76
4. Comparison of Cartilage Mechanical Properties Measured During Creep and Recovery.....	79
4.1 Introduction.....	79
4.2 Methods	84
4.2.1 Mechanical Testing.....	84
4.2.2 Data Analysis	86
4.3 Results	88
4.4 Discussion.....	90
4.5 Conclusion.....	94
4.6 Acknowledgements.....	95
5. In Vivo Cartilage Strain and Recovery After 30 Minutes of Walking	96
5.1 Introduction.....	96
5.2 Methods	99
5.2.1 Data Collection	99
5.2.2 Data Analysis—DESS Scans.....	103
5.2.3 Data Analysis—T1rho and T2 Scans.....	106
5.2.4 Statistical Analysis.....	107
5.3 Results	107

5.4 Discussion.....	109
5.5 Conclusion.....	114
5.6 Acknowledgements.....	115
6. In vivo Estimation of Cartilage Stiffness using Noninvasive Imaging Metrics	116
6.1 Introduction.....	116
6.2 Methods	119
6.2.1 Sample Harvest and MRI	119
6.2.2 MRI Data Analysis	121
6.2.3 Mechanical Testing.....	123
6.2.4 Mechanical Testing Data Analysis.....	124
6.2.5 Statistical Analysis.....	125
6.3 Results	127
6.4 Discussion.....	132
6.5 Conclusion.....	142
6.6 Acknowledgements.....	142
7. Conclusion	144
7.1 Major Contributions.....	145
7.2. Future Work.....	147
Appendix A.....	148
Appendix B	150
Appendix C.....	157
Appendix D.....	159

Appendix E	160
References	171
Biography	187

List of Tables

Table 1: Reported Mechanical Properties of Healthy (non-OA) Cartilage.	44
Table 2: Pearson Correlation Coefficients Between Outcome Variables.....	89
Table 3: MRI Parameters.	101
Table 4: Parameter Estimates from a Multiple Linear Regression Predicting the Characteristic Recovery Time.....	109
Table 5: Literature Values of Human Cartilage Characteristic Creep Time.	110
Table 6: Parameter Estimates of Stiffness Regression Model from Healthy Cartilage Only Data Set (bold = $p < 0.05$).....	129
Table 7: Parameter Estimates of Stiffness Regression Model from Healthy and Degenerated Cartilage Data Set (bold = $p < 0.05$).	131
Table 8: Human Cartilage Mechanical Properties (mean \pm standard deviation).	137

List of Figures

Figure 1: Representative tibial cartilage thickness map.	10
Figure 2: Schematic of cartilage cross-section, showing varying collagen fiber orientation.	12
Figure 3: Schematic of cartilage cross-section, showing curling effect.....	14
Figure 4: Schematic of cartilage cross-section, showing varying chondrocyte morphology and distribution.....	15
Figure 5: Stress and strain response of an elastic material, represented as a spring.	23
Figure 6: Stress and strain response of a viscous material, represented as a dashpot.	24
Figure 7: Stress and strain response of a viscoelastic material, represented by a Maxwell model.	26
Figure 8: Stress and strain response of a viscoelastic material, represented by a Kelvin-Voigt model.	27
Figure 9: Illustration of the biphasic model of cartilage.....	28
Figure 10: Cartilage confined compression test setup (Mow et al., 1980).....	35
Figure 11: Comparison of cartilage compression testing methodologies.	41
Figure 12: Example of an MRI of the knee, illustrating visualization of various tissues within and around the joint.....	47
Figure 13: Diagram of hydrogen proton magnetization vector components during MRI acquisition.	49
Figure 14: 3D joint model creation from MRI (sagittal view, left knee).	64
Figure 15: Grid sampling scheme showing 18 grid points.....	65
Figure 16: Representative tibial cartilage thickness maps (superior-inferior perspective of axial view of left knee).....	68

Figure 17: Overall (a) and compartmental (b, c) compressive strain (mean, 95% confidence interval) in tibial cartilage as a function of walk duration.....	69
Figure 18: Overall (a) and compartmental (b, c) compressive strain (mean, 95% confidence interval) in tibial cartilage as a function of normalized walking speed (Fr). .	70
Figure 19: Saemix model diagnostics for the overall strain versus duration data.....	77
Figure 20: Saemix model diagnostics for the medial strain versus duration data.....	78
Figure 21: Saemix model diagnostics for the lateral strain versus duration data.....	78
Figure 22: Comparison of the loading and unloading (recovery) response of cartilage. .	83
Figure 23: Confined compression fixturing.....	85
Figure 24: Confined compression test battery.	86
Figure 25: Creep and recovery deformation response corridors (mean \pm 1 standard deviation) across all explants.	88
Figure 26: Pairwise differences in deformation response (creep minus recovery) at each point in time (mean \pm 1 standard deviation) across all explants.....	90
Figure 27: Study timeline for each subject (adapted from Heckelman et al., In Prep)....	101
Figure 28: Tibial cartilage thickness measurement procedure.	104
Figure 29: Grid sampling system used to define cartilage thickness in each model.....	105
Figure 30: Tibial cartilage strain (% , mean \pm 95% confidence interval) across time after activity, including a fit of the empirical Kelvin-Voigt model for recovery.	108
Figure 31: Bone and cartilage deficit measurement procedure.	122
Figure 32: Correlations between input variables and stiffness (healthy cartilage only data set).	128
Figure 33: Correlations between input variables and stiffness (healthy and degenerated cartilage data set).	130

Figure 34: Comparison of values from both data sets (healthy cartilage only, and healthy and degenerated cartilage data sets). 141

Acknowledgements

It goes without saying that the completion of this degree was only made possible by the support and encouragement, both personally and professionally, of numerous people in my life. First of all, I would like to gratefully acknowledge my advisor, Dr. Lou DeFrate, for his extensive teaching, guidance, and insight. Thank you, Lou, for believing in me even when I didn't believe in myself. I am immensely thankful for your unwavering positivity, encouragement, passion for science, and humorous nature. Thank you also for the opportunity to work and learn in your lab, for generously having your door open 24/7 and answering my countless questions, and for reminding me that it's called, "research," not, "search," for a reason.

Additionally, I am very appreciative of the many other mentors I have had throughout my time at Duke. Thank you to my PhD committee members, Dr. Amy McNulty, Dr. Roger Nightingale, Dr. Adam Wax, and Dr. Stefan Zauscher, for your invaluable input, direction, and thought-provoking questions about my research. I am very appreciative of each of your contributions to my development as a scientist and as a person, and am grateful for all of the counseling you provided. Likewise, I'm thankful to Bridgette Furman, the rest of the Orthopaedic Research Group, and Dr. Ken Gall for their help and support, especially as it relates to mechanical testing. We all know that the mechanical testing provided unanticipated challenges to overcome! Along those lines, I'd like to thank Dr. Jason Luck for the example he set regarding experimental

testing. Jason, you are a role model of mine for your painstaking attention to detail, methodical planning and execution of experimental procedures, and ability to lead a diverse group of researchers. Thank you for demonstrating that extra time devoted to set up, organization, and documentation can turn out to be time well spent.

Furthermore, I'm grateful to Dr. Charles Spritzer for his expertise in analyzing MR images. Thank you for your patience in checking over the (many) MRI scans I analyzed throughout this dissertation! I'm also grateful to Dr. Karin Brodin and the rest of the group at SAFER. I immensely enjoyed the professional and cultural development resulting from my time working with you in Sweden, and to this day appreciate the friendships and collaborations we made. Tak, Karin! I'd also like to give sincere thanks to Dr. Dale Bass, Dr. Bruce Capehart, and Dr. Barry Myers for their mentorship and instruction during my time in the Injury Biomechanics Lab. While working with you I learned so much about science but also about myself. Thank you for supporting me during a very difficult transition. Overall, I enjoyed working with and learning from each of you mentioned above and am so grateful for that.

Furthermore, I am indebted to my lab mates and friends for their camaraderie and collaboration in troubleshooting, problem solving, laughing, and ranting—basically, for their general support during this degree (#frustratedtoelated). I am so thankful to work with such a talented and caring group of people, who simultaneously push me to be my best. Dr. Amber Collins, Dr. Zoë Englander, Sophia Kim-Wang, Lauren

Heckelman, and Dr. John Martin: thank you for your endless encouragement and support! Additionally, despite our brief time working together, I'd like to thank Dr. Chinmay Paranjape, Lia Meirose, and Pavan Kottamasu for their collaboration and help in carrying out my project—it is very much appreciated. Similar thanks extend to the members of the Injury Biomechanics Lab (Jason Kait, Kyle Matthews, Dr. Garrett Wood, Dr. Rachel Lance, Dr. Jay Shridharani, Dr. Allison Schmidt, Dr. Allen You, Courtney Cox, Brian Bigler, Maria Ortiz Paparoni, and Anna Knight) for their friendship and collaboration. I am so thankful for our time learning and growing together.

Next, I am extremely grateful to several people outside of the professional realm for getting me to this point. To my best friends, Dr. Jenn Treacy, Lauren Hughes, and Dr. Holly Nichols—THANK YOU for always being there for me and knowing just what to say! You are each incredible role models to me and I'm immeasurably thankful for our friendship. Thank you to Faulkner's Dance and Gymnastics (Mich, Sue, and Mike Faulkner, and all the athletes I've had the honor of coaching) for allowing me to continue to use the gymnastics gym as an escape and to be involved in the sport I love.

Above all, I am infinitely grateful to my family for their unconditional love and support. Thank you to my parents, Brent Cutcliffe, Kim Lyon, and Scott Lyon, for investing so much time, energy, and resources into me, and most of all for your unwavering love. I would not be where I am or who I am today without you. Thank you to my brothers and sister-in-law, Rob, Sarah, Jeff, and Hunter, for always having my

back and for keeping our discussions lively and interesting from day one. Thank you to my precious nibblings Ole and Wells (#auntingsohard), and to William's precious nibblings Eymija'e, Sincere, Nasir, Amir, and Serenity (#parentinternship), for your infectious laughter and unceasing curiosity. Finally, a heartfelt thank you to my boyfriend, William Wright, for being a constant source of patience, reassurance, and joy. I am so grateful every day to have you in my life.

1. Introduction

1.1 Motivation

Osteoarthritis (OA) is a common joint disorder, affecting over 27 million Americans (Lawrence et al., 2008). OA is characterized by the degeneration of synovial joint tissue, with notable changes occurring in the cartilage, subchondral bone, and synovium (Loeser et al., 2012; Lorenz and Richter, 2006). OA presents clinically with symptoms of joint pain, stiffness, muscle weakness, and limited range of motion (Litwic et al., 2013). The diagnosis of OA is currently based on gross morphological changes visible via radiography, such as joint space narrowing and osteophyte formation, and on the presence of pain (Glyn-Jones et al., 2015; Litwic et al., 2013). As these features are not present until advanced stages of the disease (Litwic et al., 2013; Lorenz and Richter, 2006) when treatment options are limited (Glyn-Jones et al., 2015; Lorenz and Richter, 2006), quantitative assessment of the changes that occur in OA *prior* to the onset of pain is crucial for improved disease treatment and symptom management.

Before changes are visible on radiographs, compositional and morphological changes occur in cartilage tissue during the onset of OA (Loeser et al., 2012; Lorenz and Richter, 2006). These changes include decreases in proteoglycan content, disruption of the collagen matrix, changes in water content, and thinning of the cartilage (Hatcher et al., 2017; Hollander et al., 1995; Lorenz and Richter, 2006; Rivers et al., 2000; Thompson and Oegema, 1979). Consequently, the tissue's mechanical properties (stiffness and

permeability) and response to load are also altered during disease progression (Knecht et al., 2006; Mansour, 2003; Mow and Huijskes, 2005). As these compositional and mechanical changes take place prior to the development of pain, they may be useful as early markers of OA progression. Therefore, in vivo measurement of cartilage composition and mechanical properties may lead to earlier detection and diagnosis of OA.

1.2 Summary of Purpose

The primary goal of the proposed work is to quantify in vivo cartilage mechanical properties. Through the proposed research, a noninvasive technique using magnetic resonance imaging (MRI) measures of cartilage composition and mechanical response will be developed to assess cartilage mechanical properties in vivo, allowing for patient-specific monitoring of cartilage health and knee joint response to load. While this methodology may be used clinically for earlier detection of OA pathology in the future, the proposed work is focused on creating (Specific Aim 1) and validating (Specific Aim 2) this measurement technique in healthy cartilage only.

The measurement technique will consist of a statistical model predicting cartilage stiffness based on noninvasive imaging measures of cartilage composition and mechanical response to load. This model will be developed using porcine knee joint cartilage, under the assumption that the relationship between porcine cartilage stiffness and porcine imaging measures is the same as the relationship between human cartilage

stiffness and human imaging measures (though, importantly, it is not necessary or assumed that porcine cartilage stiffness is representative of human cartilage stiffness, or that porcine imaging metrics are representative of human imaging metrics). The developed statistical model will then be applied to imaging data collected from a group of healthy human volunteers, and the resulting measurements of in vivo cartilage mechanical properties will be compared to cadaveric measures of human cartilage mechanical properties.

1.3 Specific Aims and Hypotheses

1.3.1 Specific Aim 1

The goal of Specific Aim 1 is to develop a statistical model relating ex vivo measures of cartilage mechanical properties to MRI measures of joint health—specifically, to cartilage composition and deformation after functional loading. These MRI measures of joint health can be assessed noninvasively in vivo, so a statistical model relating these metrics to mechanical properties would allow for mechanical properties to be quantified in vivo.

Porcine cadaveric knee cartilage will be used for Specific Aim 1. Prior to explant harvest and mechanical testing, intact joints will undergo quantitative MRI to measure cartilage T1rho and T2 relaxation times. Both of these relaxation times correlate with the stiffness (aggregate modulus) and the composition (proteoglycan and collagen content) of the tissue (Collins et al., 2018a; Hatcher et al., 2017). Since softening and compositional

changes are known to occur in OA (Hollander et al., 1995; Setton et al., 1994; Thompson and Oegema, 1979), the T1rho and T2 relaxation times may be indicative of cartilage health. Next, cartilage explants will be harvested from the joints and will undergo mechanical testing. Specifically, cartilage structural properties (thickness, characteristic time) and mechanical properties (aggregate modulus) will be measured ex vivo via traditional creep and recovery confined compression experiments (Armstrong and Mow, 1982; Ateshian et al., 1997; Jurvelin et al., 2003). Because these four measures (T1rho relaxation time, T2 relaxation time, thickness, and characteristic time) can be quantified noninvasively in vivo using MRI (Paranjape et al., 2019; Taylor et al., 2009), they will be used as predictors in a multiple regression statistical model where the measured cartilage stiffness (specifically, the aggregate modulus) is the outcome variable. This model may then be used with noninvasive in vivo MR imaging of human subjects to quantify mechanical properties such as cartilage stiffness. Additionally, once the stiffness is known, the permeability may be calculated using the relationship between the permeability, stiffness, and characteristic time.

1.3.1.1 Hypothesis 1

MRI-based markers of cartilage composition and function are related to cartilage stiffness, and this relationship can be quantified via statistical modeling.

1.3.2 Specific Aim 2

The goal of Specific Aim 2 is to noninvasively assess human tibial cartilage mechanical properties in vivo. This will be accomplished by applying the statistical model developed in Aim 1 to normative in vivo data collected from healthy volunteers to quantify in vivo cartilage stiffness and permeability.

Following linear biphasic (poroelastic) theory (Armstrong and Mow, 1982; Mow and Huiskes, 2005; Mow et al., 1980), in vivo tibial cartilage structural properties (thickness, characteristic time) and material properties (aggregate modulus, permeability) will be assessed in healthy adult subjects. Quantitative MRI will be used to measure T1rho and T2 relaxation times, which are correlated with the aggregate modulus of the tissue and are indicative of cartilage composition (Collins et al., 2018a; Hatcher et al., 2017). Then, three-dimensional (3D) models of the tibia and tibial articular cartilage created from MRI will be used to measure cartilage thickness before and after a walking activity. Specifically, cartilage thickness will be measured at baseline (prior to walking) and at five time points after walking to capture recovery of cartilage thickness. A viscoelastic model will be fit to this thickness data to measure the tibial cartilage characteristic time, which is related to the aggregate modulus and permeability of the tissue under biphasic theory (Mow and Huiskes, 2005; Mow et al., 1980). Using the statistical model developed in Specific Aim 1, the aggregate modulus of the tissue in vivo will be quantified. With the characteristic time and aggregate modulus known, the

permeability will then be calculated (Armstrong and Mow, 1982; Mow et al., 1980), enabling the measurement of cartilage mechanical properties in vivo. Finally, these in vivo measurements will be compared with literature values of human cadaveric cartilage mechanical properties quantified using traditional ex vivo mechanical testing techniques (Akizuki et al., 1986a; Treppo et al., 2000).

1.3.2.1 Hypothesis 2

In vivo cartilage mechanical properties (MRI-derived stiffness and permeability measurements) can be quantified using this methodology, and will yield similar results to literature values of human cadaveric knee cartilage stiffness and permeability measured via traditional ex vivo mechanical testing techniques.

1.4 Novelty of Proposed Research

Because changes in cartilage mechanical response occur with increasing OA progression (Collins et al., 2018a; Hatcher et al., 2017; Rivers et al., 2000), measuring these changes may allow for earlier detection of OA pathology. However, current methods for measuring cartilage mechanical properties rely on ex vivo testing (Guo et al., 2003; Mow and Guo, 2002; Mow and Huiskes, 2005), which have limited applicability in the assessment of live human patients. Alternately, previous studies have shown a relationship between emerging quantitative MRI techniques (T1rho and T2 mapping), cartilage composition, and cartilage aggregate modulus (Collins et al., 2018a), suggesting that these measures capture information regarding cartilage health and mechanical

function. Likewise, changes in cartilage thickness over time as a result of activity can be measured in vivo using a combination of pre- and post-activity MRI (Coleman et al., 2013; Paranjape et al., 2019; Sutter et al., 2015; Van de Velde et al., 2009). This technique enables measurement of cartilage deformation and recovery in response to functional loading, and provides a manner in which to quantify the mechanical response of the tissue. The proposed work provides a novel combination of these imaging methodologies to noninvasively determine mechanical properties (both the aggregate modulus and permeability) of cartilage in vivo, which has never been done before. Because cartilage loading has been shown to affect chondrocyte metabolism and homeostasis (Guilak, 2011; Guilak et al., 1995), the proposed in vivo assessment of mechanical properties will improve the understanding of tissue function under healthy and/or pathological conditions. As mechanical properties change with disease (Hatcher et al., 2017; Mansour, 2003) and injury (Setton et al., 1994), the proposed methods may be used to detect OA pathology earlier than currently available clinical techniques such as radiography.

Moreover, walking or other physical exercise is commonly recommended to OA patients to reduce pain (Focht, 2006). As mechanical loading influences chondrocyte metabolism (Guilak, 2011; Loeser et al., 2012; Sah et al., 1989), specific levels of in vivo loading (exercise) may promote cartilage health and repair (Sun, 2010). The proposed methodology provides a manner in which to measure cartilage response to various

types of exercise, and quantify how that response may change in healthy versus OA cartilage with repeated bouts of exercise or training. Importantly, the proposed technique brings together multiple metrics of cartilage function to provide a robust understanding of joint health, including morphological measures (cartilage thickness), measures of composition (T1rho and T2 imaging), as well as mechanical measures (aggregate modulus and permeability). Applying this technique to both healthy and degenerated cartilage would help determine how much exercise therapy to prescribe to OA patients, as well as shed light into how much training is detrimental to cartilage health.

Overall, the proposed research details a novel combination of imaging methodologies to noninvasively quantify in vivo cartilage mechanical properties. This technique may be used clinically to provide in vivo measurements of knee joint health and may provide earlier detection of joint dysfunction or OA pathology. Additionally, the proposed technique can be used in future biomechanics research to shed further insight into the progression of OA by comparing how knee joint health changes in specific subpopulations (e.g. aging, obese, those with joint injury) that have an increased risk of OA. Lastly, the proposed methods can be used in future work to investigate the efficacy of different therapeutic approaches, such as exercise, towards ameliorating or reversing OA pathology.

1.5 Dissertation Organization

This dissertation is organized as a collection of several academic journal articles. In addition to the Introduction, Background, and Conclusions chapters, a single chapter is devoted to each journal article in this dissertation. The first of these (Section 3. A New Stress Test for Knee Joint Cartilage) is published (Paranjape et al., 2019). The second of these (Section 4. Comparison of Cartilage Mechanical Properties Measured During Creep and Recovery) is currently under review. The remaining two (Section 5. In Vivo Cartilage Strain and Recovery After 30 Minutes of Walking and Section 6. In vivo Estimation of Cartilage Stiffness using Noninvasive Imaging Metrics) are in progress towards submission.

2. Background

2.1 Cartilage Physiology

2.1.1 Cartilage Structure and Function

Hyaline cartilage is a connective tissue found on the articular surfaces of bones comprising synovial joints (Mow and Huiskes, 2005). In this capacity, hyaline cartilage supports joint motion by aiding in load transmission through minimizing contact stresses and creating a smooth surface between articulating bones (Sophia Fox et al., 2009). For example, hyaline cartilage (subsequently referred to as, “cartilage,”) is found on the distal end of the femur and the proximal end of the tibia in the knee joint. In healthy adult humans, femoral and tibial cartilage is typically 2-4 mm thick (Akizuki et al., 1986a; Coleman et al., 2013; Lad et al., 2016; Sophia Fox et al., 2009), though the thickness is not constant but varies across the surface of each bone (Figure 1).

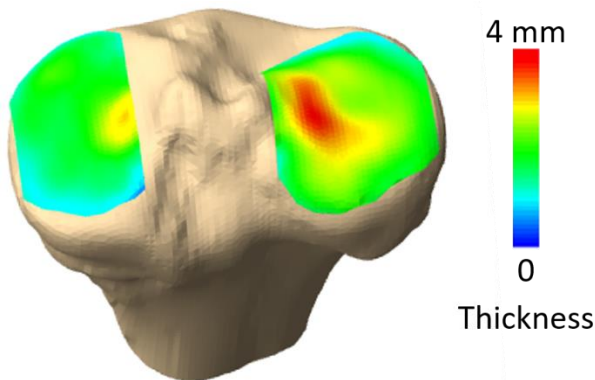


Figure 1: Representative tibial cartilage thickness map. Cartilage thickness is not constant but varies across the surface of the proximal tibia. Red indicates thicker cartilage while blue indicates thinner cartilage.

Cartilage consists of an extracellular matrix (ECM) and chondrocytes, the cells within the cartilage. The ECM is composed mainly of water, collagen, and proteoglycan (PG) molecules (Guo et al., 2003; Mow and Huiskes, 2005; Sophia Fox et al., 2009). Specifically, water accounts for 70-85% of the wet weight of the tissue, while collagen accounts for 10-20% and PG accounts for 5-10% of the wet weight (Mow and Huiskes, 2005). The collagen fibers form a highly interconnected matrix within which the PG molecules spread out and become trapped (Guo et al., 2003). The arrangement of these constituents gives rise to the mechanical function of cartilage: the collagen network resists shear and tensile forces, while the negatively charged PG molecules retain water within the tissue to resist compression (Mow and Huiskes, 2005).

The collagen fiber network of the ECM is composed primarily of type II collagen, with other minor collagens present to help stabilize the type II network (Mow and Huiskes, 2005). This network is highly organized, made up of fibers whose orientation varies throughout the depth of the cartilage tissue, leading to several distinct structural zones (Figure 2). In the superficial tangential zone—the ~10-20% of the cartilage nearest the articular surface—the collagen fibers are oriented parallel to the articular surface (Mow and Huiskes, 2005; Sophia Fox et al., 2009). Conversely, collagen fibers within the deep zone—the ~30% of the cartilage nearest the subchondral bone surface—are oriented perpendicularly to the bone (Mow and Huiskes, 2005; Sophia Fox et al., 2009). In between the superficial tangential and deep zones is the aptly-named middle

transitional zone, where collagen fiber orientation is more random and transitions between the perpendicular arrangement of the deep zone and the parallel alignment of the superficial tangential zone (Mow and Huiskes, 2005; Sophia Fox et al., 2009). The varying orientation of collagen fibers throughout the depth of the ECM allows cartilage to resist both tensile and shear forces (Mow and Huiskes, 2005). Further, the collagen fiber network traps and constrains the PG molecules within the cartilage tissue (Guo et al., 2003).

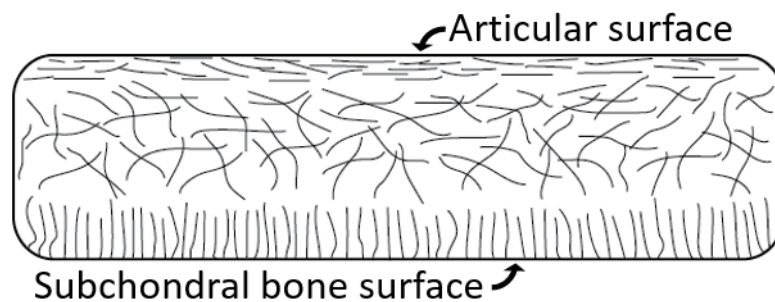


Figure 2: Schematic of cartilage cross-section, showing varying collagen fiber orientation. Collagen fibers are oriented parallel to the articular surface and perpendicular to the subchondral bone surface.

Proteoglycan molecules are large, bottle brush-like structures composed of a central core protein with numerous glycosaminoglycan chains (GAGs) attached (Mow and Huiskes, 2005; Sophia Fox et al., 2009). Aggrecan is the most abundant PG molecule in cartilage, and is formed between a core protein and the GAGs chondroitin sulfate and keratan sulfate (Mow and Huiskes, 2005; Sophia Fox et al., 2009). Furthermore, PGs such as aggrecan attach to hyaluronan molecules via link proteins to form large PG

aggregates (Mow and Huiskes, 2005; Sophia Fox et al., 2009). GAGs are anionic, and due to the electrostatic repulsion between mutual negative charges cause PGs and larger PG aggregates to spread out within the interfibrillar space of the ECM (Mow and Huiskes, 2005; Sophia Fox et al., 2009). Additionally, the anionic nature of PGs functions to draw water into the tissue via Donnan osmotic pressure (Mow and Huiskes, 2005): the numerous negatively charged GAGs attract positively charged counterions to maintain electroneutrality; this in turn draws water into the tissue to balance the ion concentration between the tissue and the surrounding fluid (Mow and Huiskes, 2005). Indeed, several mobile ions such as potassium, sodium, and calcium are present in the water within cartilage (Guo et al., 2003; Sophia Fox et al., 2009).

In addition to the collagen fiber orientation varying throughout the depth of the tissue, the concentration of constituents (collagen, PG, and water) varies throughout the depth of the tissue as well (Guo et al., 2003; Mow and Huiskes, 2005): the collagen content is highest near the articular surface of the cartilage, decreases in the middle transitional zone, and is lowest in the deep zone. The water content of cartilage follows that of collagen, with the surface zone having the highest content and the deep zone having the lowest water content (Guo et al., 2003; Mow and Huiskes, 2005). Conversely, the PG concentration is lowest near the articular surface of the cartilage and is higher in the middle and deep zones (Guo et al., 2003; Mow and Huiskes, 2005). This variation in both collagen and PG content leads to non-uniform swelling in a cartilage explant (a

piece of cartilage that has been cut out of the native tissue) when placed in an external solution (Guo et al., 2003; Mow and Huiskes, 2005) (Figure 3). PGs tend to spread out due to electrostatic repulsion of negative charges when the confining collagen network is compromised upon removal of the explant from the tissue (Guo et al., 2003; Mow and Huiskes, 2005). This uneven swelling is termed, “curling,” and occurs because the deep zone (that near the bone) of the explant swells more than the superficial zone of the explant. The swelling is uneven for two reasons: 1) the parallel arrangement of collagen fibers at the articular surface provides more tensile resistance to expansion than does the perpendicular arrangement of fibers at the deep surface, and 2) the relatively higher PG concentrations in the middle and deep layers contribute to more swelling compared to the surface layer of the cartilage with the lowest PG concentration.

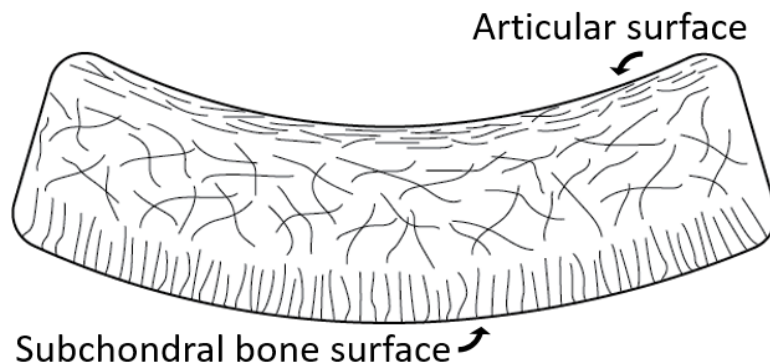


Figure 3: Schematic of cartilage cross-section, showing curling effect. Curling results from uneven swelling due to variation in collagen orientation and proteoglycan content with depth from the articular surface.

2.1.2 Chondrocyte Biology

Chondrocytes are the only type of cell present in mature cartilage (Mow and Huiskes, 2005; Sophia Fox et al., 2009). These cells are sparsely distributed throughout the tissue, and constitute less than 10% of the total volume of cartilage (Mow and Huiskes, 2005; Sophia Fox et al., 2009). Their morphology and distribution varies throughout cartilage depth (Figure 4): in the superficial tangential zone, the density of chondrocytes is highest and the cells exhibit a flat morphology (Mow and Huiskes, 2005). In the middle and deep zones, the density of the cells is lower and their shape is more spherical (Mow and Huiskes, 2005). Additionally, chondrocytes in the deep zone are oriented in vertical columns (Mow and Huiskes, 2005), similar to the collagen fiber orientation.

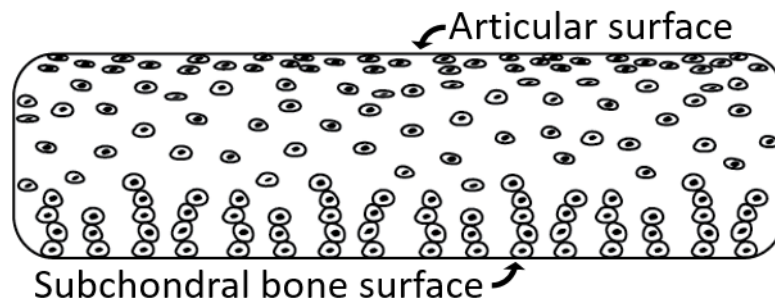


Figure 4: Schematic of cartilage cross-section, showing varying chondrocyte morphology and distribution.

The function of chondrocytes is to preserve tissue homeostasis by maintaining ECM turnover (Mow and Huiskes, 2005). A healthy chondrocyte metabolism includes both the synthesis and breakdown of ECM constituents (Guilak, 2011). As they lay down

matrix components directly around themselves, chondrocytes become immobilized within the ECM (Sophia Fox et al., 2009). Thus, each cell is responsible for maintaining matrix integrity in areas adjacent to it; areas further from a particular cell must depend on other, nearer cells for ECM turnover (Sophia Fox et al., 2009). Furthermore, cartilage tissue is aneural, avascular, and lacks a lymphatic system (Mow and Huiskes, 2005; Sophia Fox et al., 2009). Therefore, the cells rely on diffusion through the surrounding tissue and synovium for nutrient and waste transport, as well as for transport of ECM constituents (Sophia Fox et al., 2009). As a result, cartilage tissue is thought to have a low regenerative capacity (Lorenz and Richter, 2006; Mow and Huiskes, 2005; Sophia Fox et al., 2009).

Though chondrocytes are immobile and relatively isolated, they respond to several different types of stimuli, such as growth factors and cytokines, which can regulate chondrocyte metabolism and thus ECM turnover (Mow and Huiskes, 2005). Importantly, chondrocytes are also mechanically sensitive, with changes in the mechanical loading of the tissue leading to changes in the cells' metabolic activity (Guilak, 2011; Loeser et al., 2012; Sun, 2010). Using in vitro cartilage explants, increased GAG and protein synthesis (chondrocyte anabolism) has been observed following cyclic or dynamic compression of cartilage (Sah et al., 1989). Increased biosynthesis has also been observed in response to dynamic loading in chondrocytes seeded within both agarose (Buschmann et al., 1995; Lee and Bader, 1997; Shelton et al., 2003) and within

tissue-engineered cartilage constructs (Mauck et al., 2000). On the other hand, decreased biosynthesis has been observed in response to static loading in vitro, both in chondrocytes seeded within agarose (Buschmann et al., 1995) and in cartilage explants (Larsson et al., 1991; Sah et al., 1989). These observations demonstrate that chondrocytes respond to mechanical stimuli, and that changes in mechanical loading result in changes in chondrocyte metabolism and ECM turnover (Guilak, 2011; Loeser et al., 2012; Sun, 2010). Therefore, the mechanical environment experienced by the chondrocytes may be an important regulator of cartilage maintenance and health (Guilak, 2011).

2.2 Osteoarthritis

2.2.1 Epidemiology and Burden

Osteoarthritis (OA) is a debilitating joint disorder that is associated with the degeneration of articular cartilage, subchondral bone, and synovial tissue (Guilak, 2011; Litwic et al., 2013; Salaffi et al., 2005). OA affects over 27 million people—or 10% of adults—in the United States (Lawrence et al., 2008), and is among the top ten leading causes of disability in Americans (Michaud et al., 2006). Clinical symptoms of OA include joint pain, stiffness, and limited range of motion (Litwic et al., 2013), making activities of daily living difficult and affecting overall quality of life (Salaffi et al., 2005). Treatment options for OA are limited, and consist of pain management or total joint reconstruction surgery for end-stage disease (Glyn-Jones et al., 2015). These surgeries incur a large economic cost. For example, knee and hip replacements alone cost the US

\$42 billion in 2009 (Murphy and Helmick, 2012). Further, OA risk is increased in the aging population, those with obesity, and those with prior joint injury (such as anterior cruciate ligament injury) (Litwic et al., 2013). With age, the prevalence of knee OA more than doubles over a 35 year period, increasing from 19% in adults over 45 years to 44% in adults over 80 years (Litwic et al., 2013). Likewise, obesity increases the overall lifetime risk of OA from 50% to nearly 65% (Murphy et al., 2008). Overall, due to the projected increase in OA-related hospital visits (Murphy and Helmick, 2012), OA remains a significant clinical problem.

2.2.2 Clinical Diagnosis and Treatment

Currently, the diagnosis of OA is based on the existence of pain and radiographic features such as joint space narrowing (from which cartilage thinning is inferred) and the presence of osteophytes (Glyn-Jones et al., 2015; Litwic et al., 2013). However, these findings are only present in advanced stages of the disease (Li et al., 2007; Litwic et al., 2013) when cartilage degeneration is difficult to treat or reverse (Glyn-Jones et al., 2015). This is partly because the repair capacity of cartilage tissue is low, with native repair only possible for small defects in which a majority of the matrix constituents are still present (Lorenz and Richter, 2006).

Commonly, patients with knee OA experience weakness of the quadriceps femoris muscle (Lewek et al., 2004; Slemenda et al., 1997). As quadriceps strength is a major determinant of function and pain in knee OA (Aaboe et al., 2014; Berger et al.,

2012; O'Reilly et al., 1998), rehabilitation strategies often focus on improving its strength (Aaboe et al., 2014; Hurley and Scott, 1998; Maurer et al., 1999). However, these interventions are focused on reducing pain and improving function, and do not actually reverse or slow cartilage degeneration. Additionally, physical activity such as walking is often recommended to maintain cartilage health and reduce pain (Focht, 2006; Glyn-Jones et al., 2015). Exercise may even slow the progression of OA, as ex vivo and animal studies have shown that cartilage metabolism is influenced by its mechanical loading (Guilak, 2011; Guilak et al., 1995; Sah et al., 1989; Sun, 2010). However, the appropriate exercise intensity, duration, and frequency cannot currently be prescribed because direct in vivo evaluation of the response of pre-OA or OA cartilage to exercise has not yet been performed. Further, it is unknown at what stage during OA progression that exercise may improve or repair damaged cartilage, if at all.

For advanced stages of disease or for patients who don't experience pain relief after nonsurgical interventions (Beswick et al., 2012; Van Manen et al., 2012), surgical options exist. These procedures are either aimed at repairing cartilage lesions or replacing the diseased joint completely through knee arthroplasty. One method for lesion repair is microfracture, in which the exposed subchondral bone in a cartilage defect is punctured to stimulate bleeding and the eventual formation of a blood clot (Alford and Cole, 2005b). Microfracture typically results in the formation of fibrocartilage (as opposed to hyaline cartilage) within the defect (Alford and Cole,

2005b). Another method is an osteochondral transplant, in which a plug of bone and cartilage is harvested either from a cadaveric donor or from another location in the patient's body and then placed within the cartilage defect (Alford and Cole, 2005a, b). Finally, knee arthroplasty (total knee replacement) involves removing the articulating surfaces of the femur and tibia and replacing them with metal implants and a polyethylene spacer (Callaghan et al., 2000). In this manner, all of the cartilage within the tibiofemoral joint is completely removed. While these surgeries are beneficial, persistent pain following knee arthroplasty is a common outcome, with reported prevalence ranging between 10% to 34% (Beswick et al., 2012).

Overall, current treatments for OA focus on managing the disease through reducing pain and/or improving functional ability (Focht, 2006), but do not actually ameliorate or reverse tissue degeneration (Glyn-Jones et al., 2015). Thus, earlier diagnosis of OA and strategies for disease prevention and treatment would be improved if signs and symptoms of pre-OA or early OA could be quantified in vivo (Li et al., 2007). Detection of functional and degenerative changes associated with OA, prior to advanced stages of OA or the onset of pain, is critical for effective disease management.

2.2.3 Pathology

In addition to gross morphological changes visible on radiology, the development of OA is associated with compositional changes within the cartilage (Loeser et al., 2012; Yuan et al., 2014). Normal chondrocyte function includes a slow

turnover of cartilage constituents (type II collagen and proteoglycan), in which the ECM is maintained through a balance of anabolic and catabolic processes (Guilak, 2011). OA pathology results when this homeostasis is disrupted (Guilak, 2011; Loeser et al., 2012), leading to compositional changes within the tissue (Lorenz and Richter, 2006). These changes include decreases in PG content (Hatcher et al., 2017; Rivers et al., 2000; Roberts et al., 1986; Thompson and Oegema, 1979), changes in collagen organization (Hatcher et al., 2017; Hollander et al., 1995), and changes in water content (Hatcher et al., 2017; Rivers et al., 2000). Unfortunately, these pathological changes in cartilage composition are not detectable with current clinical diagnostic tools (Lorenz and Richter, 2006), as the presence of pain and radiological findings (i.e. joint space narrowing, osteophyte formation) remain the gold standard for OA diagnosis (Glyn-Jones et al., 2015; Litwic et al., 2013). Thus, diagnosis and treatment of OA may be improved if noninvasive measures of cartilage composition were available, as changes in cartilage composition may serve as early indicators of OA initiation or progression.

2.3 Mechanical Characterization of Cartilage Compressive Properties

2.3.1 Theoretical Framework

2.3.1.1 Introduction to Mechanical Characterization

How an entity responds to an external load depends on its characteristics, such as the type of material(s) constituting the entity as well as its geometry (size and shape) (Lai et al., 1999). In general, mechanical characterization of an object is the process by

which the factors affecting its response, collectively termed the mechanical properties, are described mathematically. Mechanical characterization of an entity typically involves three steps: 1) choosing an appropriate constitutive relation, 2) applying an external stimulus (i.e. a force) to the object and measuring its subsequent response (i.e. a displacement), and 3) curve-fitting the chosen constitutive relation to the measured response to quantify the mechanical properties (Lai et al., 1999). The constitutive relation defines the expected relationship between the external load and the object's response (typically in terms of stress, $\sigma(t)$, and strain, $\epsilon(t)$). In general, stress is the force acting on an object normalized to the area across which it acts, and strain is the deformation of an object normalized to its original dimensions (Mow and Huiskes, 2005). There are numerous types of constitutive relations which can be broadly classified as elastic, viscous, or viscoelastic (Lai et al., 1999).

The elastic model is the simplest constitutive relation. It predicts that stress and strain are linearly related, and do not change with time or the rate of application (Lai et al., 1999) (Figure 5). This relation is commonly conceptualized via a mechanical spring, and can be used to describe solid materials.

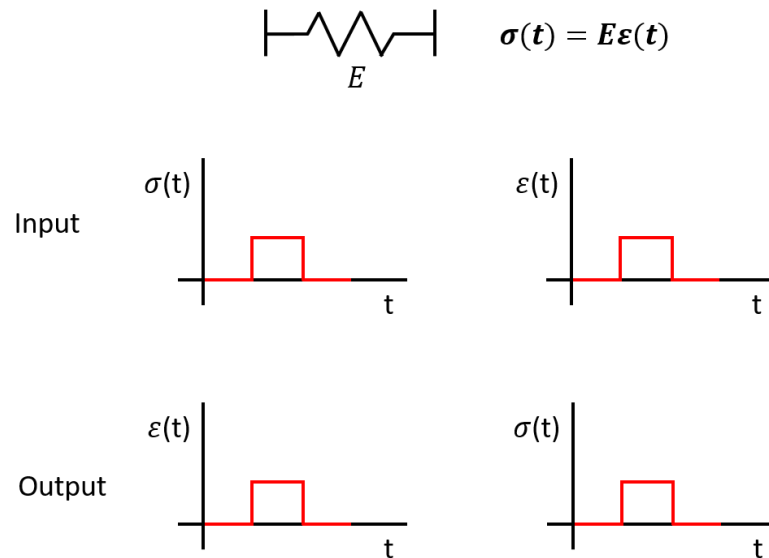


Figure 5: Stress and strain response of an elastic material, represented as a spring.

In both the creep experiment (where a step stress is applied and the strain is measured) and the stress relaxation experiment (where a step strain is applied and the stress is measured), the spring's response is constant across time and is linearly proportional to the constant input. When the input is removed, the response returns to zero—in other words, there is no permanent deformation within the spring, and it returns to its original state. The stiffness or the spring constant, E , is the single mechanical property incorporated in the elastic constitutive relation. It describes the constant ratio of the stress to the strain, and by measuring the applied stress and corresponding strain (or vice versa) and fitting a line to this stress versus strain data, the mechanical property E can be determined as the slope of the fitted line. While the elastic constitutive relation is extremely useful, many biological materials (like cartilage) do not

exhibit responses that are constant across time even when the input is constant, nor result in stress-strain curves that are linear.

The viscous model is another important constitutive relation, in which the stress is linearly related to the strain rate (the time rate of change of strain) (Lai et al., 1999) (Figure 6). This relation is conceptualized mechanically by a dashpot—a piston filled with liquid—and can be used to describe fluids.

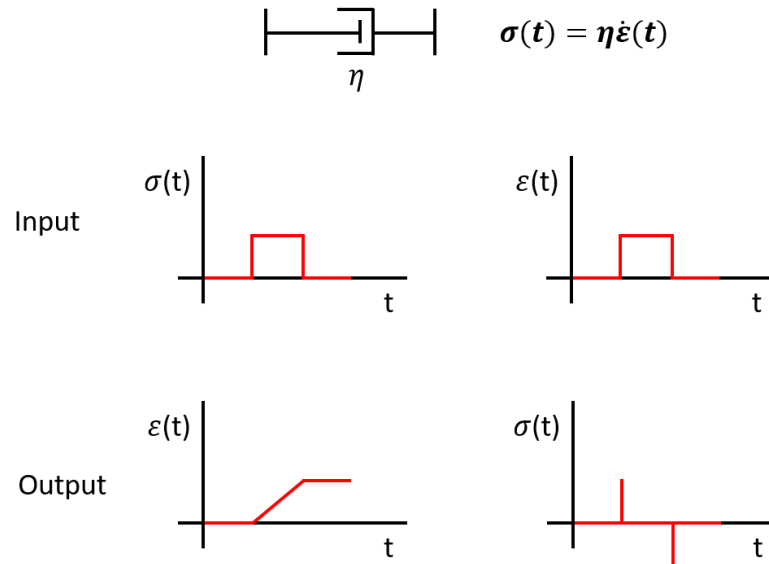


Figure 6: Stress and strain response of a viscous material, represented as a dashpot.

Unlike the spring, where the strain returns to zero when the stress input is removed during a creep experiment, a dashpot doesn't return to its original state when the stress input is removed. Additionally, the dashpot only develops a stress in response to a strain rate, and therefore it experiences infinite stress at the moment the step strain is applied (or removed), but experiences zero stress while the strain is held constant.

Like the elastic relation, the viscous relation is highly useful but is unable to predict the behavior exhibited by many biological materials (such as cartilage) during creep and stress relaxation experiments.

A third type of constitutive relationship is the viscoelastic (VE) one, used to describe materials that demonstrate some aspects of both viscous and elastic responses (Cowin and Doty, 2007). There are numerous constitutive relationships that can describe materials that display both solid-like and fluid-like behavior. These materials typically display time dependence, in that their strain changes nonlinearly over time in response to a constant applied stress (and vice versa). They may also exhibit different responses when the strain rate, loading rate, or temperature is varied. Biological materials, such as cartilage, often display VE behavior. Simple VE relations such as the Maxwell (Figure 7) and Kelvin-Voigt (Figure 8) models can be conceptualized mechanically by the combination of a spring and a dashpot, with more complicated relations including additional elements (springs or dashpots) in various orientations (Cowin and Doty, 2007).

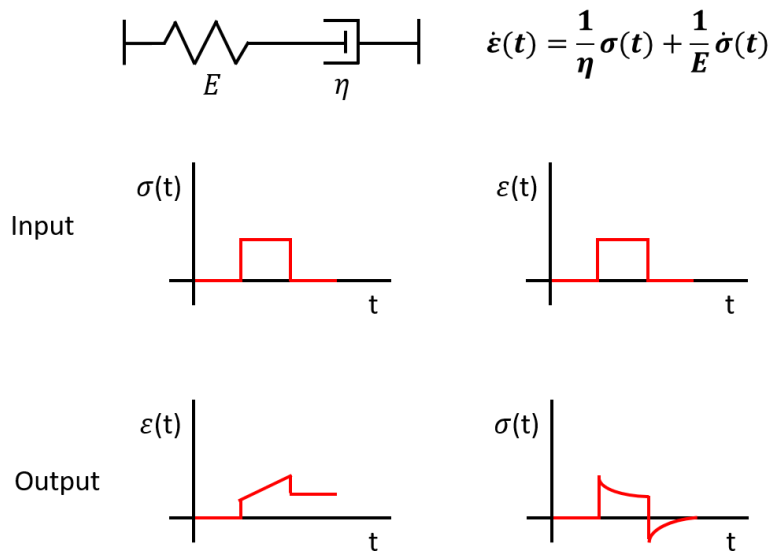


Figure 7: Stress and strain response of a viscoelastic material, represented by a Maxwell model.

In the Maxwell model (Figure 7), the spring and dashpot are in series. This model is useful for modeling fluid-like VE material behavior, because during stress relaxation, this model's stress response decays to zero. However, it is less useful in creep, as it predicts unlimited strain under a finite constant stress (when the step stress is held indefinitely). Further, it is unable to demonstrate the time-dependent reversal of strain (recovery) that many biological tissues experience when the stress is removed.

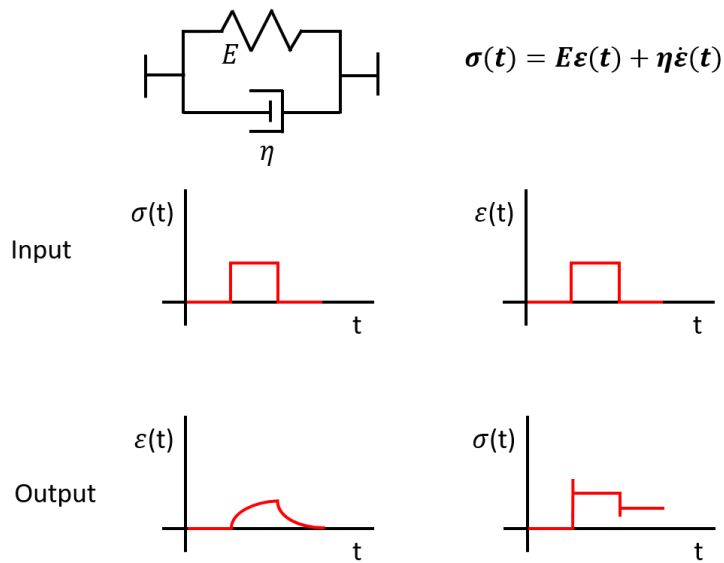


Figure 8: Stress and strain response of a viscoelastic material, represented by a Kelvin-Voigt model.

In the Kelvin-Voigt model (Figure 8), the spring and dashpot are in parallel. This model is useful for modeling the behavior of solid-like VE materials. It is complimentary to the Maxwell model, in that it is suitable for modeling creep, but less so for modeling stress relaxation. In creep, the Kelvin-Voigt model does predict a time-dependent recovery upon the removal of stress, which many VE materials demonstrate. In fact, this model is the simplest phenomenological model capturing creep behavior. On the other hand, in stress relaxation, this model predicts an infinite stress response to a step strain response (due to the presence of the dashpot), which is not physically realizable.

2.3.1.2 Biphasic Modeling of Cartilage

Like many biological materials, cartilage exhibits VE behavior in that it creeps in response to a step stress, and displays stress relaxation in response to a step strain (Mow

and Huiskes, 2005). Linear biphasic constitutive theory is commonly used to model this VE response, following seminal work by Mow and coauthors (Mow et al., 1980). This theory, also referred to as poroelastic theory, attributes the mechanical response of cartilage to interactions between its two-part structure (Figure 9): the ECM composed of collagen and PGs, and the interstitial fluid (Mow et al., 1980). As such, biphasic theory models the cartilage as a mixture consisting of two phases: a porous solid media (the solid phase) with interstitial fluid (the fluid phase) occupying the space within the pores (Mow et al., 1980).

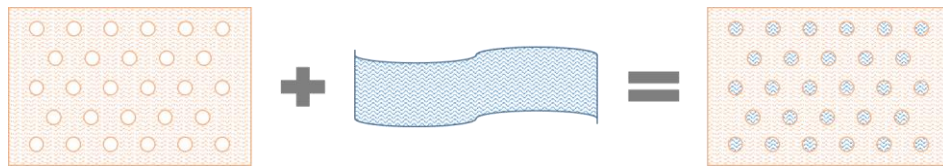


Figure 9: Illustration of the biphasic model of cartilage. The porous ECM (made of collagen and PG) represents the solid phase while the interstitial fluid represents the fluid phase. The fluid resides within the pores of the solid phase.

Therefore, mechanical loading develops a stress on the solid phase as well as pressurizes the fluid phase (Lu and Mow, 2008; Soltz and Ateshian, 1998), causing fluid to flow out of the tissue towards lower pressure following Darcy’s law (Grodzinsky and Frank, 2011). For example, in response to a constant applied stress, there is both a stress on the solid ECM and a pressure on the interstitial fluid, with the fluid pressure supporting a large portion—up to as much as 90%—of the total stress initially (Guo et al., 2003; Soltz and Ateshian, 1998, 2000). Then, as the fluid flows out of the tissue driven by this pressure, the stress on the solid matrix supports more and more of the applied

load. Eventually, upon reaching equilibrium, fluid flow and load sharing stop, and the entirety of the load is supported by the solid phase (Guo et al., 2003; Mow et al., 1980). Because the permeability of cartilage tissue is quite small (Mow et al., 1980), large fluid pressures are required to induce flow out of the tissue (Mow and Huiskes, 2005), and this flow occurs over time (Soltz and Ateshian, 1998). In this manner, the fluid pressure acts to shield the solid ECM from high stresses initially in response to loading (Guo et al., 2003; Soltz and Ateshian, 1998, 2000; Suh et al., 1995). Indeed, the tissue's frictional resistance to fluid flow (causing pressurization of the interstitial fluid) is traditionally viewed as the primary source of the observed VE response and mechanical function of cartilage in compression (Mow and Huiskes, 2005; Sophia Fox et al., 2009).

2.3.1.3 Linear Biphasic Theory Governing Equations

The governing equations describing the cartilage mixture under linear biphasic theory result from several continuity equations (for mass and momentum) and the application of several assumptions (Ateshian, 2017; Mow et al., 1980). The cartilage is modeled as a mixture of two phases: a porous solid phase and a fluid phase (Ateshian, 2017; Mow et al., 1980).

The first continuity equation is the balance of mass:

$$\text{div}(\varphi^s \vec{v}^s + \varphi^f \vec{v}^f) = 0 \quad (\text{Eq. 1})$$

where φ^s = volume fraction of solid phase (solidity)

φ^f = volume fraction of fluid phase (porosity)

\vec{v}^s = velocity vector of solid phase

\vec{v}^f = velocity vector of fluid phase

$$\varphi^s + \varphi^f = 1 \quad (\text{mixture saturation condition}) \quad (\text{Eq. 2})$$

The next two continuity equations are balances of linear momentum for the solid and fluid phases, respectively. In linear biphasic theory, loading is assumed to be quasi-static, and therefore inertia terms are not included in the balances of linear momentum.

Balance of linear momentum (solid phase):

$$\text{div}(\tilde{\sigma}^s) + \tilde{\pi} = 0 \quad (\text{Eq. 3a})$$

where $\tilde{\sigma}^s$ = total stress tensor of solid phase

$\tilde{\pi}$ = momentum exchange tensor between phases

Balance of linear momentum (fluid phase):

$$\text{div}(\tilde{\sigma}^f) - \tilde{\pi} = 0 \quad (\text{Eq. 3b})$$

where $\tilde{\sigma}^f$ = total stress tensor of fluid phase

$\tilde{\pi}$ = momentum exchange tensor between phases

Each phase is assumed to be intrinsically incompressible (Mow et al., 1980). This means that compression of the tissue (the mixture) is only possible if fluid flows out of the tissue. It also means that the total stress of each phase is divided into a hydrostatic pressure term and either a solid elastic stress term or a viscous fluid stress term:

$$\tilde{\sigma}^s = -\phi^s p I + \tilde{\sigma}^e \quad (\text{Eq. 4a})$$

and

$$\tilde{\sigma}^f = -\phi^f p I + \tilde{\sigma}^v \quad (\text{Eq. 4b})$$

where p = magnitude of fluid pressure

I = identity matrix

$\tilde{\sigma}^e$ = elastic stress tensor (of the solid phase)

$\tilde{\sigma}^v$ = viscous stress tensor (of the fluid phase)

$-\phi^s p I$ or $-\phi^f p I$ = hydrostatic pressure term

Furthermore, under linear biphasic theory, the solid phase is assumed to be a linearly elastic, homogeneous, and isotropic material experiencing infinitesimal strain:

$$\tilde{\sigma}^e = \lambda_s \text{tr}(\tilde{\varepsilon}) I + 2\mu_s \tilde{\varepsilon} \quad (\text{Eq. 5})$$

where $\tilde{\varepsilon} = \frac{1}{2}(\text{grad}(\vec{u}) + \text{grad}^T(\vec{u}))$ = infinitesimal strain tensor

\vec{u} = solid matrix displacement vector

λ_s, μ_s = Lamé's constants (of a linearly elastic and isotropic solid)

Therefore, Equation 4a becomes:

$$\tilde{\sigma}^s = -\phi^s p I + \lambda_s \text{tr}(\tilde{\varepsilon}) I + 2\mu_s \tilde{\varepsilon} \quad (\text{Eq. 6})$$

Additionally, the momentum exchange between the fluid and solid phases ($\tilde{\pi}$) is assumed to be much larger than the viscosity of the fluid. This is consequence of the very low permeability of the tissue (Mow and Huijskes, 2005; Mow et al., 1980), indicating a large resistance to fluid flow. In other words, the observed VE behavior of the tissue is assumed to be dominated by the momentum exchange between the phases

(Ateshian, 2017; Mow et al., 1980). Consequently, the viscous stress of the fluid phase is assumed to be negligible:

$$\tilde{\sigma}^v = 0 \quad (\text{Eq. 7})$$

Therefore, Equation 4b becomes:

$$\tilde{\sigma}^f = -\varphi^f p I \quad (\text{Eq. 8})$$

Moreover, the momentum exchange between the fluid and solid phases ($\tilde{\pi}$) is assumed to be linearly proportional to the relative velocity between the phases:

$$\tilde{\pi} = K(\vec{v}^f - \vec{v}^s) \quad (\text{Eq. 9})$$

where K = diffusive drag constant

Substituting Equations 8 and 9 into Equation 3b gives:

$$\text{div}(-\varphi^f p I) - K(\vec{v}^f - \vec{v}^s) = 0 \quad (\text{Eq. 10})$$

$$-\varphi^f \text{div}(p I) - K(\vec{v}^f - \vec{v}^s) = 0 \quad (\text{Eq. 11})$$

$$-\varphi^f \text{grad}(p) - K(\vec{v}^f - \vec{v}^s) = 0 \quad (\text{Eq. 12})$$

Please see Appendix A for a proof of equivalency of Equations 11 and 12.

Similarly, substituting Equations 6 and 9 into Equation 3a gives:

$$\text{div}(-\phi^s p I + \lambda_s \text{tr}(\tilde{\epsilon}) I + 2\mu_s \tilde{\epsilon}) + K(\vec{v}^f - \vec{v}^s) = 0 \quad (\text{Eq. 13})$$

$$\text{div}(-\phi^s p I) + \text{div}(\lambda_s \text{tr}(\tilde{\epsilon}) I + 2\mu_s \tilde{\epsilon}) + K(\vec{v}^f - \vec{v}^s) = 0 \quad (\text{Eq. 14})$$

$$\begin{aligned} -\phi^s \text{grad}(p) + (\lambda_s + \mu_s) \text{grad}(\text{div}(\vec{u})) + \dots \\ \mu_s \nabla^2 \vec{u} + K(\vec{v}^f - \vec{v}^s) = 0 \end{aligned} \quad (\text{Eq. 15})$$

Please see Appendix B for a proof of equivalency of Equations 14 and 15.

Together, Equations 1, 12, and 15 represent the governing equations of linear biphasic theory, describing the balance of mass, balance of linear momentum of the fluid phase, and balance of linear momentum of the solid phase, respectively. Alternately, by defining other terms, the relative fluid velocity and the hydraulic permeability, and by combining the balance of linear momentum equations, these three governing equations (1, 12, and 15) can be re-expressed (Ateashian, 2017).

Relative fluid velocity (\bar{w}):

$$\bar{w} = \varphi^f (\vec{v}^f - \vec{v}^s) \quad (\text{Eq. 16})$$

Hydraulic permeability (k):

$$k = (\varphi^f)^2 / K \quad \text{or} \quad K = (\varphi^f)^2 / k \quad (\text{Eq. 17})$$

Combining the linear momentum balances, Equations 12 and 15, results in:

$$\begin{aligned} & -\varphi^f \text{grad}(p) - K(\vec{v}^f - \vec{v}^s) + \dots \\ & \quad -\varphi^s \text{grad}(p) + \dots \\ & (\lambda_s + \mu_s) \text{grad}(\text{div}(\bar{u})) + \mu_s \nabla^2 \bar{u} + K(\vec{v}^f - \vec{v}^s) = 0 \quad (\text{Eq. 18}) \end{aligned}$$

$$\begin{aligned} & -\varphi^f \text{grad}(p) - \varphi^s \text{grad}(p) + \dots \\ & (\lambda_s + \mu_s) \text{grad}(\text{div}(\bar{u})) + \mu_s \nabla^2 \bar{u} = 0 \quad (\text{Eq. 19}) \end{aligned}$$

$$(-\varphi^f - \varphi^s) \text{grad}(p) + (\lambda_s + \mu_s) \text{grad}(\text{div}(\bar{u})) + \mu_s \nabla^2 \bar{u} = 0 \quad (\text{Eq. 20})$$

Substituting the mixture saturation condition, Equation 2, into Equation 20 gives:

$$-\text{grad}(p) + (\lambda_s + \mu_s) \text{grad}(\text{div}(\bar{u})) + \mu_s \nabla^2 \bar{u} = 0 \quad (\text{Eq. 21})$$

Moving on, substituting Equation 17 into Equation 12 results in:

$$-\varphi^f \text{grad}(p) - \frac{(\varphi^f)^2}{k} (\vec{v}^f - \vec{v}^s) = 0 \quad (\text{Eq. 22})$$

$$-\varphi^f \text{grad}(p) = \frac{(\varphi^f)^2}{k} (\vec{v}^f - \vec{v}^s) \quad (\text{Eq. 23})$$

$$-k \text{grad}(p) = \varphi^f (\vec{v}^f - \vec{v}^s) \quad (\text{Eq. 24})$$

Further substituting Equation 16 into Equation 24 gives:

$$-k \text{grad}(p) = \vec{w} \quad (\text{Eq. 25})$$

Equation 25 is an expression of Darcy's Law, in which the relative fluid velocity (\vec{w}) is proportional to the gradient in pressure, where the constant of proportionality is the hydraulic permeability (k).

Finally, substitution of Equation 2 (the mixture saturation condition) into Equation 1 results in an expression containing the relative fluid velocity (Equation 16):

$$\text{div}(\varphi^s \vec{v}^s + \varphi^f \vec{v}^f) = 0 \quad (\text{Eq. 1})$$

$$\text{div}((1 - \varphi^f) \vec{v}^s + \varphi^f \vec{v}^f) = 0 \quad (\text{Eq. 26})$$

$$\text{div}(\vec{v}^s - \varphi^f \vec{v}^s + \varphi^f \vec{v}^f) = 0 \quad (\text{Eq. 27})$$

$$\text{div}(\vec{v}^s + \varphi^f (\vec{v}^f - \vec{v}^s)) = 0 \quad (\text{Eq. 28})$$

$$\text{div}(\vec{v}^s + \vec{w}) = 0 \quad (\text{Eq. 29})$$

Together, Equations 21, 25, and 29 represent a re-expression of the governing equations of linear biphasic theory:

$$-\text{grad}(p) + (\lambda_s + \mu_s) \text{grad}(\text{div}(\vec{u})) + \mu_s \nabla^2 \vec{u} = 0 \quad (\text{Eq. 21})$$

$$\vec{w} = -k \text{grad}(p) \quad (\text{Eq. 25})$$

$$\text{div}(\vec{v}^s + \vec{w}) = 0 \quad (\text{Eq. 29})$$

2.3.1.4 Application of Linear Biphasic Theory Governing Equations to Confined Compression Creep

A common experimental setup used to measure cartilage mechanical properties is confined compression (Mow et al., 1980). In this setup, a cylindrical cartilage plug of original thickness h is harvested from the tissue and placed within an impermeable cylindrical chamber, where it is confined both on the top and bottom as well as radially. One of the chamber surfaces (either top or bottom) is porous to permit fluid flow, and the cartilage plug is compressed within the chamber (Figure 10), shown as presented in the literature (Ateshian, 2017; Mow et al., 1980). This setup is convenient as lateral expansion of the cartilage plug during compression is prevented, restricting the resulting displacement and fluid flow to be one-dimensional (along the cylindrical or z axis).

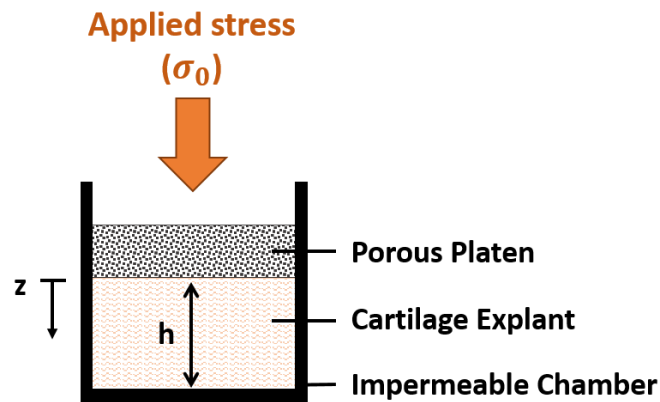


Figure 10: Cartilage confined compression test setup (Mow et al., 1980). The original thickness of the explant is given by h , and the axial coordinate describing the one-dimensional deformation is given by z ($z = 0$ is at the interface between the porous platen and the explant, while $z = h$ is at the interface between the explant and the bottom of the impermeable chamber).

Application of the governing equations (Equations 21, 25, and 29, respectively) to this configuration leads to a partial differential equation (PDE) describing this setup (Ateshian, 2017; Mow et al., 1980), which can be solved analytically.

Reduction of Equation 21 (balance of linear momentum) to one dimension (1D), and definition of the aggregate modulus, yields:

Aggregate modulus (H_A):

$$H_A = \lambda_s + 2\mu_s \quad (\text{Eq. 30})$$

Equation 21 in 1D:

$$-\frac{\partial p}{\partial z} + (\lambda_s + \mu_s) \frac{\partial^2 u_z}{\partial z^2} + \mu_s \frac{\partial^2 u_z}{\partial z^2} = 0 \quad (\text{Eq. 31})$$

Please see Appendix C for 1D simplification of Equation 21 to Equation 31.

$$-\frac{\partial p}{\partial z} + (\lambda_s + 2\mu_s) \frac{\partial^2 u_z}{\partial z^2} = 0 \quad (\text{Eq. 32})$$

$$-\frac{\partial p}{\partial z} + H_A \frac{\partial^2 u_z}{\partial z^2} = 0 \quad (\text{Eq. 33})$$

Next, expressing Equation 25 (Darcy's law) in 1D gives:

$$w_z = -k \frac{\partial p}{\partial z} \quad (\text{Eq. 34})$$

Likewise, expressing Equation 29 (balance of mass) in 1D results in:

$$\frac{\partial}{\partial z} \left(\frac{\partial u_z}{\partial t} + w_z \right) = 0 \quad (\text{Eq. 35})$$

Please see Appendix D for 1D simplification of Equation 29 to Equation 35.

Integrating Equation 35 with respect to z gives:

$$\int \left(\frac{\partial}{\partial z} \left(\frac{\partial u_z}{\partial t} + w_z \right) \right) \partial z = \int 0 \partial z \quad (\text{Eq. 36})$$

$$\frac{\partial u_z}{\partial t} + w_z = R(t) \quad (\text{Eq. 37})$$

Here, $R(t)$ is an integration function that is constant across z and can be determined from the boundary conditions. The boundary conditions arise from the fact that there is no displacement of the solid matrix at the bottom of the chamber ($z = h$, Figure 10), and that there is no fluid movement at the bottom of the chamber, either:

$$\frac{\partial u_{z=h}}{\partial t} = 0 \quad (\text{Eq. 38})$$

$$w_{z=h} = 0 \quad (\text{Eq. 39})$$

Plugging Equations 38 and 39 into Equation 37 gives:

$$0 + 0 = R(t) \quad (\text{Eq. 40})$$

Therefore, with $R(t) = 0$ (Equation 40), Equation 37 can be simplified as:

$$w_z = -\frac{\partial u_z}{\partial t} \quad (\text{Eq. 41})$$

Equations 34 and 41 are both expressions for the relative fluid velocity, w_z .

Merging these two expressions gives:

$$-\frac{\partial u_z}{\partial t} = -k \frac{\partial p}{\partial z} \quad (\text{Eq. 42})$$

$$\frac{1}{k} \frac{\partial u_z}{\partial t} = \frac{\partial p}{\partial z} \quad (\text{Eq. 43})$$

Equation 43 represents an expression for the change in pressure across the depth of the tissue as a function of the solid matrix displacement (u_z), which can be substituted into Equation 33 (the 1D balance of linear momentum):

$$-\left(\frac{1}{k} \frac{\partial u_z}{\partial t}\right) + H_A \frac{\partial^2 u_z}{\partial z^2} = 0 \quad (\text{Eq. 44})$$

$$\frac{\partial^2 u_z}{\partial z^2} - \frac{1}{H_A k} \frac{\partial u_z}{\partial t} = 0 \quad (\text{Eq. 45})$$

Equation 45 represents the PDE describing the confined compression setup (Ateshian, 2017; Mow et al., 1980). This PDE is a version of the heat equation, relating first derivatives (of a variable) with respect to time to second derivatives (of the same variable) with respect to space. As the sample is at rest initially, this PDE is subject to the following initial condition:

$$u_z(z, t = 0) = 0 \quad (\text{Eq. 46})$$

Likewise, there is no tissue displacement at the bottom of the chamber ($z = h$).

This yields the following boundary condition:

$$u_z(z = h, t) = 0 \quad (\text{Eq. 47})$$

The next boundary condition changes depending upon what type of experiment is performed (creep, stress relaxation, etc). For creep, where a compressive load is applied and held constant, the boundary condition at the top of the chamber ($z = 0$) is that the total axial normal stress equals the constant applied stress (σ_0):

$$\sigma_{zz}(z = 0, t) = -\sigma_0 \quad (\text{Eq. 48})$$

From Equation 6 (in 1D) and Equation 30, the total axial normal stress is given by:

$$\sigma_{zz} = -\varphi^s p_z + H_A \frac{\partial u_z}{\partial z} \quad (\text{Eq. 49})$$

At the top of the chamber ($z = 0$), there is no hydrostatic pressure ($p_z = 0$), since the porous platen provides a free-draining interface. Thus, for $z = 0$, Equation 49 reduces to:

$$-\sigma_0 = H_A \frac{\partial u_{z=0}}{\partial z} \quad (\text{Eq. 50})$$

In summary, the confined compression creep problem is given by Equation 45, subject to Equations 46, 47, and 50 (Ateshian, 2017; Mow et al., 1980):

$$\frac{\partial^2 u_z}{\partial z^2} - \frac{1}{H_A k} \frac{\partial u_z}{\partial t} = 0 \quad (\text{Eq. 45})$$

$$u_z(z, t = 0) = 0 \quad (\text{initial condition}) \quad (\text{Eq. 46})$$

$$u_z(z = h, t) = 0 \quad (\text{boundary condition}) \quad (\text{Eq. 47})$$

$$-\sigma_0 = H_A \frac{\partial u_{z=0}}{\partial z} \quad (\text{boundary condition}) \quad (\text{Eq. 50})$$

The solution to the above confined compression creep problem at the surface where the load is applied ($z = 0$) is given by Equations 51-53 (Ateshian, 2017; Mow et al., 1980):

$$\frac{u_z(t)}{h} = \frac{\sigma_0}{H_A} \left[1 - 2 \sum_{n=0}^{\infty} \frac{1}{M} e^{-\left(\frac{M}{\tau}\right)t} \right] \quad (\text{Eq. 51})$$

$$\text{where } M = \pi^2 \left(n + \frac{1}{2} \right)^2 \quad (\text{Eq. 52})$$

$$\tau = \frac{h^2}{H_A k} \quad (\text{Eq. 53a})$$

Please see Appendix E for the full solution of Equation 45, subject to Equations 46, 47, and 50.

Furthermore, studies often report the characteristic time (Armstrong and Mow, 1982), denoted here as τ_0 . The characteristic time represents the exponential time constant for the first term in the summation of Equation 51, when $n = 0$:

$$M = \pi^2 \left(n + \frac{1}{2} \right)^2 = \pi^2 \left(\frac{1}{2} \right)^2 = \frac{\pi^2}{4}$$

$$\text{and } e^{-\left(\frac{M}{\tau}\right)t} = e^{-\left(\frac{\pi^2}{4\tau}\right)t}$$

where the exponential time constant of this term, τ_0 , equals $\frac{4\tau}{\pi^2}$.

Therefore:

$$\tau_0 = \frac{4}{\pi^2} \tau = \frac{4}{\pi^2} \frac{h^2}{H_A k} \quad (\text{Eq. 53b})$$

2.3.2 Experimental Methodologies

Traditional techniques for measuring cartilage mechanical properties involve ex vivo testing of cartilage tissue, either from animal or cadaveric models (Guo et al., 2003; Mow and Guo, 2002; Mow and Huiskes, 2005). For compressive properties, mechanical testing is performed either through indentation or via confined or unconfined compression (Mansour, 2003) (Figure 11).

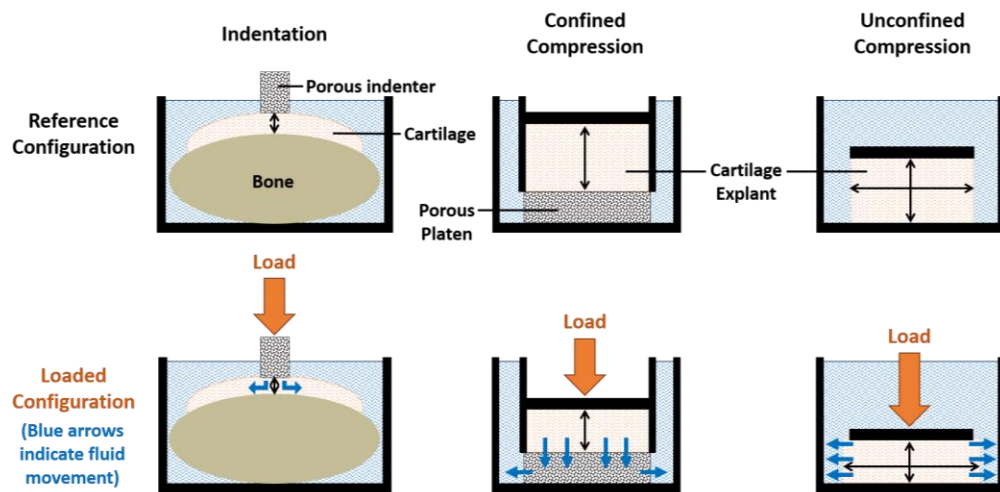


Figure 11: Comparison of cartilage compression testing methodologies.

In indentation (Athanasίου et al., 1991; Froimson et al., 1997), a portion of the cartilage surface is exposed and a porous indenter is pushed into the tissue to compress the region in contact with the indenter. In confined compression (Armstrong and Mow, 1982; Best et al., 1994; Boschetti et al., 2004; Jurvelin et al., 2003), a small cylindrical explant is harvested from the tissue and placed within a chamber, where it is confined radially and on the top and bottom. Either the top or the bottom surface is porous to permit fluid flow, and the sample is compressed within the chamber. In unconfined compression (Armstrong et al., 1984; Jurvelin et al., 2003; Park et al., 2003), the setup is similar to that of confined compression with two notable differences. First, the radial confinement is removed so the explant is free to expand laterally during compression. Second, neither the top nor bottom surfaces need to be porous (and are typically nonporous), as the lack of radial confinement allows fluid to flow radially. In all three of these tests, either an unconfined lateral surface or a porous vertical surface is necessary

to permit fluid movement from within the tissue during deformation. This is crucial as a large contribution to the observed tissue behavior and mechanical function during compression arises from the interaction between the solid phase, the ECM, and the fluid phase, the interstitial fluid within the cartilage (Mow et al., 1980; Nia et al., 2011; Soltz and Ateshian, 1998, 2000). For each of these tests, the theoretical solution (specific to the experimental configuration) (Armstrong et al., 1984; Mak et al., 1987; Mow et al., 1980) is curve-fit to experimental deformation data to quantify the mechanical properties of the tissue. For an example using the confined compression experiment, see Section 2.3.1.4 Application of Linear Biphase Theory Governing Equations to Confined Compression Creep.

Each of these *ex vivo* techniques has been widely used in the literature to quantify cartilage mechanical properties (Table 1), with confined compression and indentation being the most widely used methods (Akizuki et al., 1986a; Armstrong and Mow, 1982; Ateshian et al., 1997; Athanasiou et al., 1991; Chen et al., 2001; Froimson et al., 1997; Jurvelin et al., 2003; Mow and Huiskes, 2005; Setton et al., 1994; Treppo et al., 2000). Indentation is popular because all three mechanical properties (aggregate modulus, permeability, Poisson's ratio) can be quantified (Mow et al., 1989). Confined compression is also popular, though only two mechanical properties (aggregate modulus and permeability) can be measured using this technique (Mow et al., 1980). Unconfined compression results in measurement of the Young's modulus, and when

used in conjunction with confined compression or with optical measurements of the sample's lateral expansion can also quantify the Poisson's ratio (Armstrong et al., 1984; Korhonen et al., 2002). Although direct comparison of testing methodologies used in the literature is difficult—due to differences in the species or cartilage location studied—there is general agreement in property values between testing methodologies (Guo et al., 2003). However, one study directly comparing these techniques (Korhonen et al., 2002) found that indentation testing generally resulted in higher stiffness values than either confined or unconfined compression. This was attributed to differences in boundary conditions: there is disruption of the collagen matrix at the edges of the cartilage explant where it has been excised from the tissue in confined and unconfined compression compared to the native ECM architecture that is exposed to indentation (Korhonen et al., 2002). As collagen is stiff in tension (Akizuki et al., 1986b), especially near the superficial surface where the collagen fibers are oriented tangentially, the uncompromised ECM may resist compressive indentation more than an explant's disrupted ECM can resist compression (Korhonen et al., 2002).

Table 1: Reported Mechanical Properties of Healthy (non-OA) Cartilage.
Values represent mean \pm one standard deviation (SD).

Study	Method	Species	Cartilage Location	⁺ H _A (MPa)	⁺⁺ k (m ⁴ /Ns) x 10 ⁻¹⁵
Akizuki et al. 1986	Indentation	Human	Tibial Plateau	0.65 \pm 0.25	2.00 (SD unreported)
Treppo et al. 2000	Confined Compression	Human	Tibial Plateau	0.45 \pm 0.28	9.18 \pm 8.77
Setton et al. 1994	Indentation	Canine	Meniscus-covered Tibial Plateau	0.56 \pm 0.19	2.4 \pm 1.3
			Meniscus-uncovered Tibial Plateau	0.49 \pm 0.19	5.0 \pm 1.7
Cutcliffe and DeFrate (In Review) (Section 4)	Confined Compression	Porcine	Tibial Plateau	0.40 \pm 0.18	0.71 \pm 0.27
			Femoral Trochlea	1.17 \pm 0.48	0.59 \pm 0.27
Armstrong and Mow 1982	Confined Compression	Human	Patella	0.79 \pm 0.36	4.70 \pm 3.6
Froimson et al. 1997	Indentation	Human	Patella	0.42 \pm 0.15	2.46 \pm 1.00
			Femoral Trochlea	0.60 \pm 0.15	1.48 \pm 1.00
Jurvelin et al. 2003	Confined Compression	Human	Femoral Trochlea	0.85 \pm 0.38	1.75 \pm 1.82
Athanasίου et al. 1991	Indentation	Human	Femoral Trochlea	0.53 \pm 0.09	2.17 \pm 0.73
			Lateral Condyle	0.70 \pm 0.23	1.18 \pm 0.21
			Medial Condyle	0.59 \pm 0.11	1.14 \pm 0.16
		Canine	Femoral Trochlea	0.56 \pm 0.14	0.93 \pm 0.84
			Lateral Condyle	0.60 \pm 0.24	0.77 \pm 0.56
			Medial Condyle	0.90 \pm 0.22	0.80 \pm 0.78
		Bovine	Femoral Trochlea	0.47 \pm 0.15	1.42 \pm 0.58
			Lateral Condyle	0.89 \pm 0.29	0.43 \pm 0.20
			Medial Condyle	0.90 \pm 0.43	0.46 \pm 0.33
Chen et al. 2001	Confined Compression	Bovine	Femoral Trochlea	0.47 \pm 0.11	7.30 \pm 1.73
Ateshian et al. 1997	Confined Compression	Bovine	Glenoid	0.40 \pm 0.14	2.70 \pm 1.50
Mow et al. 1980	Confined Compression	Bovine	(unreported)	0.70 \pm 0.09	7.60 \pm 4.20

⁺H_A = aggregate modulus, ⁺⁺k = permeability.

While these ex vivo approaches are paramount to quantifying material properties and understanding how they may change with composition or pathology, their application typically requires cadaveric (either human or animal) samples, leaving in vivo determination of cartilage material properties yet to be performed. Thus, traditional ex vivo techniques have limited applicability in measuring in vivo material properties of human subjects at risk of developing or currently suffering from OA.

2.3.3 Mechanical Changes Seen in Osteoarthritis

In addition to compositional changes seen within cartilage during OA progression, changes in the mechanical response of the tissue take place as well (Guilak, 2011; Knecht et al., 2006). For instance, PG loss occurs during the progression of OA (Thompson and Oegema, 1979). Studies investigating compositional and mechanical variations in normal cartilage, as well as studies investigating OA cartilage, have observed decreases in stiffness as PG content decreases (Akizuki et al., 1986b; Froimson et al., 1997; Hatcher et al., 2017; Rivers et al., 2000; Roberts et al., 1986; Treppo et al., 2000). This relationship has also been observed when PG is enzymatically depleted from explants (Collins et al., 2018a; Grenier et al., 2014) or when cartilage degradation is induced via inflammatory cytokines or other proteinases (Bonassar et al., 1995; Bonassar et al., 1996; Legare et al., 2002). Further, alterations in collagen organization are also observed during OA (Hollander et al., 1995). As before, increases in collagen network disruption and simultaneous decreases in stiffness have been observed in OA cartilage

(Hatcher et al., 2017), in explants where collagen is enzymatically degraded (Collins et al., 2018a; Grenier et al., 2014), and when degradation is initiated by stimulating cartilage catabolism or the inflammatory cascade (Bonassar et al., 1995; Bonassar et al., 1996; Legare et al., 2002). Moreover, an important factor in the regulation of chondrocyte metabolism and homeostasis is the mechanical loading environment of the tissue (Guilak, 2011). As such, changes in the tissue's mechanical response may not only reflect initiation of cartilage degeneration, but may also contribute to further pathological metabolic and compositional changes in the tissue (Guilak, 2011). Indeed, in animal models of OA induced via transection of the anterior cruciate ligament (ACL, one of the four main stabilizing ligaments in the knee), decreases in cartilage stiffness (Setton et al., 1994) and decreases in PG content (Sah et al., 1997) compared to controls have been observed. These changes are likely due to the altered loading environment experienced by the ACL deficient knee. Therefore, in addition to changes in composition, alterations in cartilage mechanical properties and response to loading may act as early signs of OA progression.

2.4 Magnetic Resonance Imaging of Cartilage

2.4.1 Introduction to Magnetic Resonance Imaging

Magnetic resonance imaging (MRI) has been extensively used to image soft tissue (Nishimura, 2010) (Figure 12). MRI relies on the principle of nuclear magnetic resonance, in which certain atomic nuclei align when placed under an external magnetic

field (Nishimura, 2010). The main atom of interest in MRI is hydrogen, since the human body is largely composed of water molecules and contains many hydrogen atoms (Nishimura, 2010). To create an MRI, first the hydrogen protons are aligned by applying a large, main external magnetic field to define a principal axis (commonly denoted as B_0). Then, a small radiofrequency (RF) pulse is briefly applied perpendicular to B_0 . This perturbation initially tips the hydrogen protons out of alignment with B_0 , but over time they relax back into alignment with the main magnetic field (B_0), emitting RF energy as they do so (Nishimura, 2010).

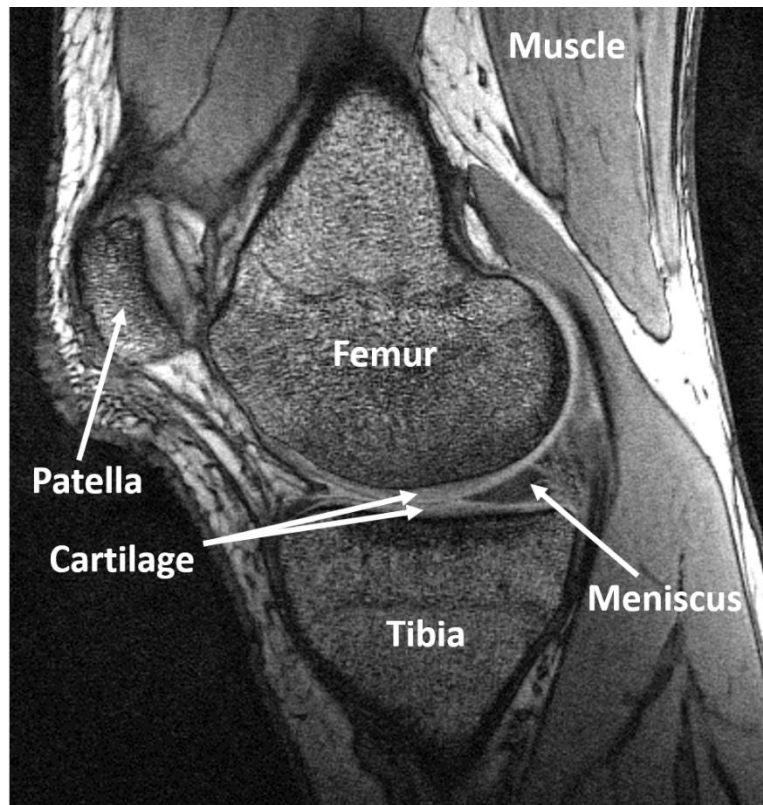


Figure 12: Example of an MRI of the knee, illustrating visualization of various tissues within and around the joint.

Different tissues have distinct relaxation parameters, which creates contrast between separate tissue structures via MRI (Nishimura, 2010) (Figure 12). Two main types of relaxation occur, termed T1 and T2 relaxation (Figure 13), which describe the relaxation of the net magnetization of the hydrogen protons broken down into its components both parallel and perpendicular to the external field, B_0 (Nishimura, 2010). T1 relaxation describes the increase over time of the component of magnetization parallel to B_0 , as the tipped hydrogen protons realign with B_0 . This relaxation occurs via exponential approach, as detailed in Equation 54 (Nishimura, 2010). On the other hand, T2 relaxation describes the decrease over time of the magnetization component perpendicular to B_0 , as the tipped hydrogen protons lose phase coherence with each other. This relaxation occurs via exponential decay, as shown in Equation 55 (Nishimura, 2010). The combination of the T1 and T2 relaxation processes results in a net magnetization with a hemispherical path (Nishimura, 2010).

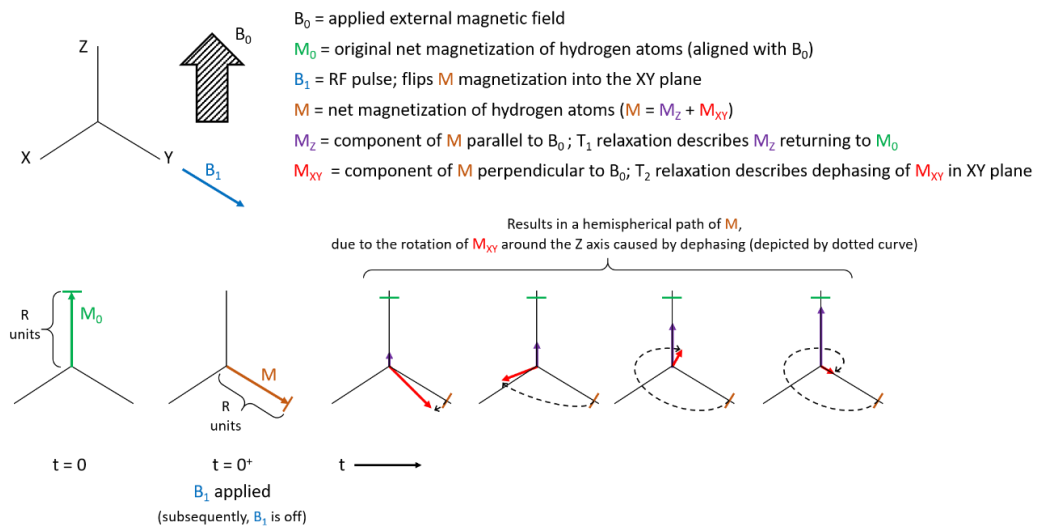


Figure 13: Diagram of hydrogen proton magnetization vector components during MRI acquisition. R units represents an arbitrary quantity denoting the length of M_0 (and of M at $t = 0^+$) for visualization purposes, to show that over time the length of the M_z component approaches R while the length of the M_{XY} component decreases from R.

$$M_z = M_0 \left(1 - e^{-\left(\frac{t}{T_1}\right)} \right) \quad (\text{Eq. 54})$$

$$M_{XY} = M_0 e^{-\left(\frac{t}{T_2}\right)} \quad (\text{Eq. 55})$$

where M_z = component of M_0 parallel to external magnetic field

M_{XY} = component of M_0 perpendicular to external magnetic field

M_0 = original net magnetization of hydrogen atoms

T_1 = time constant governing T1 regrowth

T_2 = time constant governing T2 decay

2.4.2 MRI for Cartilage Geometry Measurements

MRI can be used to create subject-specific 3D models of joint morphology, including bone and cartilage, enabling assessment of changes in cartilage thickness or

volume before and after activity (Eckstein et al., 1998). Measuring cartilage deformation in this manner allows for the noninvasive assessment of mechanical response to functional loading by capturing the strain (either engineering strain or volumetric strain) resulting from activity. Typical activities studied with this methodology include diurnal changes (Coleman et al., 2013; Waterton et al., 2000; Widmyer et al., 2013), knee bends (Eckstein et al., 2005; Eckstein et al., 2000; Eckstein et al., 1999; Eckstein et al., 1998; Hudelmaier et al., 2001; Van Ginckel et al., 2011), hopping (Cher et al., 2016; Owusu-Akyaw et al., 2018; Sutter et al., 2019; Sutter et al., 2015), running (Boocock et al., 2009; Eckstein et al., 2005; Kersting et al., 2005; Kessler et al., 2006, 2008; Mosher et al., 2010; Niehoff et al., 2011; Van Ginckel et al., 2013), and walking (Collins et al., 2018b; Eckstein et al., 2005; Lad et al., 2016; Liu et al., 2017; Paranjape et al., 2019). Walking is especially of interest as it represents an important activity of daily living, the most common form of exercise in the US (Bureau of Labor Statistics, 2016), and a clinical recommendation to OA patients (Focht, 2006). Moreover, a recent study investigating cartilage strain as a function of walk duration found that strain increased monotonically with increasing walk duration, but reached an asymptote between 40 and 60 minutes of walking (Paranjape et al., 2019) (Section 3. A New Stress Test for Knee Joint Cartilage). This asymptotic strain response was well-fit with the Kelvin-Voigt exponential model for creep, indicating that in vivo cartilage behavior resembles ex vivo cartilage behavior. Importantly, the dose-response methodology used in this study (Paranjape et al., 2019)

allows for the measurement of the characteristic creep time governing the asymptotic response of the cartilage, which is a structural property related to the cartilage aggregate modulus and permeability under biphasic theory (Mow and Huijkes, 2005; Mow et al., 1980). Though it has yet to be quantified, the recovery response can be determined in a similar fashion by measuring the recovery of cartilage thickness after activity.

Measuring cartilage deformation and recovery in this manner allows for the quantification of the characteristic recovery time, also related to the cartilage mechanical properties. Additionally, the recovery response is more accessible to measure via MRI than the creep response. Therefore, measuring changes in cartilage thickness over time in response to activity or after activity represents a cartilage stress test from which structural properties can be quantified in vivo. As such, the mechanical response of cartilage to functional loading may be noninvasively assessed in vivo with MR imaging, and investigation of this response in healthy vs OA groups may demonstrate its utility as a metric of cartilage health.

2.4.3 Quantitative MRI (T1rho and T2)

Quantitative MRI techniques, such as T1rho and T2 mapping, are emerging as noninvasive methods that reflect cartilage composition (Collins et al., 2018a; Li et al., 2007; Li et al., 2009). T1rho relaxation time is a physical property of the cartilage matrix, and is sensitive to interactions between water molecules and PG in the ECM (Guermazi et al., 2015; Li et al., 2007). Specifically, T1rho relaxation quantifies the energy dissipation

of excited hydrogen protons in the rotating frame when locked in phase by a spin lock pulse as the transverse magnetization vector decays to zero during the MRI acquisition (Matzat et al., 2013). Due to electrostatic interactions, hydrogen protons in water molecules located near large macromolecules such as PGs dissipate energy more quickly than protons in free water, resulting in faster T1rho relaxation (decreased relaxation times) (Matzat et al., 2013). Therefore, it is expected that T1rho relaxation time is sensitive to changes in PG content. Indeed, increased T1rho relaxation times correlate with PG loss in cartilage when PGs or GAGs are enzymatically depleted from the tissue (Akella et al., 2001; Collins et al., 2018a; Duvvuri et al., 2002; Duvvuri et al., 1997; Regatte et al., 2003). This relationship is also observed in studies examining both healthy and degenerated cadaveric or ex vivo cartilage, as increases in T1rho relaxation time correlate with decreases in GAG content seen in OA (Hatcher et al., 2017; Keenan et al., 2011; Li et al., 2011a; Nishioka et al., 2012). T1rho relaxation time may even be related to mechanical function, as increases in T1rho relaxation time concomitant with decreases in aggregate modulus are observed in cartilage explants both with the PG loss that occurs during OA (Hatcher et al., 2017) and when PG content is reduced via enzymatic depletion (Collins et al., 2018a).

Similarly, T2 relaxation time is related to collagen organization and water content within the cartilage (Guermazi et al., 2015; Li et al., 2007; Matzat et al., 2013; Menezes et al., 2004; Nishioka et al., 2012). T2 relaxation quantifies the loss of phase

coherence in the transverse plane between excited hydrogen protons as the transverse magnetization vector decays to zero (Matzat et al., 2013), and this decay is prolonged by the presence of free water. As such, it is expected that slower T2 relaxation (increased relaxation time) occurs when more free water is present within cartilage tissue (Guermazi et al., 2015). This sensitivity to free water content is thought to indicate the breakdown of the ECM and loss of collagen architecture (Guermazi et al., 2015; Matzat et al., 2013). Experimental results support this idea, as T2 relaxation time increases with enzymatic treatment of collagenase in cartilage explants, causing decreases in collagen organization (Collins et al., 2018a). Increases in T2 relaxation time were also observed after enzymatic treatment reducing PG content (Wayne et al., 2003), indicating that T2 relaxation time may also be sensitive to changes in water content incurred by changes in PG content. As with T1rho, T2 relaxation time may also be indicative of mechanical function, as increases in T2 relaxation time are observed alongside decreases in aggregate modulus in cartilage explants treated with collagenase (Collins et al., 2018a). In light of these findings, quantitative MRI methods (T1rho and T2 mapping) may represent promising diagnostic tools used for the noninvasive assessment of cartilage composition.

2.4.4 Imaging Changes Seen in Osteoarthritis

Notably, studies using MRI to investigate activity-induced cartilage strain have shown differences in deformation in groups that are at an increased risk of OA, such as

individuals with joint injury (Owusu-Akyaw et al., 2018; Sutter et al., 2019), obesity (Collins et al., 2018b; Widmyer et al., 2013), or advanced age (Hudelmaier et al., 2001). For example, strain in patellar cartilage and in certain areas of femoral cartilage after acute loading (single-legged hopping) is different in knees with ACL injury compared to their intact contralateral counterparts (Owusu-Akyaw et al., 2018; Sutter et al., 2019). Likewise, volumetric deformation of femoral and tibial cartilage after 30 minutes of running is larger in ACL reconstructed knees compared to matched controls (Van Ginckel et al., 2013). Similar to ACL injury or reconstruction, obese subjects exhibit larger tibial cartilage strain after 20 minutes of walking than subjects with a normal BMI (Collins et al., 2018b), as well as during typical diurnal loading (Widmyer et al., 2013). Finally, differences in cartilage deformation with age have also been observed; for instance, subjects free of knee pain aged 50-78 years demonstrate decreased patellar cartilage volumetric deformation after knee bends than subjects aged 20-30 years (Hudelmaier et al., 2001). These results motivate that measuring the mechanical response to functional loading (e.g. exercise activities) may provide further insight into cartilage health, and may be able to differentiate healthy from at-risk cartilage before the onset of degenerative symptoms.

Likewise, *in vivo* studies have shown that both T1rho and T2 relaxation times are significantly elevated in patients with radiographic OA compared to healthy controls (Dunn et al., 2004; Li et al., 2007; Li et al., 2009; Stahl et al., 2009). For T1rho, increases in

relaxation time correlate with increased OA severity as assessed via MR and radiographic grading (Li et al., 2007; Souza et al., 2013). Moreover, differences in T1rho and T2 relaxation times have been observed in groups at an increased risk of OA, such as those with focal cartilage abnormalities (Stahl et al., 2009), those with ACL injuries and cartilage lesions (Gupta et al., 2014; Nishioka et al., 2013), and those with ACL injuries who have undergone reconstructive surgery (Li et al., 2011b). Therefore, T1rho and T2 relaxation times may also represent important noninvasive measures that are sensitive to cartilage composition, and may denote changes in cartilage health before degeneration is detectable by radiography.

3. A New Stress Test for Knee Joint Cartilage

This chapter represents material originally published in Scientific Reports, Volume 9, article number 2283 (Paranjape et al., 2019). It is available at <https://doi.org/10.1038/s41598-018-38104-2>. This reuse is permitted under the copyright terms, as the article is open access (published under the Creative Commons Attribution 4.0 International License). A link to a summary of the license terms is available at <https://creativecommons.org/licenses/by/4.0/>, and a link to the license itself is available at <https://creativecommons.org/licenses/by/4.0/legalcode>. No substantial changes other than formatting were made. Collaborators on this work (C. S. Paranjape, S. C. Grambow, G. M. Utturkar, A. T. Collins, W. E. Garrett, C. E. Spritzer, and L. E. DeFrate) are gratefully acknowledged, especially the contributions of Chinmay S. Paranjape (co-first author on this work with Hattie C. Cutcliffe).

This chapter supports Aim 1 (creation of a statistical model relating stiffness to properties measurable via MRI, one of which is the characteristic time) as it establishes that the characteristic creep time can be measured in vivo using MRI.

3.1 Introduction

Cartilage metabolism is related to the mechanical loading of the tissue because chondrocytes, the cells responsible for maintaining cartilage architecture, are mechanically sensitive (Buschmann et al., 1995; Ewers et al., 2001; Guilak, 2011; Loeser et al., 2012; Milentijevic and Torzilli, 2005; Quinn et al., 2001; Sah et al., 1989). Cyclic or

dynamic loading of cartilage in vitro stimulates chondrocyte anabolism, with increased biosynthesis seen in explants (Sah et al., 1989), chondrocytes seeded within agarose (Buschmann et al., 1995; Lee and Bader, 1997; Shelton et al., 2003), and in tissue-engineered cartilage constructs (Mauck et al., 2000). Conversely, static loading in vitro results in decreased biosynthesis in similar models (Buschmann et al., 1995; Larsson et al., 1991). Further, animal studies of joint immobilization show decreases in cartilage stiffness (Jurvelin et al., 1986), a mechanical property of the tissue, with remobilization helping to restore stiffness (Jurvelin et al., 1989). These observations suggest that mechanical loading is necessary for the maintenance of cartilage structure and health (Sun, 2010).

Therefore, exercise is often recommended as a potential treatment for osteoarthritis (OA), a disabling disease of synovial joints that results in cartilage degeneration (Loeser et al., 2012). In controlled trials of exercise intervention for OA, physical activity has resulted in decreased pain scores (Ettinger et al., 1997; Van Baar et al., 1998), decreased disability scores (Ettinger et al., 1997; Van Baar et al., 1998), and increased glycosaminoglycan content as measured by delayed gadolinium-enhanced magnetic resonance imaging (Roos and Dahlberg, 2005). However, it is still unclear how exercise modifies cartilage biomechanics and ultimately joint health. As such, mapping the appropriate exercise duration and intensity to specific therapeutic targets cannot currently be performed because knowledge of how different types and intensities of

exercise influence the mechanical environment of the joint is limited. Detailed dose-response studies quantifying changes in cartilage mechanical response with changes in the duration and intensity of exercise are needed to fill this gap.

Cartilage mechanical response can be quantified by measuring either stress or strain within the tissue (Coleman et al., 2013; Lad et al., 2016; Sutter et al., 2015), which are related to one another by the tissue's mechanical properties (e.g. stiffness). Under a constant stress, cartilage displays creep behavior (Armstrong and Mow, 1982; Mow et al., 1989; Mow et al., 1980), in which the strain increases over time. Leveraging this time-dependent (viscoelastic) response of cartilage to mechanical load (Eckstein et al., 1998), our laboratory has recently developed a new technique for investigating cartilage strain in vivo (Lad et al., 2016) using three dimensional (3D) modeling and magnetic resonance imaging (MRI). This approach provides a means to evaluate cartilage function by applying an exercise stimulus—an in vivo stress—and measuring the resulting strain response, analogous to a cardiac stress test. Therefore, our cartilage stress test may be used to quantify tissue health: as cartilage strain response depends on its mechanical properties and composition, both of which are altered in OA (Lorenz and Richter, 2006), the local strain response may be different in OA patients versus healthy individuals. Furthermore, by measuring strain via MRI, our cartilage stress test can be applied noninvasively to a variety of populations. As walking is the most common form of exercise in the US (Bureau of Labor Statistics, 2016), we explored the dose-dependent

effects of walk duration and walk speed on cartilage thickness and strain, a necessary step to inform exercise-based OA therapies.

Specifically, we quantified the effects of varying durations and speeds on the in vivo response of cartilage following walking exercise to develop a cartilage stress test in a dose-dependent manner. This investigation provides important insight into normal in vivo cartilage biomechanics under varying intensities of loading, which has important implications for OA progression, prevention, and treatment. Additionally, this work provides innovative measurements of normative cartilage creep during walking, revealing this fundamental mechanical behavior in healthy subjects. Overall, this study addresses core questions about cartilage mechanics and informs exercise-based treatment approaches to slowing the progression of OA.

3.2 Methods

3.2.1 Data Collection

Duke University Health System Institutional Review Board (IRB) approval was obtained prior to starting this study. All study procedures were carried out in compliance with the IRB's regulations. Ten healthy subjects, including five males and five females (mean age: 25 years, range: 22–27 years; mean BMI: 22.1 kg/m², range: 20.0–24.7 kg/m²) with no history of injury or surgery to any of the joints in their lower extremities, provided informed written consent prior to their participation. The same subjects participated in two different walk protocols, each consisting of several separate

sessions, where each session took place on a separate day: 1) walking at a fixed, comfortable speed with bouts of different durations (ranging from 10 to 60 minutes) and 2) walking for a fixed duration of 30 minutes at different speeds (including a low, moderate, and high walk speed). Subjects began in the first walk protocol of the study and were given the option to also participate in the second protocol at a later date. The exercise duration or speed was randomized in each protocol.

For each session of both protocols, subjects arrived at 7am, in order to minimize the known diurnal pattern of cartilage strain in the knee and to minimize loading of the joint prior to the study (Coleman et al., 2013). They were instructed not to perform any strenuous exercises the night before or morning of the study. After arrival, subjects rested supine for 45 minutes prior to a baseline MRI scan (Sutter et al., 2015). They were transported to the MR scanner (located adjacent to the room where they rested) using a wheelchair to avoid any weight-bearing following the resting period. Imaging was performed using a 3 Tesla scanner (Trio Tim, Siemens Medical Solutions USA, Malvern, PA) with an 8-channel receive-only knee coil. During imaging, subjects lay supine with their knee in a relaxed, extended position. Sagittal plane images (field of view: 16x16 cm; resolution: 512x512 pixels; slice thickness: 1 mm) were generated using a double-echo steady-state sequence (DESS; flip angle: 25°; repetition time: 17 ms; echo time: 6 ms) (Utturkar et al., 2013). Total pre-activity scan time per session was approximately 9

minutes. Subjects underwent the 45 minutes of rest and pre-activity baseline scan in each study session.

Subjects were then transported via wheelchair to an adjacent treadmill. Under the first protocol, in each session subjects walked for one of five durations (10, 20, 30, 40, or 60 minutes; one duration per session). Subjects also wore a Fitbit (Fitbit Inc., San Francisco, CA) during the walk to quantify step count. Immediately following the walk, subjects underwent a post-activity scan (same as the pre-activity scan; see details above). Time from walk completion to post-activity MRI initiation was $3:24 \pm 0:29$ minutes (mean \pm standard deviation), and ranged from 2:27 to 4:47 minutes. This amount of time is small compared to the reported 90 minutes for patellar cartilage volume (Eckstein et al., 1999) to recover to baseline after activity. In all sessions, subjects walked at a fixed, comfortable walk speed which was constant across sessions. To account for differences in height and leg length, which affect stride length and loading frequency and therefore loading between subjects, speed was normalized to the subject's leg length using the Froude Number (Fr) (Alexander and Jayes, 1983), in order to ensure a similar loading level was applied across volunteers. The Froude Number is a dimensionless quantity which takes into account the subject's limb length (L , in m), defined as the vertical distance from the ground to the greater trochanter; the gravitational constant ($g = 9.81$, in m/s^2); and the subject's walk velocity (v , in m/s) (Alexander and Jayes, 1983). Limb length was determined by measuring the distance from the greater trochanter (via

manual palpation) down to the surface of the floor. For the first protocol, all subjects walked at a normalized speed of $Fr = 0.25$. For each walk duration, the normalized speed remained constant, meaning that increased walk durations resulted in an increased number of steps.

If subjects chose to participate in the second protocol, the same procedure described above was repeated, except that each session consisted of a fixed 30 minute walk duration at one of three different speeds. Three normalized walking speeds were chosen *a priori* to span possible walking speeds of a human adult (Alexander and Jayes, 1983; Kramer and Sylvester, 2012): $Fr = 0.10$ (corresponding to 0.9 ± 0.04 m/s for the volunteers in this study, mean \pm standard deviation), representing an adult walking with impaired mobility; $Fr = 0.25$ (corresponding to 1.5 ± 0.04 m/s for the volunteers in this study), representing an adult walking at a comfortable pace; and $Fr = 0.40$ (corresponding to 1.9 ± 0.09 m/s for the volunteers in this study), representing a walk close to the run-walk transition. Walk velocity (treadmill speed) was then calculated from these Fr , via Equation 56 (Alexander and Jayes, 1983). For each normalized speed, the walk duration remained constant, meaning that increased normalized speeds resulted in not only increased numbers of steps, but step frequencies as well.

$$v = \sqrt{(Fr)(L)(g)} \quad (\text{Eq. 56})$$

Because our prior study found significant cartilage strain after a single bout of walking using a sample size of eight (Lad et al., 2016), we aimed to recruit between eight

and ten subjects for the current study. Ten subjects participated in the first protocol, with eight subjects completing all five sessions (two subjects completed all but the 60 minute duration walk). Of the ten, eight subjects chose to participate in the second protocol, with seven of the eight subjects completing all three sessions (one subject did not participate in the slow walk speed, $Fr = 0.10$).

3.2.2 Data Analysis

Cartilage thickness was measured via creation of three dimensional (3D) knee joint models from the MR images (Figure 14). This technique has been previously validated to measure changes in cartilage thickness (Van de Velde et al., 2009) and has been shown to have a coefficient of variation of 1% (Coleman et al., 2013). This methodology has been used to measure diurnal changes in cartilage thickness (Coleman et al., 2013) as well as changes in cartilage thickness after a single bout of walking (Lad et al., 2016). To do so, the boundaries of the tibial cortex and tibial articular cartilage surface were manually traced by a single investigator in each slice of the MR images (Figure 14a) using solid modeling software (Rhinoceros 4.0, Robert McNeel and Associates, Seattle, WA). The segmentations from each slice were then stacked to create a wireframe model of the joint (Figure 14b), which was used to generate a 3D surface mesh model (Figure 14c) of both the bone and cartilage (Geomagic Studio 11, 3D Systems, Rock Hill, SC).

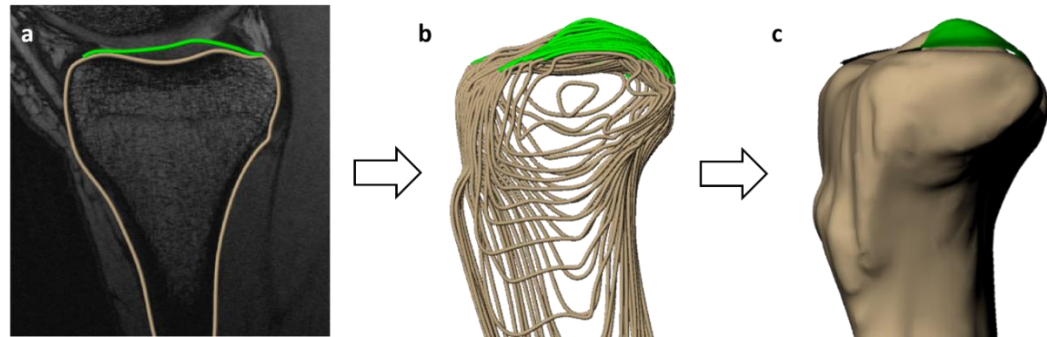


Figure 14: 3D joint model creation from MRI (sagittal view, left knee). Image shows a) segmentation of articular cartilage and bone in a single MRI slice, b) stacked wireframe model of segmented surfaces, and c) 3D surface mesh model of the tibia and tibial cartilage.

The bony surfaces of the pre- and post-activity tibia models were aligned using an iterative closest-point technique (Geomagic Studio 11, 3D Systems, Rock Hill, SC). Then, a grid system of 18 sampling points was applied to measure cartilage thickness in a site-specific manner at the same locations in the pre- and post-activity models. The grid system consisted of nine evenly-spaced sampling points on both the medial and lateral tibial plateaus (Figure 15). To measure cartilage thickness at each sampling point, custom software (Wolfram Mathematica 9, Wolfram Research, Champaign, IL) was used (Lad et al., 2016). First, cartilage thickness, defined as the distance between each point on the cartilage surface mesh and the nearest point on the bony surface mesh, was calculated. Then, the thickness values within a 2.5 mm radius of each sampling point were averaged to define the cartilage thickness at that sampling point. Subsequently, compressive strain was defined at each sampling point as the change in thickness from pre- to post-activity, normalized to the pre-activity thickness (positive values indicate

compression, corresponding to a decrease in thickness after activity). As data was collected across multiple sessions, the strain resulting from activity during a particular session was calculated with respect to that session's pre-activity scan. Overall compressive strain was reported as the average strain across all 18 points on the tibial cartilage, with compartmental strains (medial and lateral) similarly defined as the average across the nine medial and nine lateral sampling points, respectively.

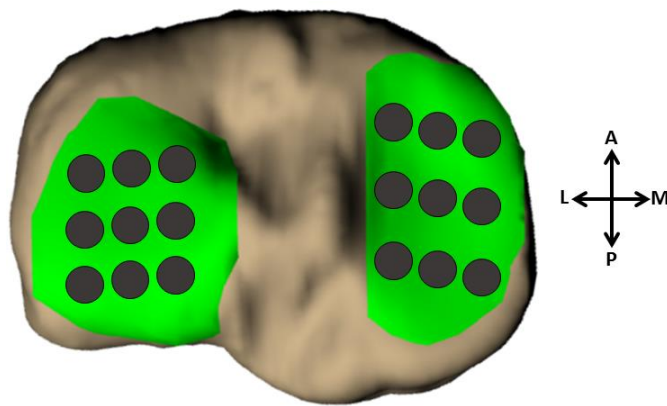


Figure 15: Grid sampling scheme showing 18 grid points. Image shows nine evenly-spaced sampling regions on both the medial and lateral tibial plateaus (superior-inferior view, left knee).

Statistical analyses were performed using SAS (SAS 9.4, SAS Institute Inc., Cary, NC) and R (Ihaka and Gentleman, 1996) with a significance level of $p < 0.05$. Data were checked for normality using the Shapiro-Wilk test. Therefore summary statistics (mean, 95% confidence interval) were calculated for overall and compartmental strain values at each duration and at each normalized speed. Two-tailed Spearman correlation was used to determine if a monotonic relationship existed between compressive strain and

increasing walk duration. Linear mixed effects (LME) modeling was used to determine whether normalized walk speed was a significant predictor of compressive strain.

Experiments using confined compression (Armstrong and Mow, 1982; Ateshian et al., 1997; Boschetti et al., 2004; Chin et al., 2011; Grenier et al., 2014; Jurvelin et al., 2003; Miller and Morgan, 2010; Mow et al., 1980; Schinagl et al., 1997; Setton et al., 1993; Soltz and Ateshian, 1998) or indentation testing (Athanasίου et al., 1991; Froimson et al., 1997; Herzog et al., 1998; Korhonen et al., 2002; Mak et al., 1987; Mow et al., 1989; Setton et al., 1994) have shown cartilage to behave in a time-dependent viscoelastic manner, where cartilage creeps (shows asymptotic increases in strain over time) in response to a constant load. During this creep response, increases in strain level off exponentially with time (Mow et al., 1980). Therefore, the empirical Kelvin-Voigt viscoelastic two-parameter exponential model (Mow and Huijskes, 2005) (Equation 57) was fit to the compressive strain versus walk duration data. This model was chosen as it is the simplest phenomenological model that captures creep behavior; however, other models (such as the standard linear solid or biphasic models) could alternately be used (Mow and Huijskes, 2005). Nonlinear mixed effects (NLME) modeling was performed using the *saemix* package in R (Comets et al., 2017).

$$\textit{Strain} = A[1 - \exp(-B(\textit{walk duration}))] \quad (\text{Eq. 57})$$

Resting baseline thicknesses were obtained for each subject in every session via the pre-activity MRIs. A zero-minute time point was created for the walk duration data

by defining the compressive strain at zero minutes of walking to be zero for all subjects. The 95% confidence interval for the strains about this zero-minute time point was calculated as follows. First, the resting cartilage thickness was calculated (per subject) for each session. Next, these resting thicknesses were averaged across sessions to yield a single representative resting thickness per subject. The standard error of these resting thicknesses was also calculated per subject. Each subject's standard error was then expressed as a percentage of their mean representative resting thickness. Finally, the mean standard error (expressed as a percent) across all 10 subjects was calculated. This value was used to calculate the 95% confidence interval across all subjects for the zero-minute time point in the same fashion as it was calculated across all subjects for every other duration.

3.3 Results

In order to measure the mechanical response of cartilage to walking, we compared cartilage thickness distributions across the tibial plateau obtained using MR imaging before and after bouts of walking exercise at different durations and speeds. To apply consistent loading between subjects, walk speed was normalized using the Froude Number (Fr) (Alexander and Jayes, 1983). Increased walk duration at a fixed normalized speed ($Fr = 0.25$) resulted in decreased cartilage thickness (Figure 16) and thus increased compressive strain. Increased normalized speed for a fixed walk duration (30 minutes)

also resulted in decreased cartilage thickness (Figure 16) and increased compressive strain.

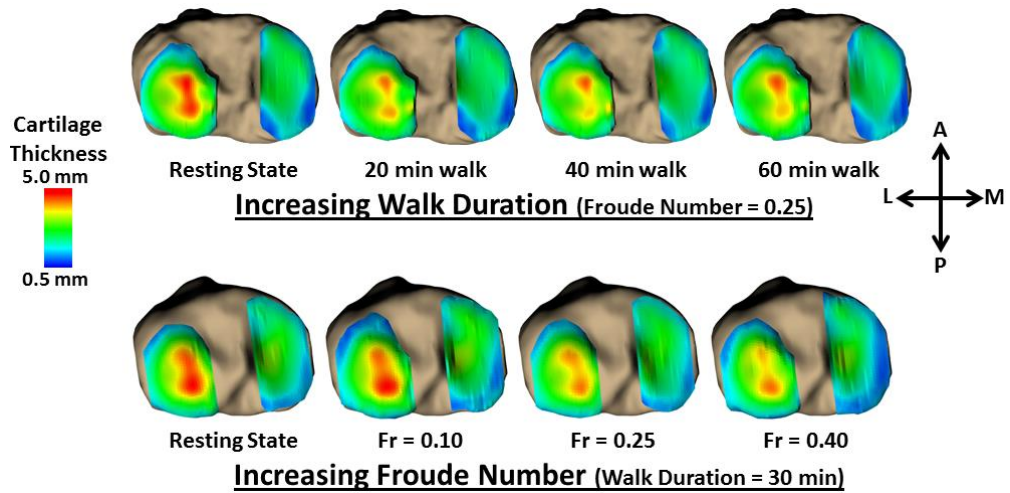


Figure 16: Representative tibial cartilage thickness maps (superior-inferior perspective of axial view of left knee). Top row: first protocol (increasing walk duration), bottom row: second protocol (increasing normalized walking speed). Increased duration and increased normalized speed each resulted in decreased cartilage thickness compared to the baseline resting state, with thickness changes leveling off with longer walk durations. Averaged across all volunteers, pre-exercise (baseline) cartilage thickness was 2.5 ± 0.3 mm (mean \pm 95% confidence interval), 2.1 ± 1.8 mm, and 3.0 ± 2.6 mm across the entire tibial plateau, the medial plateau, and the lateral plateau, respectively.

As walk duration increased (for a fixed walking speed, $Fr = 0.25$), mean tibial cartilage compressive strain increased monotonically (never decreased), eventually plateauing at longer walk durations (Figure 17). This asymptotic pattern of increased compressive strain with increased walk duration was consistent across the entire tibial plateau (Figure 17a), and when the medial and lateral portions were analyzed separately (Figure 17b and c). Spearman correlation indicated that the increase in compressive strain with increased walk duration was statistically significant ($p < 0.05$) for the entire

tibial plateau ($p = 0.001$) and for each compartment (medial: $p = 0.002$, lateral: $p = 0.04$). Additionally, compressive strain as a function of walk duration was well-fit by the Kelvin-Voigt exponential model for creep (Figure 17, see Section 3.7 Paper Appendix for model diagnostics). After 10 minutes of walking, compressive strain (mean \pm 95% confidence interval) was $2 \pm 1\%$, $2 \pm 2\%$, and $2 \pm 2\%$ for the overall tibia, medial plateau, and lateral plateau, respectively; while for 20 minutes of walking it was $3 \pm 1\%$, $2 \pm 1\%$, and $4 \pm 1\%$, respectively. Compressive strains in the tibial cartilage leveled off to $5 \pm 2\%$, $5 \pm 2\%$, and $5 \pm 2\%$ (overall tibia, medial plateau, and lateral plateau, respectively) at 60 minutes of walking.

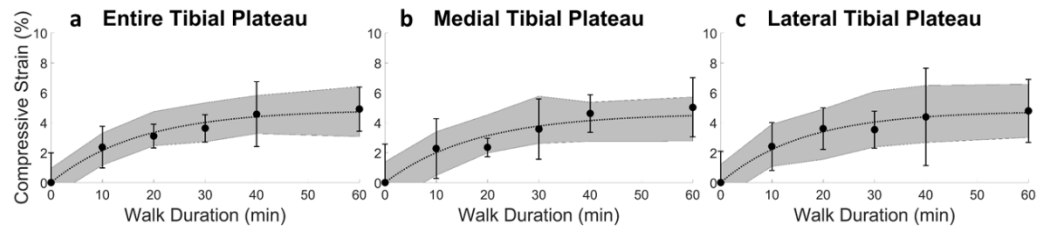


Figure 17: Overall (a) and compartmental (b, c) compressive strain (mean, 95% confidence interval) in tibial cartilage as a function of walk duration. Results are for a fixed normalized walking speed ($Fr = 0.25$). Sample size (n) = 10 for all time points except 60 min where $n = 8$. Compressive strain significantly increased (Spearman correlation, $p < 0.05$) with increasing walk duration in a nonlinear fashion (lines represent the nonlinear mixed effects model fits of the Kelvin-Voigt two-parameter creep model to the duration data while shading represents the 95% prediction interval for the median of this fit).

As normalized walking speed increased (for a fixed duration of 30 minutes), mean tibial cartilage compressive strain increased from a slow pace ($Fr = 0.10$), to a moderate pace ($Fr = 0.25$), and to a fast pace ($Fr = 0.40$; close to the walk-run transition of $Fr = 0.5$ (Alexander and Jayes, 1983)) (Figure 18). This pattern was consistent across the

entire tibial plateau (Figure 18a), and when the medial and lateral compartments were analyzed separately (Figure 18b and c). Linear mixed modeling indicated that Fr was a significant predictor for the overall tibial strain ($p = 0.004$) and medial plateau strain ($p = 0.03$), but not the lateral plateau strain ($p = 0.15$). At $Fr = 0.10$, compressive strain (mean \pm 95% confidence interval) was $1 \pm 2\%$, $0 \pm 2\%$, and $2 \pm 3\%$ for the overall tibia, medial plateau, and lateral plateau, respectively. At $Fr = 0.25$, compressive strain was $3 \pm 1\%$, $3 \pm 2\%$, and $3 \pm 1\%$, respectively (overall, medial, lateral); while for $Fr = 0.40$, compressive strain was $6 \pm 8\%$, $4 \pm 5\%$, and $8 \pm 11\%$, respectively.

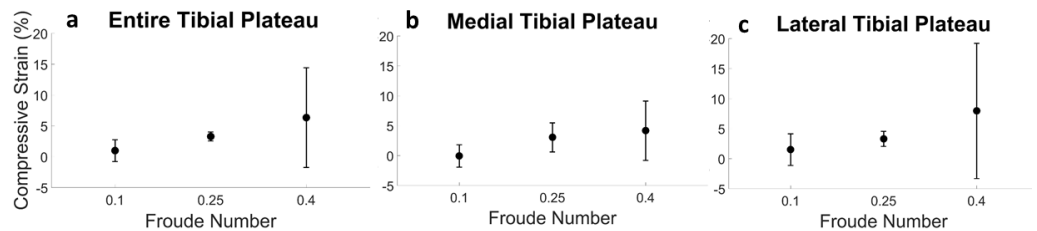


Figure 18: Overall (a) and compartmental (b, c) compressive strain (mean, 95% confidence interval) in tibial cartilage as a function of normalized walking speed (Fr). Results are for a fixed walk duration (30 minutes). Sample size (n) = 7 for Fr = 0.1, n = 10 for Fr = 0.25, and n = 8 for Fr = 0.40. Compressive strain significantly increased (linear mixed model, $p < 0.05$) with increased normalized walking speed for the overall tibia and medial tibial plateau, but not for the lateral tibial plateau.

3.4 Discussion

As mechanical loading influences chondrocyte metabolism (Guilak, 2011; Loeser et al., 2012; Sah et al., 1989), certain levels of exercise or in vivo loading may promote cartilage health (Sun, 2010). Therefore, investigating various exercise intensities on the in vivo response of healthy cartilage is a crucial first step toward OA therapies and prevention programs. Towards this end, the current study provides a direct measure of

cartilage compressive strain after walking, an activity of daily living and also a common exercise, in a duration- and speed-dependent manner. We used a combination of MR imaging and site-specific 3D modeling of subjects' cartilage before and after activity to investigate bouts of walking at different durations and speeds, in order to quantify the resultant cartilage compressive strain (Coleman et al., 2013; Lad et al., 2016; Sutter et al., 2015). Our walk duration results demonstrate that for a fixed, comfortable walking speed, as walk duration increased, cartilage compressive strain across the tibial plateau increased monotonically (Spearman correlation, $p < 0.05$). Moreover, compressive strain approached an asymptote between forty and sixty minutes of walking. Finally, our results also demonstrate that for a fixed walk duration, as normalized walking speed increased, overall tibial cartilage and medial tibial plateau compressive strain also increased (linear mixed model, $p < 0.05$).

Our observations of an asymptotic relationship between increasing walk duration and cartilage strain demonstrate in vivo creep. Cartilage creep behavior has been well-documented in vitro (Armstrong and Mow, 1982; Mow et al., 1989; Mow et al., 1980), but not in vivo. Creep occurs due to the motion of fluid within the tissue: initially, there is a high degree of fluid loss at the tissue surface, where there is a high amount of strain. Over time, the fluid loss near the surface of the cartilage redistributes throughout the rest of the tissue until an equilibrium strain and loss of fluid is reached. This redistribution levels off in an exponential manner across time (Mow et al., 1980).

Importantly, the in vivo cartilage strains observed in the present study demonstrated similar behavior, illustrated by the agreement between the Kelvin-Voigt exponential model (Mow and Huijskes, 2005) and our strain versus walk duration data (Figure 17). Since in vitro work has demonstrated a link between mechanical loading and chondrocyte metabolism (Buschmann et al., 1995; Larsson et al., 1991; Lee and Bader, 1997; Mauck et al., 2000; Sah et al., 1989; Shelton et al., 2003), our observations of cartilage creep occurring in vivo are vital for leveraging in vitro findings towards preventing, treating, and ameliorating OA degeneration.

Prior work including in vitro studies, animal studies, and exercise intervention studies has pointed towards exercise as a potential therapeutic or preventative measure for OA (Jurvelin et al., 1989; Roos and Dahlberg, 2005; Sun, 2010). Therefore, the design of this study—a dose-response investigation analyzing both exercise time (walk duration) and exercise intensity (walking speed) on in vivo cartilage strain in a site-specific manner—represents a vital piece of information for establishing therapeutic targets and clinical interventions for OA, as it quantifies the response of healthy cartilage to physiological loading (various bouts of walking). This normative data is crucial for informing future studies, as it provides physiological boundary conditions (strain values) to apply during investigations of mechanical loading and cartilage health. Furthermore, despite walking being the most popular form of exercise in the US (Bureau of Labor Statistics, 2016), there is a lack of data in the literature characterizing cartilage

response to walking. A previous study from our lab investigated the cumulative in vivo cartilage deformation after only a single bout of walking at a fixed duration (Lad et al., 2016), while the present study quantified cartilage deformation after multiple bouts of walking at different durations. In addition, the current study also investigated the effect of walking speed. Our speed results support the notion that faster cycles within a set length of time load the cartilage more. We observed that as walking speed increased, so too did the compressive strain in the tibial cartilage (Figure 18). As increased walking velocity is accompanied by increased ground reaction forces (Nilsson and Thorstensson, 1989), increased speed likely also elevates joint reaction forces and thus the forces acting on the tibial cartilage. Therefore, faster walking may involve larger joint forces than slower walking, potentially leading to the larger cartilage deformations seen at higher Fr than seen following walking at lower Fr. Lastly, we observed that the compressive strains resulting from walking were not evenly distributed across the cartilage surface (Figure 16), indicating that site-specific measurements are needed to accurately capture cartilage response across the tissue. As OA may incur focal tissue changes or defects, such as increased thinning in cartilage sub-regions compared to the overall compartment (Wirth et al., 2009), the ability to capture focal cartilage changes in a site-specific manner may shed further light into OA etiology (DeFrate, 2017; Okafor et al., 2014).

Overall, the work presented here offers several implications for OA treatment and prevention. Current therapeutic guidelines for walking as an exercise intervention for OA target symptoms such as pain and physical function (Focht, 2006). The data in this study is a first step toward developing therapeutic measures aimed at improving cartilage health, as it characterizes compressive strain in healthy cartilage to various degrees of walking exercise (normative tibial cartilage response data). However, future studies are needed to determine the response of degraded or OA cartilage to these intensities of walking, in order to inform therapeutic targets and exercise recommendations. Likewise, the in vivo stress test methodology presented here can be used in future work to formulate recommendations for safe levels of several other types of exercise, such as running or cycling, as well as to investigate the response of other cartilage surfaces in the knee, such as the femoral cartilage and the articular surfaces of the patellofemoral joint. The benefits of this noninvasive stress test are that it is both patient-specific and site-specific: our methodology can be used to determine cartilage response on an individual patient basis, and it can detect particular regions of cartilage thinning or local changes in strain. These two features taken together can inform specific therapeutic regimens to target certain degenerative phenotypes. Furthermore, this approach may also be used as an in vivo creep test to non-invasively quantify mechanical properties of cartilage. As such, it is a novel way to study the degenerative OA process, as individuals can be followed over time to investigate changes in in vivo

cartilage mechanical properties with normal aging. OA etiology can further be explored using our stress test by testing healthy controls, populations at high risk of OA (such as with obesity (Collins et al., 2018b) or prior joint injury (Sutter et al., 2019)), and those already suffering from OA to characterize differences between in vivo mechanical properties of healthy, at risk, and OA cartilage. Lastly, combining this methodology with other techniques, such as quantitative MR imaging (e.g. T1rho or T2 mapping (Collins et al., 2018a; Collins et al., 2018b; Hatcher et al., 2017; Li et al., 2007; Taylor et al., 2018)) or blood-based markers, may increase the sensitivity and specificity of OA diagnosis.

3.5 Conclusion

In conclusion, this study used a novel cartilage stress test based on MR imaging and 3D modeling to quantify tibial cartilage compressive strain after walking in a dose-dependent manner for both walk duration and speed. Further, this study provided innovative observations of in vivo creep (monotonically-increasing compressive strain) in response to increasing walk duration. These in vivo observations are consistent with data describing in vitro cartilage behavior under compression (Armstrong and Mow, 1982; Gao et al., 2015; Mow et al., 1989; Mow et al., 1980), and are also consistent with studies investigating in vivo cartilage biomechanics (Coleman et al., 2013; Eckstein et al., 1999; Kessler et al., 2006; Lad et al., 2016). While treatments for OA are limited, exercise is able to ameliorate pain associated with OA (Ettinger et al., 1997; Focht, 2006; Van Baar

et al., 1998) and represents a promising intervention capable of influencing cartilage health. However, the appropriate type, intensity, and duration of exercise cannot yet be prescribed as direct in vivo evaluation of exercise on cartilage health has not been performed. Towards this end, the data of this study represent physiological benchmarks for healthy cartilage response to walking, which may aid in the design of treatment and prevention strategies for those suffering from OA. Further, the technique presented here provides a framework for future studies investigating the effects of various types of exercise on cartilage health in a variety of populations, such as those at high risk for OA. Both the novel data and innovative methodology of the current study are useful for future work to determine exercise regimens that may be used therapeutically to treat or prevent OA.

3.6 Acknowledgements

The authors would like to thank Dr. Daniel O. Schmitt for his helpful discussions regarding this study. The authors would also like to thank the Center for Advanced Magnetic Resonance Development at Duke University for their assistance with this project. Research reported in this publication was supported by the NIH grants TL1TR001116, AR066477, and AR065527.

3.7 Paper Appendix

The following plots illustrate the NLME model evaluation tools provided by the saemix package (Comets et al., 2017) for the Kelvin-Voigt two-parameter creep model fit

of the duration data. Model evaluations are given for the fits to the overall strain, medial strain, and lateral strain. The Q-Q plots and frequency vs NPDE (normalized prediction distribution errors) plots indicate that the model fits the data well, while the NPDE vs X and NPDE vs Predicted Y plots indicate that the error is randomly distributed, further indicating good model diagnostics.

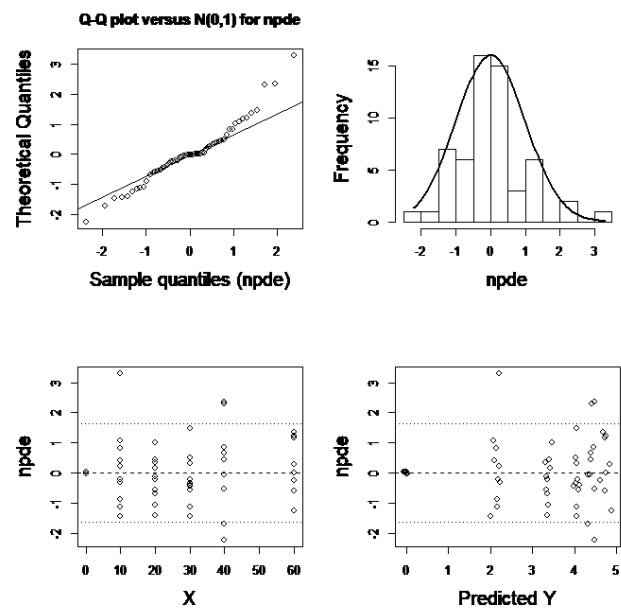


Figure 19: Saemix model diagnostics for the overall strain versus duration data.

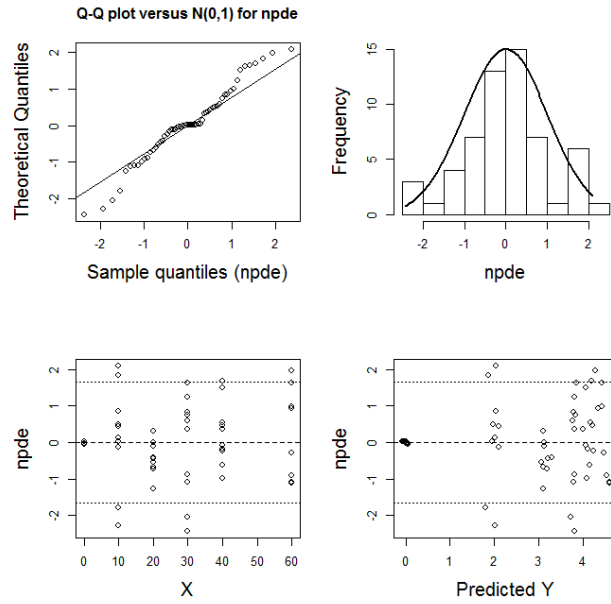


Figure 20: Saemix model diagnostics for the medial strain versus duration data.

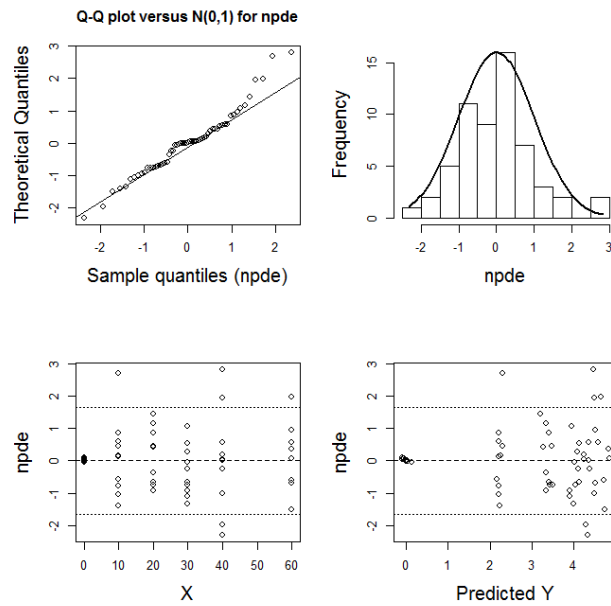


Figure 21: Saemix model diagnostics for the lateral strain versus duration data.

4. Comparison of Cartilage Mechanical Properties Measured During Creep and Recovery

This chapter represents material currently under review in Scientific Reports.

Collaborators on this work (L. E. DeFrate) are gratefully acknowledged.

This chapter supports Aim 1 (creation of a statistical model relating stiffness to properties measurable via MRI, one of which is the characteristic time) as it validates the hypothesis that similar mechanical properties result from measuring either the recovery response or the creep response (in other words, that the characteristic recovery time is an appropriate surrogate for the characteristic creep time). As illustrated in Section 5. In *Vivo Cartilage Strain and Recovery After 30 Minutes of Walking*, measuring the recovery response in vivo via MRI is more efficient than measuring the creep response in vivo via MRI, as it involves only one study visit per volunteer and fewer total MR images.

4.1 Introduction

Osteoarthritis (OA) is a degenerative disease of articular cartilage and affects over 27 million Americans (Lawrence et al., 2008). OA is currently diagnosed via the presence of pain and radiographic features, such as osteophytes and joint space narrowing, from which cartilage loss is inferred (Glyn-Jones et al., 2015; Kellgren and Lawrence, 1957; Litwic et al., 2013). Unfortunately, radiographic imaging techniques rely upon gross morphological changes to be present in the tissue, which may not occur until late in the disease (Litwic et al., 2013). Other methodologies use magnetic resonance

imaging (MRI) to assess OA rather than x-ray imaging (Peterfy et al., 2004); however, radiography remains the traditional modality used clinically (Glyn-Jones et al., 2015; Litwic et al., 2013). Currently, treatment for end-stage OA is limited, including pain management or joint replacement surgery to restore function and reduce pain (Glyn-Jones et al., 2015). While they ameliorate symptoms associated with the disease, these therapies do not directly treat or reverse cartilage degeneration. Therefore, earlier detection of OA degeneration is needed for more effective disease management and treatment.

Prior to gross morphological changes, other changes occur in cartilage tissue during the progression of OA (Lorenz and Richter, 2006). These include compositional changes, such as the loss of proteoglycan content (Hatcher et al., 2017; Rivers et al., 2000; Thompson and Oegema, 1979), the loss of collagen content and organization (Hatcher et al., 2017; Hollander et al., 1995), and changes in tissue hydration (Lorenz and Richter, 2006; Rivers et al., 2000). These changes, in turn, alter the tissue's response to mechanical load and thus its mechanical function (Collins et al., 2018a; Grenier et al., 2014; Guilak, 2011; Hatcher et al., 2017; Knecht et al., 2006; Rivers et al., 2000). Altered mechanical function may also contribute to further pathology and degeneration within the tissue (Guilak, 2011). As these compositional and mechanical changes occur prior to the onset of pain and/or gross imaging findings, detection of these mechanical changes may lead to earlier diagnosis of OA.

Cartilage mechanical assessment is classically performed in the ex vivo environment by removing explants of cartilage tissue, or by exposing the cartilage surface and indenting upon it (Guo et al., 2003; Mansour, 2003; Mow and Guo, 2002; Mow and Huiskes, 2005). As such, in vivo application of these techniques is limited, especially as diagnostic or prognostic tools. On the other hand, previous work has used MR imaging to measure cartilage response in vivo by quantifying changes in cartilage volume and thickness (Boocock et al., 2009; Cher et al., 2016; Coleman et al., 2013; Collins et al., 2018b; Eckstein et al., 2005; Eckstein et al., 1999; Eckstein et al., 1998; Hudelmaier et al., 2001; Kessler et al., 2006, 2008; Lad et al., 2016; Mosher et al., 2010; Sutter et al., 2019; Sutter et al., 2015; Van Ginckel et al., 2011; Van Ginckel et al., 2013; Widmyer et al., 2013). In these studies, an exercise activity is used to mechanically load the cartilage tissue, and MR images from before and after the activity are compared to quantify the resulting deformation. This is possible due to cartilage's biphasic nature, which consists primarily of an extracellular matrix and water (Mow et al., 1980; Sophia Fox et al., 2009). During loading, water flows out of the tissue, which imparts time-dependent or viscoelastic behavior to the cartilage (Mak et al., 1987; Mow et al., 1989; Mow et al., 1980). Because of this time-dependence, MR images can be used to measure load-induced deformation, such as changes in cartilage thickness or volume (Eckstein et al., 1999; Eckstein et al., 1998).

Due to the viscoelastic nature of cartilage tissue, mechanical characterization of cartilage requires knowledge of the strain-time history. Therefore, cartilage's mechanical response may be quantified in vivo using this MRI methodology by assessing deformation repeatedly after different intensities or doses of exercise. For example, prior work by our group (Paranjape et al., 2019) varied the duration and intensity of walking to quantify how cartilage strain changed over time after walking. This was analogous to a creep test, where the load was applied and held for a set duration, and the resulting strain was measured across time during that duration. However, this paradigm — repeated applications of pre/post MR imaging and exercise — led to an expensive and time-intensive study.

On the other hand, adapting the current in vivo MRI methodology to assess the reversal of strain during the recovery period after loading may lead to a more efficient study design while still enabling assessment of the mechanical response (Figure 22). As stated, water flows out of the tissue during loading and deformation accumulates in a time-dependent manner within the cartilage (Mak et al., 1987; Mow et al., 1989; Mow et al., 1980). Conversely, upon the removal of load during the recovery period, water flows back into the tissue, causing the reversal of the deformation over time as the cartilage returns to its baseline state. If the unloading trajectory is similar to the loading trajectory, then measuring the strain history during recovery should allow for similar mechanical characterization as measuring the strain history during creep.

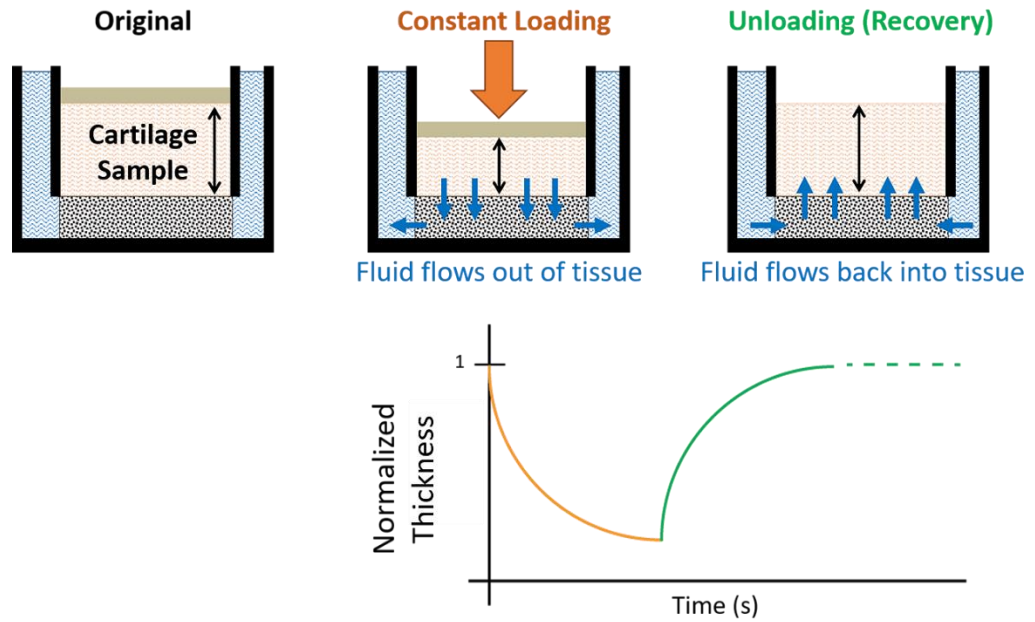


Figure 22: Comparison of the loading and unloading (recovery) response of cartilage.

Therefore, the purpose of this study was to measure and compare the cartilage mechanical response to loading (creep) and unloading (recovery), in a controlled ex vivo environment by conducting confined compression creep and recovery tests on porcine cartilage explants from the tibial plateau and femoral trochlea. Our goal was to compare the strain trajectories during loading and unloading to determine whether the recovery response may be used as a surrogate measure for the creep response when making mechanical assessments of cartilage tissue in vivo.

4.2 Methods

4.2.1 Mechanical Testing

Ex vivo confined compression creep and recovery experiments were carried out using full-thickness cartilage plugs (N = 10) from porcine femurs and tibiae. Skeletally mature porcine knee joints were obtained intact from a local abattoir. As all tissue received was from already deceased animals who were not euthanized for the purposes of this study, Institutional Animal Care and Use Committee (IACUC) approval was not required. Joints were dissected to expose the articular cartilage surfaces of the femur and tibia, and 5 mm diameter cartilage explants were harvested from the tibial plateaus and femoral trochlea of the joints. Explants were promptly wrapped in PBS-soaked gauze and stored at -20°C until testing.

Explants were thawed at room temperature for 30 minutes prior to mechanical testing. After thawing, 3 mm diameter cylindrical plugs were cut from the original 5 mm diameter plugs and loaded into a confined compression chamber filled with PBS for mechanical testing (Figure 23).

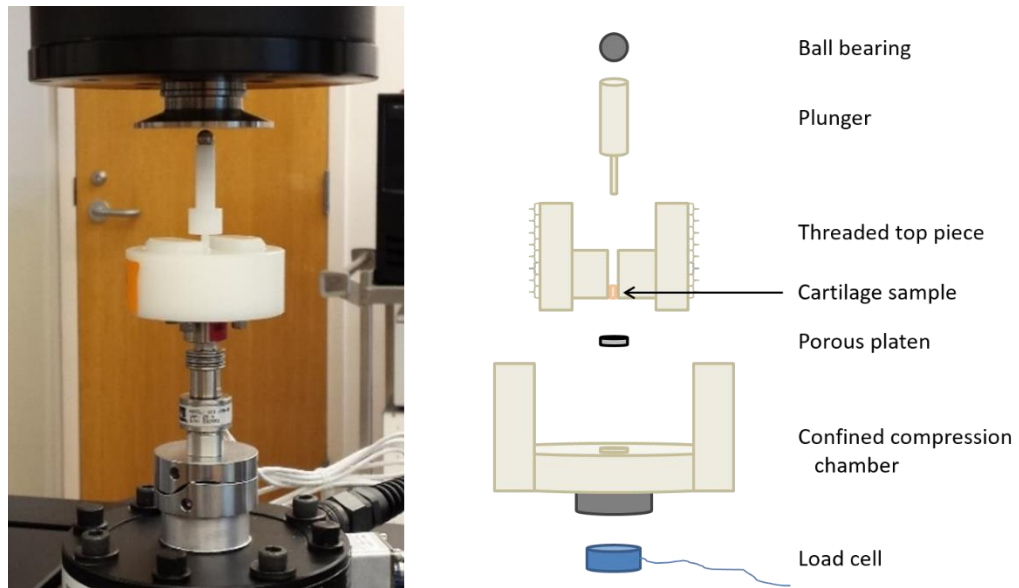


Figure 23: Confined compression fixturing.

Creep and recovery tests were performed in load control on an MTS Acumen 3 materials test system (MTS Systems Corporation, Eden Prairie, MN). The test battery included four steps: 1) cyclic preconditioning, to ensure explants reached a repeatable steady-state level of hydration throughout the depth of the tissue (Gao et al., 2015); 2) a preload (-0.1 N, 60 min), to allow explants to equilibrate to a baseline thickness under a small compressive load (Athanasίου et al., 1991; Mow et al., 1989); 3) a creep load (-0.5 N, 60 min), to measure the strain response during creep; 4) a recovery load (-0.1 N, 60 min), to measure the strain response during recovery (Figure 24a). Notably, the preload and recovery levels (-0.1 N) were the same to ensure that the change in force occurring between steps 2 and 3 was equal in magnitude and opposite in direction to that occurring between steps 3 and 4. Further, the magnitude of the change in force (0.4 N) during creep and recovery was chosen to result in less than 20% strain in the tissue at

equilibrium (Ateshian et al., 1997; Mow et al., 1989; Mow et al., 1980). Similarly, the preconditioning cycled between the same creep and recovery loads (-0.10 N and -0.50 N), and consisted of a 0.10 Hz sinusoid for 100 cycles as this rate and number have been shown to be sufficient for the tissue to reach a dynamic equilibrium in which no further ratcheting strain occurs per cycle (Gao et al., 2015). Finally, the preload, creep load, and recovery load were each held for 60 minutes to allow the explants to reach equilibrium in each phase.

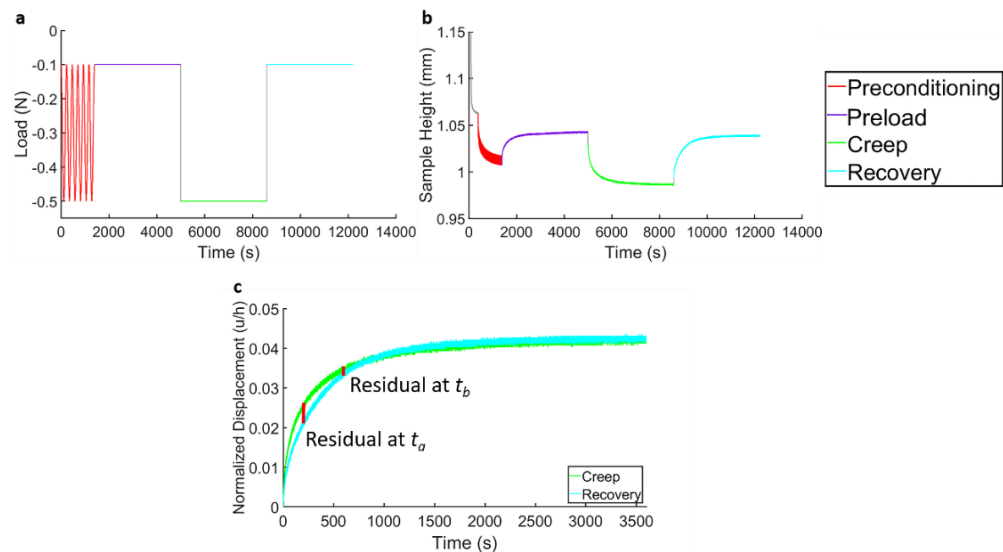


Figure 24: Confined compression test battery. a) Applied load protocol. b) Measured data from a representative explant. c) Illustration of residuals from a representative explant for assessment of similarity of creep and recovery curves via calculation of the average residual across time.

4.2.2 Data Analysis

The biphasic creep solution (Equations 51-53) (Mow et al., 1980) was fit to the measured creep and recovery deformation responses (Figure 24b, c) separately to

calculate the tissue's characteristic time (τ_0) and aggregate modulus (H_A) during both the creep and recovery phases. The fit procedure was performed in MATLAB (version R2018a, Mathworks, Natick, MA) using the nonlinear least-squares curve-fitting algorithm `lsqcurvefit`. Baseline thickness was defined as the mean explant thickness over the final five minutes of the preload phase (step 2 of the test battery, described previously). Similarity between the creep and recovery response was assessed via the average residual, defined as the mean absolute error between the creep and recovery strain curves across time for a given explant, expressed as a percent of the final (60 minute) creep strain (Figure 24c). Therefore, the average residual represents the expected error at any point in time between the creep and recovery curves for a given explant. Likewise, the mean average residual across multiple explants represents the mean expected error between the creep and recovery phases. Statistical analyses were performed in SAS (version 9.4, SAS Institute, Cary, NC) with $p < 0.05$ indicating significance. Outcome variables assessed were the aggregate modulus and characteristic time from each phase (creep and recovery). One-way repeated-measures analysis of variance (ANOVA) were carried out to test for differences in outcome between the creep and recovery phases. Cartilage location (tibial plateau vs femoral trochlea) was included as a factor to examine differences in mechanical properties across location. Further, Pearson correlations were calculated between outcome variables. Data are summarized using the mean \pm one standard deviation unless otherwise indicated.

4.3 Results

Overall, explants in this experiment experienced a mean strain of $12.8\% \pm 8.9\%$ at creep equilibrium (end of the creep phase). Explants recovered to $99.0\% \pm 0.9\%$ of their baseline thickness by the end of the recovery phase (baseline thickness: 0.75 ± 0.18 mm). Furthermore, no statistically significant differences were found in mechanical properties between the creep and recovery phases (Figure 25). The mean aggregate moduli were 0.71 ± 0.50 and 0.68 ± 0.48 MPa (creep and recovery, respectively), and the mean characteristic times were 11.6 ± 5.2 and 12.6 ± 7.3 min, respectively. Cartilage location (tibial plateau vs femoral trochlea) had a statistically significant main effect on both mechanical properties (aggregate modulus and characteristic time) measured in this study.

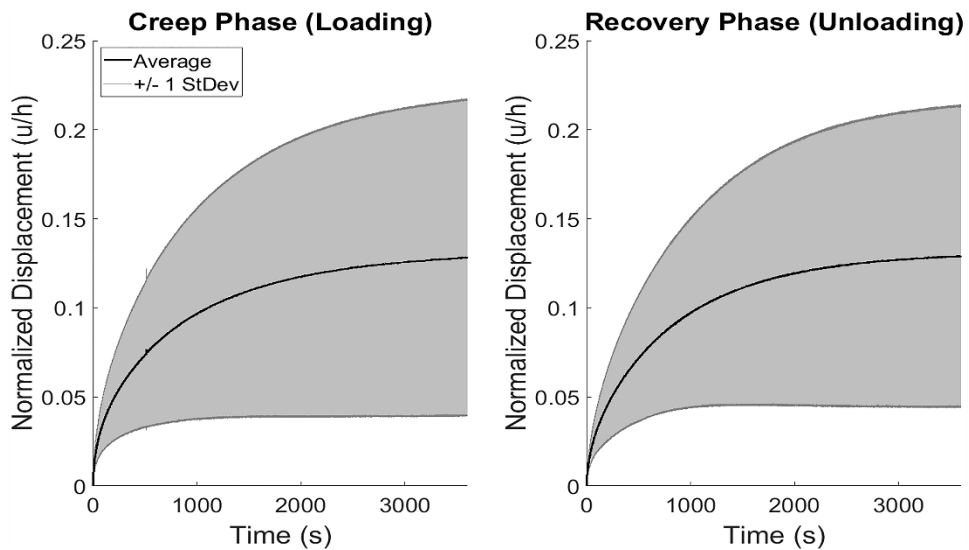


Figure 25: Creep and recovery deformation response corridors (mean \pm 1 standard deviation) across all explants. Mechanical properties (aggregate modulus and characteristic time) were not statistically significantly different between the creep and recovery phases.

Furthermore, statistically significant correlations were found between the aggregate moduli of each phase (Pearson $r = 0.996$), and between the characteristic times of each phase (Pearson $r = 0.897$) (Table 2). Additionally, the characteristic times of each phase were significantly correlated with the aggregate moduli of each phase, respectively (Table 2).

Table 2: Pearson Correlation Coefficients Between Outcome Variables.

		Aggregate Modulus		Characteristic Time	
		Creep	Recovery	Creep	Recovery
Aggregate Modulus	Creep	$r = 1.000$	$r = 0.996$ ($p < 0.0001$)	$r = -0.851$ ($p < 0.0018$)	$r = -0.720$ ($p < 0.0188$)
	Recovery		$r = 1.000$	$r = -0.843$ ($p < 0.0022$)	$r = -0.718$ ($p < 0.0194$)
Characteristic Time	Creep			$r = 1.000$	$r = 0.897$ ($p < 0.0004$)
	Recovery				$r = 1.000$

Lastly, the mean average residual between creep and recovery phases in this experiment represented an error of $5.4\% \pm 3.3\%$ of the final (60 minute) creep strain, indicating a high degree of similarity between the creep and recovery responses in the confined compression environment. Indeed, a calculation of the pairwise differences between creep and recovery at each point in time (Figure 26) illustrates that the mean pairwise difference remained low at all times.

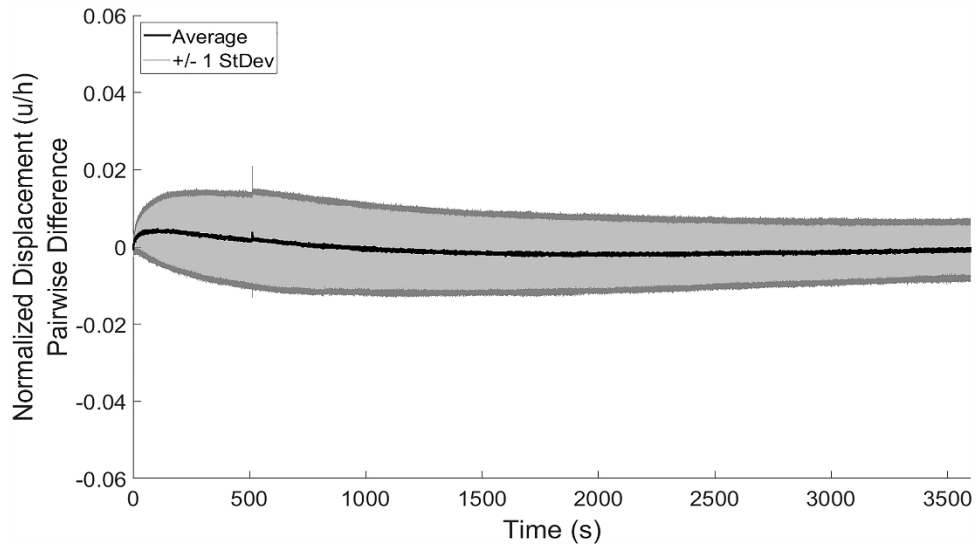


Figure 26: Pairwise differences in deformation response (creep minus recovery) at each point in time (mean \pm 1 standard deviation) across all explants.

4.4 Discussion

As the mechanical response of cartilage changes as the tissue progresses from a healthy to a degenerated state, such as during OA pathology (Hatcher et al., 2017; Hollander et al., 1995; Lorenz and Richter, 2006; Rivers et al., 2000; Setton et al., 1994; Thompson and Oegema, 1979), measurement of the tissue’s mechanical response may serve as a useful biomarker of cartilage disease. Because traditional methods of mechanical response characterization are invasive when applied to cartilage tissue, they are not well suited for in vivo applications. Therefore, the development of a noninvasive cartilage mechanical assessment is needed to characterize mechanical response in vivo, which may be accomplished using MRI (Paranjape et al., 2019) (Section 3. A New Stress Test for Knee Joint Cartilage). Towards this end, the current study evaluated the use of the recovery strain trajectory as a surrogate for the creep strain trajectory in a controlled,

ex vivo environment, in order to validate the assessment of cartilage recovery for quantifying in vivo mechanical properties.

Importantly, this study did not find statistically significant differences in either the aggregate modulus or the characteristic time between the creep and recovery phases. This finding motivates the use of the recovery phase as a surrogate for the creep phase, especially for measurement of bulk properties or response such as the total (engineering) strain within the tissue, as measured in the current study. This is useful as classically, mechanical properties are assessed during the loading response, but the unloading (or recovery) response is more accessible in vivo using MRI techniques. Therefore, understanding whether the recovery response reflects the loading response ex vivo is crucial for validating this in vivo approach. Moreover, the mean characteristic times measured in this study, 11.6 ± 5.2 min for creep and 12.6 ± 7.3 min for recovery, are on the same order as those measured in vivo: in a prior study, the mean in vivo creep trajectory of healthy human tibial cartilage had a characteristic time of 17.2 minutes (Paranjape et al., 2019). While future exploration of cartilage recovery in vivo is needed to determine whether the in vivo creep response may be represented by the in vivo recovery response, the findings of the current study support this idea.

Additionally, the current study found that the average residual—the expected error between creep and recovery response at any point in time—was low: $5.4\% \pm 3.3\%$ of the final (60 minute) creep strain. However, the average residual was not zero.

Further, larger pairwise differences were seen at early time points (0-800 seconds) than at later time points (Figure 26). These observations are consistent with prior literature which also did not find the creep and recovery phases to be perfectly reversible (Ateshian et al., 1997; Athanasiou et al., 1994; Athanasiou et al., 1991; Mow et al., 1989; Stolberg-Stolberg et al., 2018). We hypothesize that these slight differences are due to strain-dependent permeability (Mow et al., 1984), in which the tissue's permeability decreases as the strain in the tissue increases. A decrease in permeability indicates more resistance to fluid flow, making it more difficult for fluid to enter or leave the cartilage matrix. Therefore, at early times in the creep response, there is little strain within the tissue and the permeability is near its maximum, making it easier for fluid to flow out of the tissue and strain to accumulate in response to the sustained load. Conversely, at early times in the recovery response, there is a large amount of strain in the tissue (the strain is near its maximum) and the permeability is lower, making it more difficult for fluid to flow back into the tissue and for strain to dissipate. This is supported by our observations of the pairwise differences (Figure 26), in which we defined the pairwise difference as the creep response minus the recovery response at each point in time. The positive values at early times (0-800 seconds) indicate that the creep deformation was typically larger than the recovery deformation at these early times, which is consistent with a larger relative permeability at this point in creep than in recovery. In the current study, the permeability was assumed to be constant. In the presence of strain-dependent

permeability, a constant permeability assumption in combination with complete thickness recovery would lead to a slightly larger characteristic recovery time than characteristic creep time, which was also observed in this study (11.6 ± 5.2 min for creep and 12.6 ± 7.3 min for recovery). Future studies investigating incorporation of a strain-dependent permeability term when modeling the creep and recovery deformation would be beneficial to test this hypothesis. Nonetheless, the observed pairwise differences are small, especially at later times throughout the deformation (> 800 seconds), leading to a small average residual and nonsignificant differences in the characteristic creep and recovery times.

In this study, a statistically significant difference in mechanical properties between cartilage from the tibial plateau and femoral trochlea was found, which is consistent with prior literature indicating that regional differences exist in mechanical properties—for example, between femoral and tibial cartilage (Athanasίου et al., 1994; Athanasίου et al., 1995b; Athanasίου et al., 1991; Froimson et al., 1997; Treppo et al., 2000). Porcine tibial and femoral cartilage was found to have aggregate moduli during creep of 1.17 ± 0.48 and 0.40 ± 0.18 MPa, respectively. Likewise, the characteristic creep times were 7.4 ± 3.2 and 14.4 ± 4.4 min, respectively. Further, these mechanical property values—both the modulus and characteristic time—are consistent with literature values of ex vivo cartilage mechanical properties measured via confined compression (Armstrong and Mow, 1982; Collins et al., 2018a; Hatcher et al., 2017; Jurvelin et al., 2003;

Treppo et al., 2000). Finally, upon reaching recovery equilibrium (end of the recovery phase), explants recovered to within $99.0\% \pm 0.9\%$ of their baseline thickness, confirming previous reports of thickness recovery upon load removal in ex vivo creep experiments (Ateshian et al., 1997; Athanasiou et al., 1994; Athanasiou et al., 1991; Mow et al., 1989). Future work may expand on these results by testing degenerated or OA cartilage to understand whether pathology affects the loading response in the same manner as it affects the unloading response.

4.5 Conclusion

Overall, measuring the recovery response may be a useful surrogate for the creep response, especially in the in vivo context of measuring cartilage mechanical function where the recovery phase is more accessible via MRI than the loading phase. This study investigated recovery in the controlled ex vivo environment of confined compression, and did not find statistically significant differences in cartilage mechanical properties (aggregate modulus and characteristic time) between the creep and recovery phases. These results validate the use of the recovery paradigm to measure in vivo mechanical properties, with the eventual goal of leveraging mechanical changes as prognostic or diagnostic indicators of cartilage degeneration.

4.6 Acknowledgements

The authors would like to gratefully acknowledge Lia Meirose for her helpful discussions concerning this study. This study was supported by the NIH grants AR065527, AR074800, and AR075399.

5. In Vivo Cartilage Strain and Recovery After 30 Minutes of Walking

This chapter represents material currently in preparation for submission to a scientific journal. Collaborators on this work (K. M. Davis, C. E. Spritzer, and L. E. DeFrate) are gratefully acknowledged.

This chapter supports Aim 1 (creation of a statistical model relating stiffness to properties measurable via MRI, one of which is the characteristic time) as it establishes that the characteristic recovery time can be measured in vivo using MRI. Further, it supports Aim 2 (application of the statistical model to healthy in vivo MRI data) as it provides normative in vivo MRI data to which the statistical model will be applied.

5.1 Introduction

Osteoarthritis (OA) is a debilitating disease affecting articular cartilage, the tissue lining the ends of long bones in synovial joints (Mow and Huiskes, 2005). Clinically, OA presents with joint pain, stiffness, and limited range of motion (Litwic et al., 2013), which makes normal daily activities difficult and reduces quality of life (Glyn-Jones et al., 2015). Current treatments for end-stage OA focus primarily on pain management and joint replacement surgery (Glyn-Jones et al., 2015), both of which may alleviate symptoms but do not directly ameliorate cartilage degeneration (Glyn-Jones et al., 2015). One reason treatment options remain limited is that the clinical diagnosis of OA relies on the presence of pain and radiographic findings, which may not be present until late in the disease when it is difficult to treat or reverse (Litwic et al., 2013). Therefore, OA

treatment and prevention strategies, as well as identification of those at risk of OA, may be improved if OA pathology could be detected at earlier stages of the disease.

During OA degeneration, several changes occur in cartilage tissue before clinical signs (radiographic findings and pain) are present (Lorenz and Richter, 2006). These include altered cartilage composition, such as decreases in proteoglycan content, changes in collagen organization, and changes in water content (Hatcher et al., 2017; Hollander et al., 1995; Lorenz and Richter, 2006; Rivers et al., 2000; Thompson and Oegema, 1979). The mechanical response of cartilage to loading is also affected, as decreases in stiffness and changes in permeability are observed in OA cartilage (Collins et al., 2018a; Guilak, 2011; Hatcher et al., 2017; Knecht et al., 2006; Rivers et al., 2000; Setton et al., 1994). Alterations in mechanical response may contribute to further pathology (Guilak, 2011), as cartilage metabolism has been shown to be affected by its mechanical environment (Buschmann et al., 1995; Larsson et al., 1991; Lee and Bader, 1997; Sah et al., 1989). As a result, measurement of changes in cartilage composition or mechanical response may serve as indicators of OA pathology prior to radiographic features or pain (Knecht et al., 2006), and may help identify subjects at risk of developing OA.

While assessment of cartilage mechanical response is classically performed in the ex vivo environment, magnetic resonance imaging (MRI) combined with loading has been used to quantify cartilage mechanical response (Chan et al., 2016; Paranjape et al.,

2019). Under load (such as from exercise), water is forced out of the extracellular matrix. As this flow of water occurs over time, it gives rise to a time-dependent deformation of the cartilage (Mow et al., 1980). MRI can then be used to measure cartilage morphology before and after the exercise-induced flow of water, enabling measurement of cartilage deformation due to loading (Eckstein et al., 2005; Eckstein et al., 1999; Eckstein et al., 1998). For example, in recent work from our lab (Paranjape et al., 2019), cartilage was mechanically loaded via repeated bouts of walking at different durations while MRI taken before and after each walk allowed for measurement of the strain incurred by the different walk durations. Furthermore, quantitative MRI techniques have emerged as methods that may reflect cartilage composition and health (Collins et al., 2018a; Li et al., 2007; Li et al., 2009). Specifically, quantitative MRI measures such as T1rho and T2 relaxation times are sensitive to changes in proteoglycan concentration, collagen content and organization, and water content (Collins et al., 2018a; Guermazi et al., 2015; Li et al., 2007; Wayne et al., 2003), and can be obtained noninvasively.

In addition to these prior measures, the flow of water back into the tissue upon recovery is also time-dependent, and can be quantified similarly using MRI. Indeed, recent ex vivo work by our group (Cutcliffe and DeFrate, In Review) showed that measuring the unloading response, or recovery after loading, results in similar mechanical property characterization (aggregate modulus and characteristic time) as measuring the loading response, as is traditionally done. Not only would assessing

cartilage recovery in vivo complement our prior work that investigated cartilage creep in vivo (Paranjape et al., 2019), it may also reduce MRI and analysis time, as only one pre-activity MRI and one bout of activity is necessary (compared to multiple bouts of activity and pre/post MRI when measuring the creep response). Therefore, the purpose of this study was to measure the in vivo tibial cartilage mechanical response during recovery, analogous to that previously measured during loading (Paranjape et al., 2019). It was hypothesized that cartilage would exhibit a time-dependent recovery characterized by exponential approach, and that the characteristic time of this approach would be comparable to characteristic times measured ex vivo. Additionally, baseline MRI biomarkers of cartilage composition (T1rho and T2 relaxation times) and cartilage thickness were measured in healthy subjects in order to explore their potential relationships with the characteristic recovery time.

5.2 Methods

5.2.1 Data Collection

All study procedures were approved by the Duke University Health System Institutional Review Board (IRB). Eleven healthy subjects (5 male/6 female; mean age: 25 years, range: 22-32 years; mean BMI: 22.1 kg/m², range: 19.8-24.7 kg/m²) provided informed written consent prior to their participation.

The study consisted of a single visit for each subject (Figure 27—adapted from (Heckelman et al., In Prep)). Subjects were instructed to refrain from strenuous activity

the day before the study and arrived at the study center at 7am to minimize cartilage loading prior to the study (Coleman et al., 2013). Upon arrival, subjects lay supine for 45 minutes to allow for cartilage equilibration (Sutter et al., 2015). Then, subjects were transported by wheelchair to the MR scanner where they underwent baseline (pre-activity) MRI, using a 3 Tesla scanner (Trio Tim, Siemens, Erlangen, Germany) and an 8-channel knee coil (Invivo Corporation, Gainesville, FL). Specifically, each subject's dominant knee was imaged while they lay supine with their leg in a relaxed and extended position. Leg dominance was determined by the preferred leg used to kick a ball (Gabbard and Hart, 1996). All MRI were acquired in the sagittal plane, and three different sequences were used to obtain three types of images during the baseline MRI: a double-echo steady-state (DESS) scan, a T1rho scan, and a T2 scan (see Table 3 for scan parameters). Total baseline scan time was approximately 35 minutes.

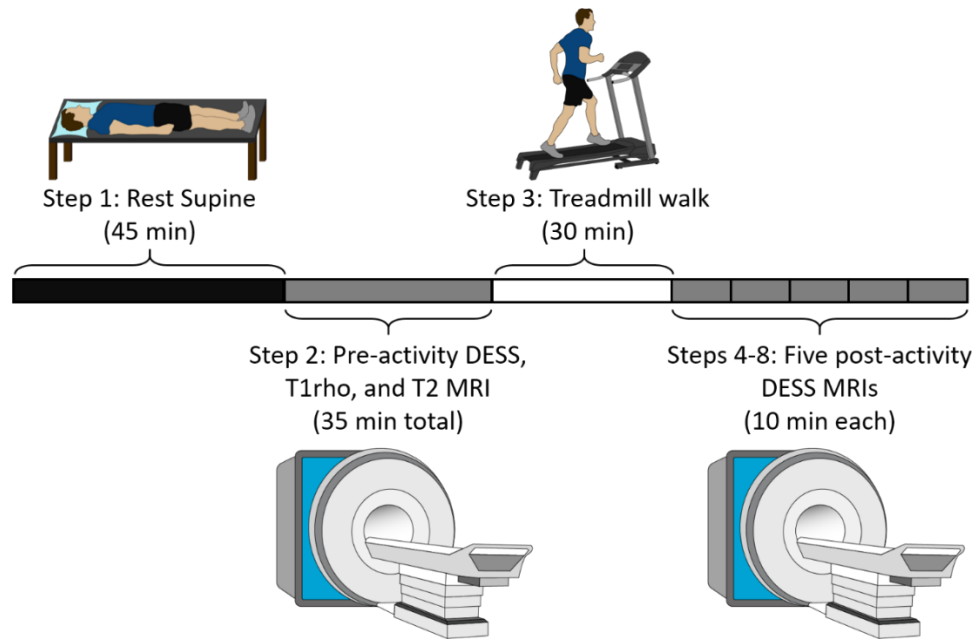


Figure 27: Study timeline for each subject (adapted from Heckelman et al., In Prep).

Table 3: MRI Parameters.

Parameter	DESS Scan	T1rho Scan	T2 Scan
Field of view	16 cm x 16 cm	14 cm x 14 cm	16 cm x 16 cm
Matrix size	512 px x 512 px	256 px x 256 px	384 px x 384 px
Slice thickness	1 mm	3 mm	3 mm
Flip angle	25°	15°	180°
Repetition time	17 ms	3500 ms	3500 ms
Echo time(s)	6 ms	5.9 ms	13.8, 27.6, 41.4, 55.2, 69.0, 82.8, 96.6 ms
Spin lock times	---	5, 10, 40, 80 ms at 500 Hz	---
Duration	~10 min	~13 min	~12 min

After the baseline MRI, subjects walked on a treadmill for 30 minutes in a room adjacent to the MR scanner. This duration was chosen because it induces statistically

significant strain within tibiofemoral cartilage (Lad et al., 2016; Paranjape et al., 2019). Subjects walked at a fixed, comfortable speed normalized to their lower limb length to ensure consistent loading across subjects (as height, lower limb length, and therefore stride length may vary). Normalization was accomplished using the Froude number (Fr) (Alexander and Jayes, 1983), which is a dimensionless quantity relating walk speed (v , in m/s), lower limb length (L , in m, defined as the vertical distance from the surface of the floor to the greater trochanter, identified by manual palpation), and the gravitational constant ($g = 9.81$, in m/s^2) according to Equation 56. Each subject walked at a normalized speed of $Fr = 0.25$ (corresponding to 1.48 ± 0.05 m/s for these subjects, mean \pm standard deviation) which represents a comfortable walking pace for adults (Alexander and Jayes, 1983; Kramer and Sylvester, 2012).

$$Fr = v^2 / gL \quad (\text{Eq. 56})$$

Immediately after the walking exercise, subjects underwent five consecutive post-activity MRIs to capture the recovery of cartilage thickness after loading. The post-activity imaging consisted of five DESS scans acquired consecutively, with no wait time between sequences. As each DESS scan lasted approximately 10 minutes, the post-activity MRIs captured a total period of 50 minutes after the walking activity. Time between walk and MRI initiation was $3:36 \pm 0:47$ minutes (mean \pm standard deviation).

5.2.2 Data Analysis—DESS Scans

The DESS MR images were used to create virtual three dimensional (3D) knee joint models (Carter et al., 2015) from which tibial cartilage thickness was measured (Figure 28). This technique has been previously shown to measure changes in cartilage thickness with a coefficient of variation of 1% (Coleman et al., 2013). Quantifying tibial cartilage thickness involves three steps: 1) manual segmentation by a single investigator of the boundaries of the tibial cortex and tibial articular cartilage surface in each DESS MR image slice (Figure 28a) using solid modeling software (Rhino 4.0, Robert McNeel and Associates, Seattle, WA); 2) stacking the segmented contours across slices to create a wireframe model of the joint (Figure 28b); and 3) generating a 3D surface mesh model from the wireframe models (Figure 28c) using solid modeling software (Geomagic Studio 11, 3D Systems, Rock Hill, SC). This procedure was carried out for each DESS scan (pre-activity scan and five post-activity scans) to generate a 3D surface mesh model representing the tibia and tibial cartilage at each time point (pre-activity and 10, 20, 30, 40, and 50 minutes post-activity).

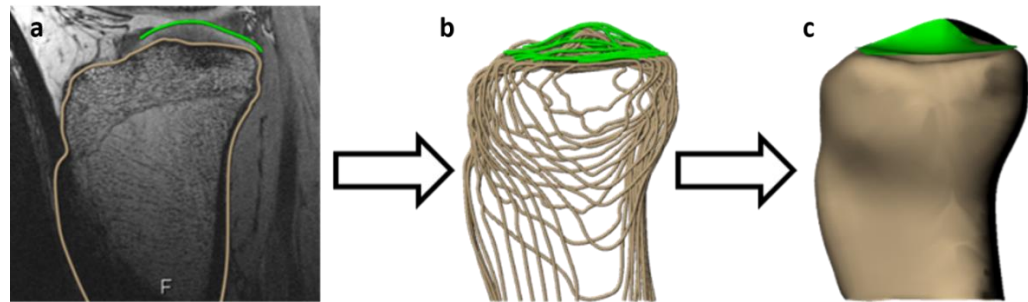


Figure 28: Tibial cartilage thickness measurement procedure. Image shows a) segmentation of tibial cortex and tibial articular cartilage, b) segmentation stack across several slices, and c) 3D surface mesh model creation.

Next, each post-activity tibia model was aligned with the pre-activity tibia model using an iterative closest-point technique (Geomagic Studio 11, 3D Systems, Rock Hill, SC). This was done in order to sample cartilage thickness at the same locations in the pre- and each post-activity model. To quantify cartilage thickness, 18 sampling points were applied across the surface of the tibial cartilage (9 points arranged in a 3x3 grid on the medial and lateral plateaus, respectively; Figure 29), and custom software (Wolfram Mathematica 9, Wolfram Research, Champaign, IL) was used to measure cartilage thickness at each sampling point (Lad et al., 2016; Paranjape et al., 2019). Thickness was defined as the distance between each node of the cartilage surface mesh and the nearest node of the tibial surface mesh. The thickness value of all cartilage surface nodes within a 2.5 mm radius were averaged to represent the cartilage thickness at each sampling point. Cartilage strain was calculated for each sampling point as the thickness change from post- to pre-activity, normalized to the pre-activity thickness. All 18 sampling

points were averaged to represent the mean cartilage strain per subject at each recovery time point.

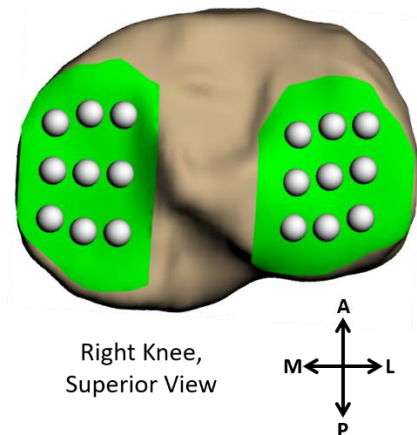


Figure 29: Grid sampling system used to define cartilage thickness in each model.

Importantly, ex vivo studies using mechanical testing (Armstrong and Mow, 1982; Ateshian et al., 1997; Athanasiou et al., 1991; Mow et al., 1980; Soltz and Ateshian, 1998) and a recent in vivo MRI study from our group (Paranjape et al., 2019) have demonstrated the asymptotic behavior of cartilage, commonly described using biphasic theory (Mow et al., 1980). Under biphasic theory, the characteristic time (Equation 53b) describes how quickly equilibrium (the asymptote) is reached, and is related to the stiffness, thickness, and permeability of the cartilage (Mow et al., 1980). As only five time points were quantified in this study, the empirical Kelvin-Voigt viscoelastic two-parameter exponential model (Mow and Huiskes, 2005) describing recovery (Equation 58) was fit to the in vivo compressive strain versus time post-activity (10, 20, 30, 40, and 50 minutes) data, to quantify the Kelvin-Voigt recovery time constant ($1/B$) of the tissue

(Paranjape et al., 2019), which approximates the characteristic recovery time. Curve-fitting was carried out using custom software written in MATLAB (version R2018a, Mathworks, Natick, MA).

$$Strain = A[\exp(-B(\textit{time after activity}))] \quad (\text{Eq. 58})$$

5.2.3 Data Analysis—T1rho and T2 Scans

The T1rho and T2 MR images were used to calculate T1rho and T2 relaxation times (Borthakur et al., 2003; Hatcher et al., 2017; Li et al., 2007), using custom software written in MATLAB. First, the cartilage was manually segmented in each slice of the scan corresponding to the first acquired spin lock time (T1rho) or echo time (T2), to define the subset of pixels representing cartilage. These same cartilage masks were then applied to the scans from subsequent spin lock times (T1rho) or echo times (T2). Next, the signal intensity in each cartilage pixel was extracted for every spin lock time (for T1rho images) or for every echo time (for T2 images). Finally, for each pixel, the signal intensities across time (either spin lock or echo) were fit with an exponential decay curve (Equation 59), where the relaxation time was defined as the decay constant of the exponential curve (Li et al., 2007). The mean relaxation time across all pixels from all slices was used to represent each subject's relaxation time (both for T1rho and T2).

$$S = S_0 e^{-\left(\frac{t}{\tau_x}\right)} \quad (\text{Eq. 59})$$

where S = signal intensity, t = time—either spin lock (T1rho) or echo (T2),

and τ_x = decay constant—either T1rho or T2 relaxation time.

5.2.4 Statistical Analysis

Statistical modeling was performed in SAS (SAS 9.4, SAS Institute Inc., Cary, NC) with a significance level of $p < 0.05$. Outcome measures (characteristic recovery time, baseline cartilage thickness, baseline T1rho relaxation time, and baseline T2 relaxation time) were assessed for normality using the Shapiro-Wilk test. Two-tailed Pearson correlations were used to test for significant correlations between the outcome measures. Finally, multiple linear regression modeling was performed to determine whether baseline MR-derived measures (cartilage thickness, T1rho relaxation time, T2 relaxation time) were predictive of the characteristic recovery time.

5.3 Results

Overall, the magnitude of cartilage strain incurred by the 30 minute walk decreased with time after activity, indicative of the recovery of cartilage thickness with time after activity. Specifically, at 10 minutes post-activity, the mean strain was $-4\% \pm 1\%$ ($\pm 95\%$ confidence interval), while at 50 minutes post-activity, it had recovered to $-1\% \pm 1\%$ (Figure 30). Indeed, the mean strain trajectory across time (calculated as the mean strain value across subjects at each post-activity time point) was well-fit by the empirical Kelvin-Voigt exponential model for recovery (Figure 30), with a characteristic recovery time of 25.2 minutes (root mean square error, RMSE = 0.24; RMSE of a line fit to these data = 0.46).

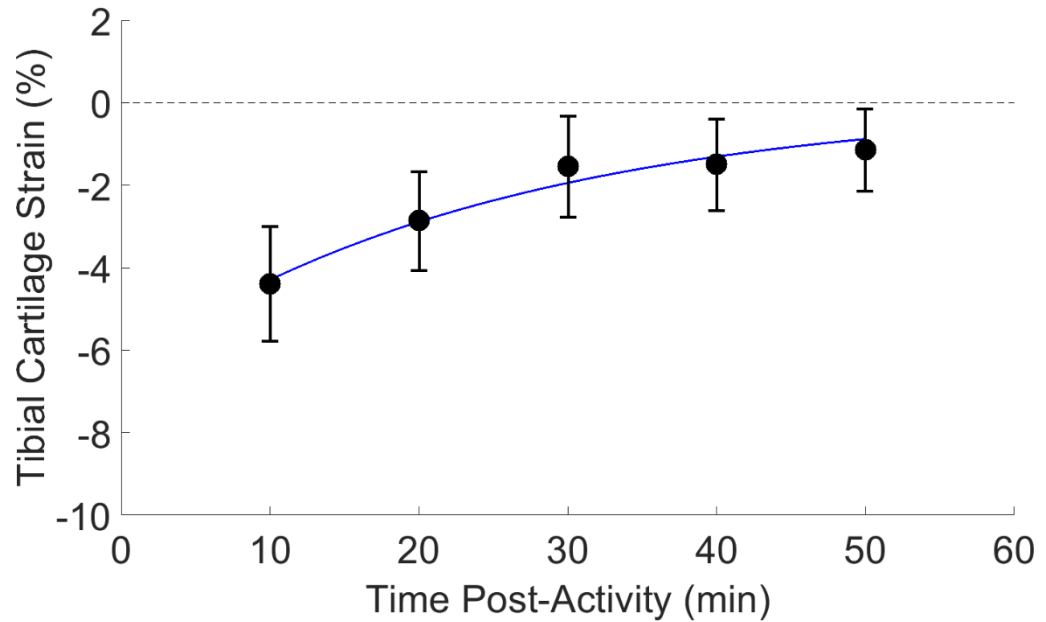


Figure 30: Tibial cartilage strain (% mean \pm 95% confidence interval) across time after activity, including a fit of the empirical Kelvin-Voigt model for recovery. The magnitude of cartilage strain decreased with time post-activity.

The correlation analysis and multiple linear regression model predicting the characteristic recovery time as a function of baseline measures (cartilage thickness, T1rho relaxation time, T2 relaxation time) was based on a subset of our cohort (8 subjects), as three subjects did not complete T2 scans. No significant correlations between any of the outcome measures were found, and the multiple linear regression model did not find any of the baseline measures to be significant predictors of the characteristic recovery time (Table 4).

Table 4: Parameter Estimates from a Multiple Linear Regression Predicting the Characteristic Recovery Time.

Variable	Parameter Estimate	Standard Error	p value
Baseline Thickness (mm)	37.46	24.61	0.20
Mean T1rho Relaxation Time (ms)	-2.31	1.33	0.16
Mean T2 Relaxation Time (ms)	0.79	2.54	0.77

5.4 Discussion

As the diagnosis of OA depends on features that are typically not present until advanced stages of the disease (i.e. radiographic findings and pain) (Litwic et al., 2013), assessment of changes that are observable at earlier stages of disease progression is important for improved identification of subjects at risk of OA, and ultimately for enhanced OA treatment and prevention. Mechanical response and cartilage composition may represent metrics that illustrate differences between healthy and early-stage OA cartilage (Knecht et al., 2006). Therefore, in this study we quantified the in vivo cartilage recovery response to 30 minutes of walking using MRI, as well as measured baseline values of cartilage thickness, T1rho relaxation time, and T2 relaxation time in a cohort of relatively young, healthy adult human subjects.

Using this data, we fit the Kelvin-Voigt empirical recovery model to the mean strain trajectory across time to quantify the in vivo characteristic recovery time of tibial

plateau cartilage, and found it to be 25.2 minutes. This value is consistent with human cartilage values obtained via ex vivo mechanical testing (Table 5). Using the reported values of mean explant height, stiffness, and permeability from two studies of creep in human cartilage, we calculated the corresponding characteristic creep times via Equation 53b (Armstrong and Mow, 1982; Mow et al., 1980) to be 26.8 minutes for tibial plateau cartilage (Akizuki et al., 1986a) and 17.7 minutes for patellar cartilage (Armstrong and Mow, 1982). These are similar to the characteristic recovery time measured in the present in vivo study (25.2 minutes for tibial plateau cartilage). This consistency validates our in vivo MRI approach, and reveals the utility of the characteristic recovery time as an in vivo metric describing cartilage’s mechanical function.

Table 5: Literature Values of Human Cartilage Characteristic Creep Time.

Reference	Cartilage Location	Sample Height, h (mm)	Stiffness, H_A (MPa)	Permeability, k ($\times 10^{-15} \text{ m}^4/\text{Ns}$)	Characteristic Time, τ_0 (min)
Akizuki et al. 1986a	Tibial Plateau	2.27	0.65	2.00	26.8
Armstrong & Mow 1982	Patella	3.12	0.79	4.70	17.7

Furthermore, our recovery trajectory is comparable with other observations in the literature. For example, a recent study (Van Ginckel et al., 2013) found that in response to 30 minutes of running, femoral and tibial cartilage volume of healthy subjects recovered to within 1% of baseline after 45 minutes. In the current study, tibial

cartilage thickness also recovered to within 1% of baseline after a similar amount of time (strain after 50 minutes of recovery, mean \pm 95% confidence interval: $-1\% \pm 1\%$).

Likewise, an MRI study investigating a running activity found that tibial cartilage volume recovered to within 1% of baseline after 60 minutes (Kessler et al., 2008). Though running may involve higher forces than walking (Nilsson and Thorstensson, 1989), several observations in the literature show similar amounts of strain immediately post-exercise between walking and running (Eckstein et al., 2005; Harkey et al., 2017). This may be because cartilage strain accumulated during cyclic loading levels off to a similar value given enough loading cycles, regardless of the activity (Eckstein et al., 1999; Harkey et al., 2018). Alternatively, it may be because running involves increased loading frequency compared to walking (Nilsson and Thorstensson, 1989), leaving less time per cycle for fluid to leave the cartilage. Indeed, ex vivo studies of cyclic loading in cartilage have reported that, for the same applied load and number of cycles, the total accumulated strain decreases as the loading frequency increases (Gao et al., 2015; Soltz and Ateshian, 2000).

Moreover, the in vivo recovery response measured here is similar to our prior work investigating the in vivo loading response, which was also well-fit by the Kelvin-Voigt model for creep (Paranjape et al., 2019). The similarity between the in vivo creep and recovery strain trajectories is in line with our ex vivo results, in which comparable mechanical property measurements resulted from assessing either the loading or the

unloading response (Cutcliffe and DeFrate, In Review). Yet, it is important to note that there are slight differences in the manner of load application during the in vivo loading and unloading responses. In the work presented here, we monitored the recovery response during static unloading (in which the load was constant over time), which we assumed to be indicative of the creep response during static loading (Cutcliffe and DeFrate, In Review). Conversely, our previous in vivo study (Paranjape et al., 2019) used a cyclic exercise activity, as walking represents an activity for which the knee cartilage undergoes periods of loading alternating with periods of unloading. Similar to static loading, cartilage accumulates strain over time in an asymptotic manner in response to cyclic loading (Gao et al., 2015). However, the rate of strain accumulated during cyclic loading may not equal the rate of strain accumulated during static loading. Despite differences in loading, in both studies the Kelvin-Voigt empirical model showed a better fit to the strain data than a linear model (smaller RMSE value), indicating that the strain data more closely resemble an exponential function (approach or decay) than they do a linear function, regardless of whether in response to cyclic loading or static offloading. This exponential behavior is important as the strain data was not acquired instantaneously—rather, each MRI acquisition took a finite amount of time, and a small amount of time elapsed between walk completion and MRI initiation in this study (3:36 ± 0:47 minutes, mean ± standard deviation). Because the exponential is a self-similar curve, these constraints have minimal influence on the measured characteristic time, as

the same proportion of strain recovers in a defined duration of time, regardless of when during the recovery that duration takes place (for example, the same proportion of strain will recover in the first 10 minutes as in the second 10 minutes).

Finally, the characteristic recovery time was not significantly correlated with the baseline MRI metrics (T1rho relaxation time, T2 relaxation time, cartilage thickness) measured here, nor were these metrics significant predictors of the characteristic recovery time. Therefore, in the present study, predicting the mechanical response of cartilage from static baseline measures was challenging. However, this study analyzed only relatively young and healthy volunteers. As T1rho and T2 relaxation times change with OA progression (Li et al., 2007), these baseline measures may be more indicative of mechanical response if analyzed on a regional or zonal (superficial vs deep) basis, or when a larger variation in cartilage health is assessed. On the other hand, recent work investigating changes in stiffness and histology in murine cartilage after surgical destabilization of the medial meniscus found that significant changes in stiffness were apparent sooner after the surgery (within a week) than were histological changes (within four to eight weeks) (Doyran et al., 2017). This supports the hypothesis that mechanical changes occur earlier in the progression of OA than do histological changes. It may also explain why associations with T1rho and T2 were not observed in the current study, as these qMRI measures are indicative of changes in cartilage composition. Nonetheless, as cartilage mechanical response changes as cartilage health

changes (Knecht et al., 2006), the characteristic time presented here may represent another useful indicator of in vivo cartilage health that is important to quantify, in addition to baseline measures of composition and morphology. However, future testing including characterization of recovery time in OA patients and those at risk of OA (such as with obesity or joint injury) is required to fully understand the utility of the characteristic time as an indicator of cartilage health.

5.5 Conclusion

Overall, the results of our present study show that comparable mechanical properties (characteristic times) are measured using our in vivo MRI approach as they are using ex vivo mechanical testing. Additionally, as measuring the recovery response is more accessible than the loading response in the context of in vivo MRI measurements, this study presents a more efficient method for quantifying in vivo cartilage mechanical properties. Lastly, while future studies are needed to assess how the characteristic time changes with OA severity (and therefore its value as a marker of early-stage OA), it represents a promising metric describing the mechanical state of the cartilage and may be indicative of health status. As such, the results presented here quantify normative values of the in vivo characteristic time of healthy tibial plateau cartilage against which future values of OA cartilage can be compared.

5.6 Acknowledgements

The authors would like to thank the Center for Advanced Magnetic Resonance Development at Duke University for their assistance with this project. This study was supported by the NIH grants AR065527, AR074800, and AR075399.

6. In vivo Estimation of Cartilage Stiffness using Noninvasive Imaging Metrics

This chapter represents material currently in preparation for submission to a scientific journal. Collaborators on this work (P. K. Kottamasu, A. L. McNulty, C. E. Spritzer, and L. E. DeFrate) are gratefully acknowledged.

This chapter carries out Aim 1 (creation of a statistical model relating stiffness to properties measurable via MRI) by making both MRI measurements and ex vivo mechanical property measurements on a cohort of porcine cartilage explants, and developing a statistical model relating the measured MRI and mechanical properties. Additionally, this chapter carries out Aim 2 (application of the statistical model to healthy in vivo MRI data) by applying the developed statistical model to the normative in vivo MRI data measured in Section 5. In Vivo Cartilage Strain and Recovery After 30 Minutes of Walking.

6.1 Introduction

Magnetic resonance imaging (MRI) is increasingly being used to assess cartilage morphology, particularly as it relates to the etiology of osteoarthritis (OA) (Guermazi et al., 2015; Taylor et al., 2009). This is because a hallmark feature of OA is the degeneration of articular cartilage (Lawrence et al., 2008; Loeser et al., 2012). Currently, the clinical diagnosis of OA requires both the existence of radiographic findings (i.e. joint space narrowing, which is indicative of cartilage loss, and the presence of osteophytes) as well as pain (Glyn-Jones et al., 2015; Kellgren and Lawrence, 1957; Lawrence et al., 2008;

Litwic et al., 2013). However, these features are usually not present until advanced stages of OA (Litwic et al., 2013; Lorenz and Richter, 2006). A significant advantage of MRI techniques compared to radiography is that they can visualize cartilage directly. As such, MRI methods may be able to detect OA pathology before osteophytes or joint space narrowing can be detected via radiography (Atkinson et al., 2019; Guerhazi et al., 2015; Litwic et al., 2013). Therefore, MRI methods may have utility towards understanding OA etiology and in providing markers of disease progression.

Notably, several pathological changes occur in cartilage during OA before large changes in morphology are visible (Lorenz and Richter, 2006). Many of these changes are mechanical; for instance, cartilage loses its stiffness during OA progression (Hatcher et al., 2017; Knecht et al., 2006; Rivers et al., 2000), meaning that it deforms more under the same amount of load than healthy cartilage. Moreover, changes in the tissue's permeability have been observed in human cartilage with naturally-occurring OA (Rivers et al., 2000), as well as in *ex vivo* studies where OA was modeled through enzymatic degradation of healthy cartilage (Bonassar et al., 1995; Grenier et al., 2014; Wayne et al., 2003). This implies that the relative ability of fluid movement through the tissue changes with OA, which has important implications towards fluid pressurization within the cartilage and therefore its ability to bear load (Soltz and Ateshian, 1998, 2000). In addition to these mechanical alterations, cartilage undergoes compositional changes as OA advances, such as changes in its matrix constituents (decreases in proteoglycan

and disruptions in collagen architecture) and water content (Hatcher et al., 2017; Hollander et al., 1995; Rivers et al., 2000; Thompson and Oegema, 1979). Therefore, earlier detection of OA pathology may be accomplished through measurements of changes in composition and/or mechanical response (Knecht et al., 2006). Unfortunately, traditional assessment of cartilage composition and mechanical response is invasive (via histology, biochemistry, or mechanical testing, all of which require ex vivo tissue explants for analysis), limiting their clinical application to live patients.

On the other hand, MRI methods can provide noninvasive measures of in vivo cartilage composition and mechanical response to load, and may be beneficial towards earlier detection of OA pathology or OA risk (Guermazi et al., 2015; Knecht et al., 2006). For example, quantitative MRI techniques like T1rho mapping and T2 mapping are sensitive to water content, proteoglycan content, and collagen content and organization (Collins et al., 2018a; Guermazi et al., 2015; Hatcher et al., 2017; Li et al., 2007; Wayne et al., 2003). Furthermore, cartilage mechanical response to load can be quantified via a combination of MRI and physical activity (Chan et al., 2016; Coleman et al., 2013; Eckstein et al., 2005; Eckstein et al., 1999; Eckstein et al., 1998; Lad et al., 2016; Paranjape et al., 2019). Here, the physical activity imparts mechanical load to the tissue, while pre- and post-activity MRI quantifies its morphology (thickness or volume) and subsequent deformational response to the activity. In fact, recent work in our lab (Cutcliffe et al., In Prep; Paranjape et al., 2019) used this technique to not only measure strain after a

walking activity but also to measure the characteristic time of tibial plateau cartilage.

The characteristic time is a structural property of cartilage that is related to the tissue's stiffness, thickness, and permeability under linear biphasic models of cartilage mechanical function (Armstrong and Mow, 1982; Mow et al., 1980).

While these MRI techniques provide critical information, they still cannot directly measure cartilage stiffness. However, it is hypothesized that cartilage stiffness is significantly related to a combination of one or more of these MRI parameters, as the stiffness is one determinant of the mechanical response of the tissue (Mow et al., 1980) and changes with alterations in composition (Collins et al., 2018a). If so, stiffness estimates based on noninvasive MRI measures should be similar to ex vivo measurements of cartilage stiffness. Therefore, the purpose of this study was to create a statistical model relating cartilage stiffness (measured using traditional ex vivo techniques) to parameters that can be measured in vivo using MRI, to be used as a tool for assessing stiffness in vivo. The secondary goal of this study was to apply this model to an existing in vivo human MRI data set (Cutcliffe et al., In Prep).

6.2 Methods

6.2.1 Sample Harvest and MRI

Eight skeletally mature porcine lower limbs were procured with knee joints intact but musculature removed from a local abattoir directly after slaughter. Tissue was only received from deceased animals who were not euthanized for the purposes of this

study, so Institutional Animal Care and Use Committee (IACUC) approval was not required. Prior to dissection, each knee joint was MR imaged in the sagittal plane with the joint capsule intact using a 3 Tesla scanner (Trio Tim, Siemens, Erlangen, Germany) and an 8-channel knee coil (Invivo Corporation, Gainesville, FL). Three MR sequences were used: a double-echo steady-state (DESS) sequence (FOV: 16 cm x 16 cm; matrix: 512 px x 512 px; slice thickness: 1 mm; slice gap: 0 mm; flip angle: 25°; TR: 17 ms; TE: 6 ms), a T1rho map (FOV: 14 cm x 14 cm; matrix: 265 px x 256 px; slice thickness: 3 mm; slice gap: 0 mm; flip angle: 15°; TR: 3500 ms; TE: 5.9 ms; TSL: 5, 10, 40, and 80 ms at 500 Hz), and a T2 map (FOV: 16 cm x 16 cm; matrix: 384 px x 384 px; slice thickness: 3 mm; slice gap: 0.6 mm; flip angle: 180°; TR: 3500 ms; TE: 13.8, 27.6, 41.4, 55.2, 69.0, 82.8, and 96.6 ms). The total pre-dissection imaging lasted approximately 35 minutes per knee. Next, joints were dissected to expose the femoral and tibial articular surfaces, and 5 mm diameter cylindrical full-thickness cartilage explants (N = 76) were harvested from visually healthy regions, identified via a Collins grade of 0 (Collins and McElligott, 1960), of the tibial plateaus and femoral condyles. Explants were promptly wrapped in gauze soaked in phosphate-buffered saline (PBS) containing a protease inhibitor cocktail (Millipore Sigma, St. Louis, MO). Then, they were stored at -20°C until mechanical testing (see below). After dissection, each disarticulated bone (femur and tibia) was MR imaged again, using the same DESS protocol as used previously. Finally, each bone was stored at -20°C.

At a later date, two of the knee joints were thawed at room temperature for 24 hours and additional 5 mm diameter cartilage explants (N = 25) were harvested. In this second dissection, most explants (N = 18) were harvested from visually degenerated regions, identified via a Collins grade of I or II (Collins and McElligott, 1960), of the tibial plateaus and femoral condyles. The rest (N = 7) were harvested from visually healthy regions, to confirm that an additional freeze-thaw cycle did not alter the measured ex vivo mechanical properties (Athanasίου et al., 1994; Athanasίου et al., 1991).

6.2.2 MRI Data Analysis

The post-dissection DESS MR images were used to quantify the precise location of each explant, as the cartilage deficits resulting from harvest were visible within the DESS images. This was accomplished by creating three dimensional (3D) bone models from both the post-dissection DESS MR images and the pre-dissection T1rho and T2 images and registering them together. In this manner, the specific location of each explant was quantified in the T1rho and T2 images. Creation of the 3D bone models involved manual segmentation of the boundaries of the tibial and femoral cortices in each MRI slice (of the DESS, T1rho, and T2 images) using solid modeling software (Rhinoceros 4.0, Robert McNeel and Associates, Seattle, WA) (Figure 31). For the DESS images, the cartilage deficits were also manually segmented in every slice in which they appeared. Wireframe models of the bones (consisting of the segmentations compiled

across image slices) were used to create 3D surface mesh models via another solid modeling software (Geomagic Studio 11, 3D Systems, Rock Hill, SC). Then, the 3D surface mesh model of each bone (tibia and femur) from the post-dissection DESS scan was registered separately to the corresponding surface mesh model from the T1rho and T2 scans, respectively, using an iterative closest-point technique (Geomagic Studio 11, 3D Systems, Rock Hill, SC). The pixels in the T1rho and T2 images belonging within each explant were thus identified and used for further analysis.

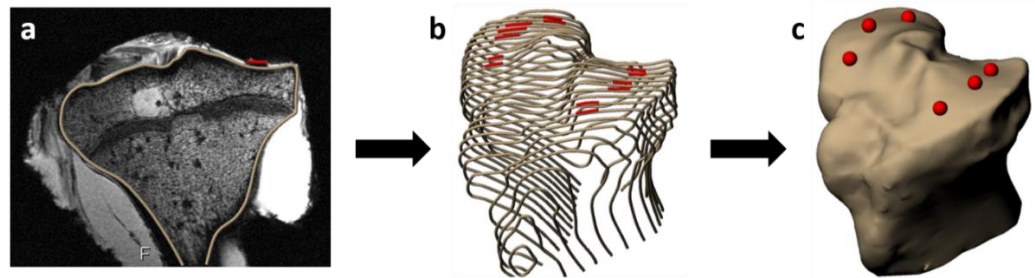


Figure 31: Bone and cartilage deficit measurement procedure. Image shows a) segmentation of tibial cortex and tibial articular cartilage deficit, b) compilation of segmentations across several slices, and c) 3D surface mesh model creation.

Additionally, the T1rho and T2 scans were used to quantify the mean T1rho and T2 relaxation times of each explant (Borthakur et al., 2003; Hatcher et al., 2017; Li et al., 2007). Relaxation times were calculated using custom software written in MATLAB (version R2018a, Mathworks, Natick MA) as follows: first, cartilage was manually segmented in each slice of the scan from the first acquired spin lock time (for T1rho scans) or echo time (for T2 scans). Then, these slice-specific segmentations were applied to the scans from subsequent spin lock or echo times to denote the set of pixels

comprising cartilage. For all pixels within the segmentation, the signal intensity was extracted from the scans of every spin lock or echo time and fit with an exponential function (Equation 59) to quantify the relaxation time of each pixel (Li et al., 2007). Each explant's relaxation time was calculated as the mean relaxation time across all pixels belonging within the explant, as identified from the post-dissection DESS MRI.

$$S = S_0 e^{-\left(\frac{t}{\tau_x}\right)} \quad (\text{Eq. 59})$$

where S = signal intensity, t = time (T1rho: spin lock; T2: echo),

and τ_x = fitted relaxation time constant (either T1rho or T2).

6.2.3 Mechanical Testing

Explants were thawed for 30 minutes at room temperature, after which 3 mm diameter cylindrical plugs were cut from the original 5 mm diameter explants. The 3 mm plugs were subsequently loaded into a confined compression fixture for mechanical testing (Figure 23), which was filled with PBS containing a protease inhibitor cocktail (Millipore Sigma, St. Louis, MO).

An MTS Acumen 3 materials test system (MTS Systems Corporation, Eden Prairie, MN) was used to carry out creep and recovery tests in load control, similar to our previous work (Cutcliffe and DeFrate, In Review). The test protocol began with cyclic preconditioning (-0.1 N to -0.3 N peak-to-peak sinusoid cycling at 0.10 Hz for 200 cycles) to allow the plugs to reach a repeatable, steady-state level of hydration. This number of loading cycles at this frequency forces fluid alternately out of and into the

tissue, until it reaches a dynamic equilibrium where no additional ratcheting strain accumulates per cycle (Gao et al., 2015). Then, explants equilibrated to a baseline thickness under a -0.1 N preload for 120 minutes (Athanasίου et al., 1991; Mow et al., 1989). Next, a creep load of -0.3 N was applied for 120 minutes so that plugs could reach creep equilibrium. This change in load (-0.2 N) was chosen to result in less than 20% strain at the end of creep (Ateshian et al., 1997; Mow et al., 1989; Mow et al., 1980). Finally, a recovery load of -0.1 N was applied for 120 minutes. The rate at which the preload, creep, and recovery loads were applied was 0.05 N/s.

6.2.4 Mechanical Testing Data Analysis

The deformation response of both creep and recovery was fit with the biphasic solution corresponding to confined compression creep (Equations 51-53) (Mow et al., 1980) to quantify the aggregate modulus and characteristic time (Armstrong and Mow, 1982) of the tissue during each phase (creep and recovery), as in our previous work (Cutcliffe and DeFrate, In Review). Nonlinear least-squares curve-fitting was implemented in MATLAB (version R2018a, Mathworks, Natick MA) to fit the theoretical solution to the experimental data. Baseline thickness was calculated as the average explant thickness over the last five minutes of the preload application (Cutcliffe and DeFrate, In Review).

6.2.5 Statistical Analysis

The primary goal of the current study was to model cartilage stiffness as a function of parameters that can be measured in vivo using MRI. As the creep response is classically used to quantify mechanical properties (Mansour, 2003; Mow and Huijskes, 2005), the aggregate modulus from the creep phase was used as the outcome variable in the statistical model (subsequently referred to as the “stiffness”). Continuous input variables used were the baseline thickness, characteristic recovery time, T1rho relaxation time, and T2 relaxation time. The only categorical input variable used was bone (either femur or tibia), representing from which bone each cartilage sample was harvested.

Statistical modeling was carried out using SAS (SAS 9.4, SAS Institute Inc., Cary, NC) with a significance level of $p < 0.05$. Because two dissections were performed, two data sets were analyzed in this study. In the first (termed, “healthy cartilage only data set”), explants from the first dissection ($N = 76$) were included; however, upon preparation for mechanical testing, $N = 2$ were found to exhibit degenerative surface fibrillations. These samples were still mechanically tested but were excluded from the healthy cartilage only data set (final $N = 74$). Two-tailed Pearson correlations were used to examine correlations between continuous input variables and the outcome. Further, multiple linear regression with mixed modeling was used to examine whether continuous input variables and/or the categorical input variable were significant predictors of the stiffness.

Based on the results of the healthy cartilage only data set, a second dissection was performed at a later date to obtain osteoarthritic explants (see 6.2.1 Sample Harvest and MRI). This was done to test whether the relationship between stiffness and input variables detected in the healthy cartilage only data set was also representative of degenerated cartilage. All explants from the two joints used in the second dissection were statistically analyzed in the second data set (termed, “healthy + degenerated cartilage data set”). This included those that were excluded from the healthy cartilage only data set (N = 2). In total, the healthy + degenerated cartilage data set encompassed N = 20 degenerated explants and N = 25 healthy explants (final N = 45). For this data set, the same analyses were carried out as for the healthy cartilage only data set (Pearson correlation and multiple linear regression with mixed modeling). Additionally, a two-way ANOVA was used to investigate effects of health status (visually healthy vs visually degenerated) and bone (femur vs tibia) on the continuous input variables and stiffness. Where significant main effects were found, the mean and standard deviation across either health status or bone were reported.

As the secondary goal of this study was to apply the developed models to an existing in vivo human MRI data set (Cutcliffe et al., In Prep), both models were applied separately to the existing in vivo human MRI data. First, the parsimonious model corresponding to each data set was developed, in which a second regression with mixed modeling was carried out using only the intercept and predictors that were found to be

statistically significant in the original multiple linear regression with mixed modeling analysis. Using the parameter estimates from the parsimonious models, stiffness values were computed for each volunteer using their respective in vivo MRI parameters. MRI parameters measured included baseline thickness, baseline mean T1rho relaxation time, baseline mean T2 relaxation time, and the characteristic recovery time of the tibial plateau cartilage. Next, permeability values were derived for each volunteer using their calculated stiffness, baseline thickness, and characteristic recovery times, via Equation 53b. In this manner, two stiffness and permeability values were computed for each volunteer, corresponding to the parsimonious model of the healthy cartilage only data set and that of the healthy + degenerated cartilage data set, respectively. MRI parameters, stiffness, and permeability values were reported as the mean \pm standard deviation.

6.3 Results

For the healthy cartilage only data set, both the characteristic recovery time and the baseline thickness were significantly correlated with the stiffness (Figure 32). The characteristic recovery time showed a negative correlation with stiffness and the baseline thickness showed a positive correlation with stiffness. On the other hand, neither the T1rho relaxation time nor the T2 relaxation time were significantly correlated with stiffness (Figure 32). Similarly, both the characteristic recovery time and the

baseline thickness were significant predictors of stiffness, while neither relaxation time (T1rho or T2) nor bone were significant predictors of stiffness (Table 6).

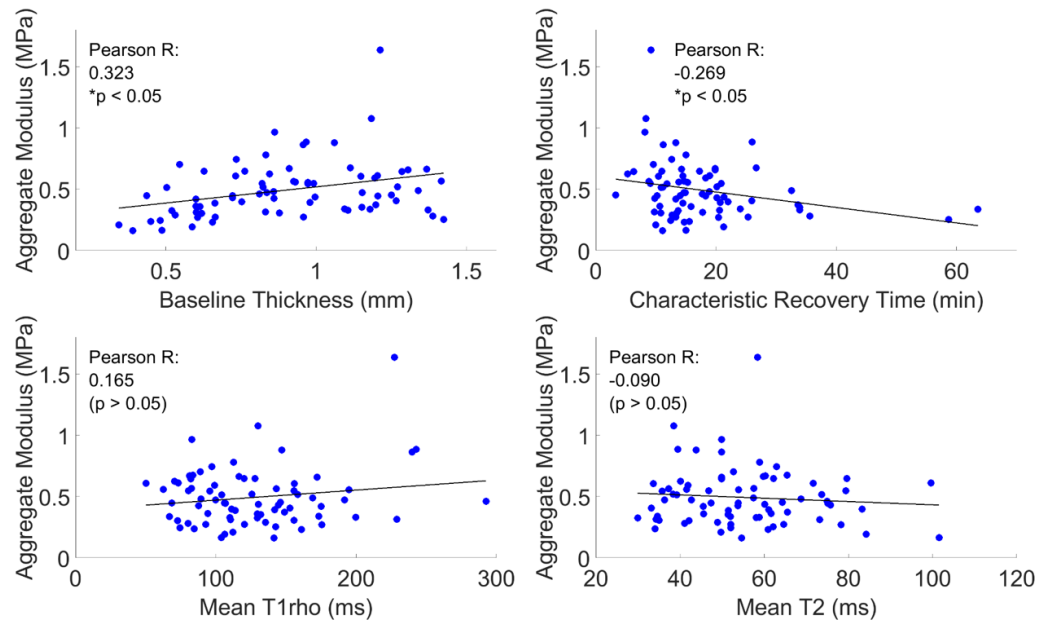


Figure 32: Correlations between input variables and stiffness (healthy cartilage only data set).

Table 6: Parameter Estimates of Stiffness Regression Model from Healthy Cartilage Only Data Set (bold = $p < 0.05$).

Variable	Full Model			Parsimonious Model		
	Parameter Estimate	Standard Error	p value	Parameter Estimate	Standard Error	p value
Intercept	0.1938	0.1263	0.169	0.2968	0.0767	0.006
Bone (Tibia = 0, Femur = 1)	-0.0545	0.0668	0.442	---	---	---
Baseline Thickness (mm)	0.4051	0.0937	<0.001	0.4451	0.0881	<0.001
Characteristic Recovery Time (min)	-0.0115	0.0026	<0.001	-0.0118	0.0025	<0.001
Mean T1rho Relaxation Time (ms)	0.0006	0.0005	0.220	---	---	---
Mean T2 Relaxation Time (ms)	0.0015	0.0015	0.341	---	---	---

In a similar manner, for the healthy + degenerated cartilage data set, the characteristic recovery time was significantly negatively correlated with stiffness while the T1rho and T2 relaxation times were not correlated with stiffness (Figure 33). However, the baseline thickness was no longer significantly correlated with stiffness in this data set (Figure 33). Along these same lines, only the characteristic recovery time was a significant predictor of stiffness, while neither relaxation time (T1rho nor T2), baseline thickness, nor bone were significant predictors of stiffness in this data set (Table 7). Moreover, there was a significant main effect of health status (visually healthy vs

visually degenerated) on all of the variables measured in this data set. Specifically, visually degenerated samples showed significantly lower stiffnesses (0.28 ± 0.18 MPa vs 0.43 ± 0.17 MPa), significantly larger baseline thicknesses (1.45 ± 0.27 mm vs 0.97 ± 0.31 mm), and significantly longer characteristic recovery times (63.0 ± 36.3 min vs 21.3 ± 9.9 min) than visually healthy samples, respectively. Further, visually degenerated samples showed significantly longer T1rho relaxation times (163 ± 66 ms vs 128 ± 38 ms) and significantly shorter T2 relaxation times (47 ± 12 ms vs 55 ± 13 ms) than visually healthy samples. Bone (femur vs tibia) showed a significant main effect on stiffness only, with tibial cartilage being stiffer than femoral cartilage (0.44 ± 0.18 MPa vs 0.29 ± 0.17 MPa).

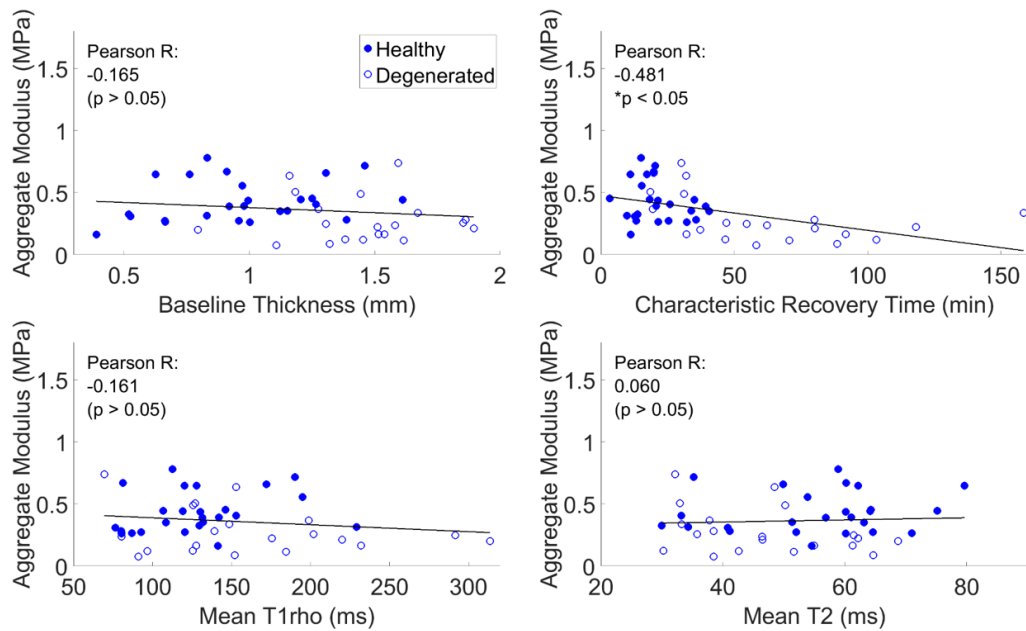


Figure 33: Correlations between input variables and stiffness (healthy and degenerated cartilage data set). Note different x-axes (but same y-axes) than Figure 32.

Table 7: Parameter Estimates of Stiffness Regression Model from Healthy and Degenerated Cartilage Data Set (bold = $p < 0.05$).

Variable	Full Model			Parsimonious Model		
	Parameter Estimate	Standard Error	p value	Parameter Estimate	Standard Error	p value
Intercept	0.3333	0.1517	0.272	0.4666	0.0562	0.076
Bone (Tibia = 0, Femur = 1)	-0.1521	0.0452	0.184	---	---	---
Baseline Thickness (mm)	0.1352	0.0795	0.097	---	---	---
Characteristic Recovery Time (min)	-0.0034	0.0009	<0.001	-0.0027	0.0007	<0.001
Mean T1rho Relaxation Time (ms)	-0.0003	0.0004	0.466	---	---	---
Mean T2 Relaxation Time (ms)	0.0023	0.0019	0.219	---	---	---

Across volunteers in the existing in vivo human MRI data set (Cutcliffe et al., In Prep), baseline thickness was 2.43 ± 0.28 mm, baseline mean T1rho relaxation time was 49 ± 5 ms, baseline mean T2 relaxation time was 46 ± 3 ms, and characteristic recovery time was 27.3 ± 20.0 min. Application of the healthy cartilage only data set model resulted in a stiffness of 1.06 ± 0.24 MPa and permeability of $5.65 \pm 9.33 \times 10^{-15}$ m⁴/Ns, while application of the healthy + degenerated cartilage data set model resulted in a stiffness of 0.39 ± 0.05 MPa and permeability of $16.43 \pm 28.34 \times 10^{-15}$ m⁴/Ns.

6.4 Discussion

As clinical OA diagnosis requires the presence of pain and radiographic features, which are usually not present until end-stage OA (Litwic et al., 2013; Lorenz and Richter, 2006), detection of earlier pathology using MRI methods may allow for enhanced diagnostic and therapeutic techniques. Of particular interest are mechanical properties, as these factors may be able to differentiate early OA cartilage from healthy cartilage (Knecht et al., 2006). Therefore, this study had two goals: 1) to develop an ex vivo model characterizing the relationship between stiffness (aggregate modulus) and parameters measurable via MRI, and 2) to apply this model to an existing in vivo data set consisting of these MRI-based parameters (Cutcliffe et al., In Prep) to estimate stiffness in vivo.

In the first goal, both healthy and degenerated cartilage were examined. OA cartilage exhibited significantly different mechanical properties—lower stiffness and increased characteristic recovery times—than healthy cartilage, which is consistent with prior reports using ex vivo mechanical testing techniques. For instance, a study modeling OA in the canine knee via 11 weeks of immobilization showed significantly lower stiffness and longer (albeit nonsignificantly) recovery times in the immobilized limbs compared to control limbs (Jurvelin et al., 1986). Additionally, another study conducted by our group also investigated healthy vs OA porcine cartilage (Hatcher et al., 2017). In that work, a significant decrease in stiffness and an overall increase in the

characteristic recovery time were observed in degenerated vs healthy cartilage. Likewise, previous work studying healthy and OA cartilage (Akizuki et al., 1986a) or using surgical ligament transection to model knee OA (Sah et al., 1997) found decreased stiffness, but no appreciable permeability changes, in OA cartilage compared to healthy cartilage (recall that permeability is related to the stiffness and characteristic time by Equation 53b). While a decrease in cartilage stiffness with OA is consistently seen in the literature (Armstrong and Mow, 1982; Bonassar et al., 1995; Grenier et al., 2014; Setton et al., 1994; Treppo et al., 2000; Wayne et al., 2003), there are conflicting reports of how permeability changes with OA. For example, other investigations using surgical ligament transection (Setton et al., 1994) or enzymatic digestion to model OA cartilage (Bonassar et al., 1995; Grenier et al., 2014; Wayne et al., 2003) observed increases in permeability either with time after surgery or with decreases in proteoglycan content. Similarly, prior studies of the variation in mechanical response with normal variation in composition also saw increases in permeability as proteoglycan content decreased (Treppo et al., 2000) or as water content increased (Armstrong and Mow, 1982). Finally, some studies even report a decrease in permeability in OA cartilage compared to healthy cartilage (Rivers et al., 2000). These discrepancies warrant further investigation—perhaps, similar to thickness and water content, which may initially increase in early OA but are decreased in advanced OA (Lorenz and Richter, 2006), the

permeability may change in different directions relative to healthy values between early and later stages of disease progression.

Furthermore, OA cartilage showed significantly different T1rho and T2 relaxation times compared to healthy cartilage, which is also consistent with earlier work. Specifically, OA cartilage had significantly increased T1rho relaxation times compared to healthy cartilage. Several studies, either in the ex vivo (Collins et al., 2018a; Hatcher et al., 2017; Li et al., 2011a) or in vivo environment (Li et al., 2007; Li et al., 2009; Nishioka et al., 2012), likewise found significant increases in T1rho relaxation time with OA. Conversely, OA cartilage had significantly decreased T2 relaxation times compared to healthy cartilage in the current study. While several studies found increased T2 relaxation times with OA (Collins et al., 2018a; Li et al., 2007; Li et al., 2009; Nishioka et al., 2012), prior work by our group similarly found decreased T2 relaxation times in OA cartilage (Hatcher et al., 2017). In that study, histological analysis showed that OA cartilage lacked the superficial layer, which demonstrates significantly higher T2 relaxation times than does the deep layer (Carballido-Gamio et al., 2010; Hannila et al., 2009; Nieminen et al., 2001). As a result, the authors concluded that the lower T2 times observed in OA cartilage were a result of the missing superficial layer. Similarly, a study using interleukin-1 to induce cartilage degradation found lower T2 values in treated cartilage compared with untreated control tissue (Menezes et al., 2004). Moreover, another study found that the T2 relaxation time of moderate OA cartilage was

significantly larger than that of severe OA cartilage (David-Vaudey et al., 2004). Perhaps changes in collagen organization or arrangement dominate the T2 relaxation time at early stages of OA while subsequent changes in collagen content (such as a lack of the superficial zone) dominate at later stages of the disease (Hatcher et al., 2017).

Additionally, T2 is sensitive not only to collagen organization within the tissue but also to water content (Guermazi et al., 2015; Li et al., 2007; Matzat et al., 2013; Nishioka et al., 2012). As water content may be elevated in mild stages of the disease (but is ultimately decreased in late stages of OA) (Lorenz and Richter, 2006), the T2 relaxation time's dependence on water content may also influence measures of T2 relaxation in cartilage displaying different degrees of OA pathology. Taken together, these observations underscore the complexity of the T2 relaxation time's relationship with water content and collagen organization.

In the second goal, we applied our statistical models (developed in fulfillment of the first goal) to an in vivo data set (Cutcliffe et al., In Prep). Both models resulted in estimates of human cartilage stiffness and permeability on the same order of magnitude as found in the literature using traditional ex vivo mechanical testing (Akizuki et al., 1986a; Armstrong and Mow, 1982; Athanasiou et al., 1994; Athanasiou et al., 1995b; Athanasiou et al., 1991; Treppo et al., 2000) (Table 8). Included where possible are the corresponding characteristic times (Armstrong and Mow, 1982), which were calculated using the reported mean values of baseline thickness, stiffness, and permeability.

Importantly, the in vivo characteristic recovery time measured by our group of tibial plateau cartilage (27.30 ± 20.0 min) is similar to that quantified in the ex vivo environment with mechanical testing (26.8 min) (Table 8). Likewise, the in vivo baseline thickness (2.43 ± 0.28 mm) is similar to reported ex vivo measures of human tibial plateau sample height (2.27 ± 0.50 mm) (Table 8). While our in vivo stiffness estimate from the healthy cartilage only data set model is somewhat larger than reported ex vivo tibial plateau stiffness values (1.06 ± 0.24 compared to 0.65 ± 0.25 and 0.45 ± 0.28 MPa), it is still within the ranges reported for other regions of human cartilage (such as the distal tibia, proximal talus, femoral condyles, or femoral head cartilage) (Table 8). Further, our estimate from the healthy + degenerated cartilage data set model is much closer to reported ex vivo tibial plateau stiffness values (0.39 ± 0.05 compared to 0.65 ± 0.25 and 0.45 ± 0.28 MPa) (Table 8). Correspondingly, our in vivo permeability estimate from the healthy cartilage only data set model is similar to ex vivo measures of permeability (5.65 ± 9.33 compared to 2.00 and $9.18 \pm 9.77 \times 10^{-15}$ m⁴/Ns) while the other estimate from the healthy + degenerated cartilage data set model is larger than ex vivo measures ($16.43 \pm 28.34 \times 10^{-15}$ m⁴/Ns) (Table 8).

Table 8: Human Cartilage Mechanical Properties (mean \pm standard deviation).

Reference	Cartilage Location	Sample Height (h, mm)	Stiffness (H_A , MPa)	Permeability (k , $\times 10^{-15}$ m ⁴ /Ns)	Characteristic Time (τ_0 , min)
Current Study	Tibial Plateau (healthy only model)	2.43 ± 0.28	1.06 ± 0.24	5.65 ± 9.33	27.3 ± 20.0
	Tibial Plateau (healthy + degen. model)	2.43 ± 0.28	0.39 ± 0.05	16.43 ± 28.34	27.3 ± 20.0
Akizuki et al. 1986	Tibial Plateau	2.27 ± 0.50	0.65 ± 0.25	2.00 \pm n/a	26.8
Treppo et al. 2000	Tibial Plateau	---	0.45 ± 0.28	9.18 ± 8.77	---
	Distal Femur	---	0.60 ± 0.35	5.17 ± 6.24	---
	Proximal Talus	---	0.93 ± 0.45	2.55 ± 2.83	---
Athanasίου et al. 1995	Proximal Talus	1.22 ± 0.30	1.06 ± 0.39	1.09 ± 0.87	8.7
	Distal Tibia	1.14 ± 0.23	1.19 ± 0.39	1.43 ± 1.84	5.2
Armstrong & Mow 1982	Patella	3.12 ± 0.72	0.79 ± 0.36	4.70 ± 3.60	17.7
Athanasίου et al. 1991	Patello-femoral Groove	3.57 ± 1.12	0.53 ± 0.09	2.17 ± 0.73	74.8
	Lateral Femoral Condyle	2.31 ± 0.53	0.70 ± 0.23	1.18 ± 0.21	43.5
	Medial Femoral Condyle	2.21 ± 0.59	0.59 ± 0.11	1.14 ± 0.16	49.4
Athanasίου et al. 1994	Femoral Head	1.40 ± 0.21	1.19 ± 0.51	0.92 ± 0.47	12.1
	Acetabulum	1.26 ± 0.27	1.24 ± 0.58	0.87 ± 0.58	10.0

The differences in stiffness and permeability estimates between the two models are due to the fact that the model from the healthy cartilage only data set included the baseline thickness and the characteristic recovery time, while the model from the healthy + degenerated cartilage data set included only the characteristic recovery time (Table 6 and Table 7). This is likely because differences in thickness between the femur and tibia were observed in the healthy cartilage only data set (two-sample t-test, $p < 0.05$), with tibial cartilage being significantly thicker than femoral cartilage (0.96 ± 0.29 mm vs 0.80 ± 0.26 mm). On the other hand, no height differences across bone were observed in the healthy + degenerated cartilage data set, but OA cartilage was significantly thicker than healthy cartilage. As a greater proportion of femoral samples showed OA than tibial samples, the relative increase in thickness due to OA may have confounded differences in baseline thickness across bone in this data set.

Importantly, both of the statistical models illustrate that the characteristic recovery time is a stronger moderator of stiffness in these data sets than either the T1rho or T2 relaxation times. Comparison of values from both data sets (Figure 34) illustrates this, indicating that early changes in cartilage health may be more easily identified by measuring in vivo mechanical properties (such as the characteristic recovery time) than other baseline imaging markers. To this point, in the healthy + degenerated cartilage data set, the effect size (Cohen's D) (Cohen, 1962) of the characteristic recovery time was 1.65, indicating a large effect (> 0.8), while for the T1rho and T2 relaxation times it was

0.66 and 0.64 (indicating moderate effects, > 0.2 but < 0.8), respectively. In further support of this hypothesis, a recent study modeling OA in mice through surgical destabilization of the medial meniscus (Doyran et al., 2017) found that significant decreases in stiffness were evident within a week after surgery, while histological markers of OA (e.g. cartilage thinning and/or fibrillation, changes in proteoglycan staining) were not apparent until 4 weeks after surgery at the earliest. This is not to say that histology or quantitative MRI measures such as T1rho and T2 relaxation times are not useful; on the contrary, they provide important information about cartilage composition and health, especially when OA pathology is advanced. However, mechanical metrics (e.g. characteristic time, stiffness) may be more sensitive to early changes in cartilage health than quantitative MRI measures. For example, a recent review (Atkinson et al., 2019) indicated that T1rho and T2 relaxation times have effect sizes generally in the moderate range (0.35-0.40 and 0.33-0.74, respectively) in subjects without but at risk of OA compared to controls. On the other hand, effect sizes (calculated using the reported means and standard deviations) for baseline T1rho and T2 measurements in studies of patients with definite OA compared to controls (Li et al., 2007; Souza et al., 2010; Teng et al., 2016) range from 0.45 to 2.76, with a majority of effect sizes being greater than 1 (indicating large effects). However, few studies beyond the current investigation have measured changes in quantitative MRI metrics simultaneously with mechanical changes in models of OA. In those that have (Collins et

al., 2018a; Hatcher et al., 2017; Wayne et al., 2003), changes in mechanical properties were observed concomitant with changes in T1rho or T2 relaxation times, as in the present study. Yet, it remained unclear whether quantitative imaging may be used as an indicator of the mechanical state of the tissue. Towards this end, the current study demonstrates that while quantitative imaging metrics are important in differentiating healthy and OA cartilage, they are not as strong of moderators of stiffness as is the characteristic recovery time. Therefore, the characteristic recovery time may represent another useful indicator of mechanical function and that is sensitive to early changes in cartilage health.

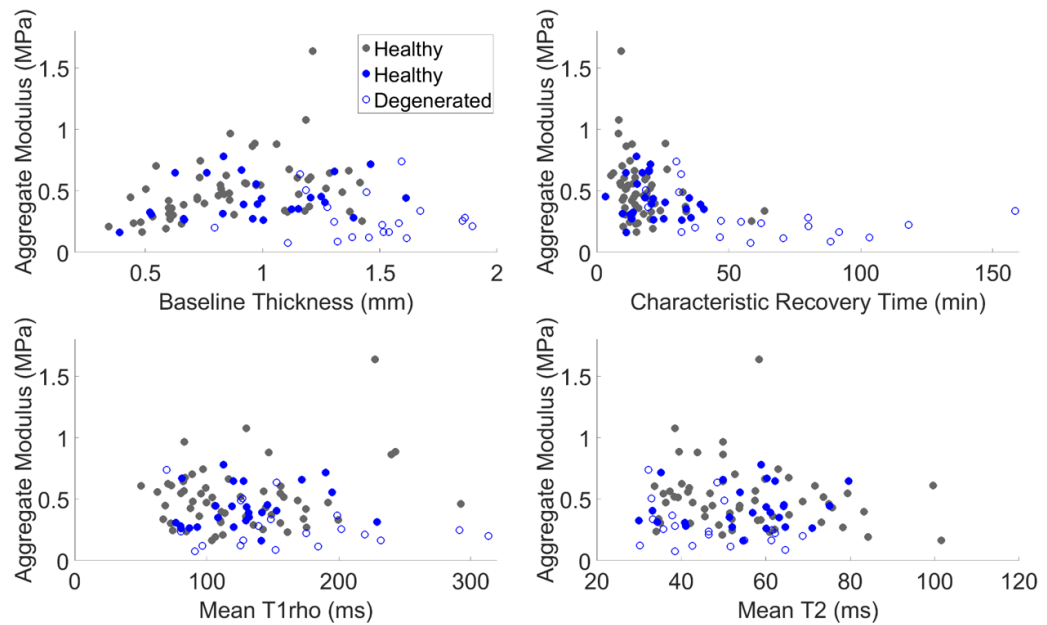


Figure 34: Comparison of values from both data sets (healthy cartilage only, and healthy and degenerated cartilage data sets). The healthy cartilage only data set comprised all filled circles (grey and blue) while the healthy and degenerated cartilage data set comprised all blue circles (filled and open). Note different x-axes (but same y-axes) than Figure 32 and Figure 33.

A potential limitation of this study is that the statistical models were developed using porcine cartilage but were applied to human cartilage, as cartilage tissue from different species has been observed to exhibit different mechanical properties (Athanasίου et al., 1995a). Importantly, the design of this study does not assume that porcine cartilage properties are representative of human cartilage properties; rather, it assumes that the relationship between cartilage imaging metrics and mechanical properties is the same across species. This assumption is supported by the similarity in literature values of human tibial cartilage stiffness and the in vivo estimates developed in the current study. While differences in these relationships may exist, animal models

of disease are commonly used as a crucial first step toward understanding human disease. Thus, despite potential differences in these relationships across species, the methodology of this study represents a novel approach for quantifying stiffness in vivo.

6.5 Conclusion

Overall, the results of this study illustrate that the characteristic recovery time—a property that can be noninvasively quantified in vivo—is predictive of cartilage stiffness, one of the mechanical properties known to change with OA (Hatcher et al., 2017; Knecht et al., 2006; Rivers et al., 2000). Therefore, it may serve as an indicator of cartilage health. Further, because the characteristic recovery time is a single property incorporating multiple aspects of mechanical function (thickness, stiffness, and permeability), all of which may change in mild or pre-OA (Knecht et al., 2006), it may provide valuable early indication of OA pathology, especially when quantified in addition to noninvasive compositional measures such as T1rho and T2 relaxation time. Future studies detailing how this metric changes during disease progression (mild, moderate, and severe) are therefore warranted to assess its efficacy as a clinical marker of OA.

6.6 Acknowledgements

The authors would like to thank the Center for Advanced Magnetic Resonance Development at Duke University for their assistance with this project, and would like to

gratefully acknowledge Lia Meirose for her helpful discussions concerning this study.

This study was supported by the NIH grants AR065527, AR074800, and AR075399.

7. Conclusion

The principal goal of this dissertation was to measure cartilage mechanical properties *in vivo*. The development of a noninvasive imaging technique accomplishing this goal consisted of two parts, each corresponding to a particular Specific Aim. The focus of Aim 1 was the creation of a statistical model relating cartilage stiffness to metrics measurable *in vivo* using MRI, while the purpose of Aim 2 was the application of this model to healthy normative human data and comparison of the resulting *in vivo* stiffness estimates with literature values of *ex vivo* human cartilage stiffness.

As mechanical properties such as stiffness and permeability change with OA progression (Knecht et al., 2006; Mansour, 2003; Mow and Huiskes, 2005), *in vivo* measurement of these properties may aid in the diagnosis of OA. This is crucial as current clinical OA detection relies on the presence of pain and gross radiographic findings, which are not generally present until advanced stages of the disease when therapeutic approaches are limited (Glyn-Jones et al., 2015; Litwic et al., 2013; Lorenz and Richter, 2006). Because compositional and biomechanical changes precede large changes in morphology visible on radiography (Knecht et al., 2006; Loeser et al., 2012; Lorenz and Richter, 2006), *in vivo* measurement of changes in mechanical properties may enable earlier detection of OA pathology than current clinical practice, allowing for the development of improved treatment and management techniques.

7.1 Major Contributions

In total, the work comprising this dissertation represents a significant contribution to the scientific literature in that it presents and validates a novel technique for quantifying cartilage mechanical properties noninvasively in vivo (Section 6. In vivo Estimation of Cartilage Stiffness using Noninvasive Imaging Metrics). Prior to this study, measurement of mechanical properties was available only in the ex vivo environment (Guo et al., 2003; Mow and Guo, 2002; Mow and Huijskes, 2005). However, the research presented in this dissertation offers other important contributions beyond the technique for in vivo measurement of cartilage mechanical properties.

For example, Section 4. Comparison of Cartilage Mechanical Properties Measured During Creep and Recovery (Cutcliffe and DeFrate, In Review) demonstrates that similar mechanical properties are quantified when fitting either the creep response or recovery response with the linear biphasic solution for confined compression (Mow et al., 1980). This result validates measurements of the recovery phase in vivo, as measuring recovery is more accessible in vivo with the cartilage stress test (fewer visits per volunteer, less time and expense spent on MRI) than measuring creep. Though not the focus of the study, this work also presents a preconditioning protocol for cartilage in confined compression (cyclic loading in addition to a static preload). While several studies quantifying cartilage mechanical properties begin with a static preload (Akizuki et al., 1986a; Ateshian et al., 1997; Grenier et al., 2014; Setton et al., 1993; Soltz and

Ateshian, 1998), few discuss other elements of preconditioning. In many loading regimes (such as tension), preconditioning is commonly used to ensure repeatability of the measured response by applying a consistent loading history before mechanical testing. As prior literature illustrates that cartilage approaches a dynamic equilibrium in response to cyclic loading (Gao et al., 2015), the current work similarly used cyclic loading to dynamic equilibrium as part of the preconditioning. This is because the steady-state tissue hydration occurring at dynamic equilibrium provides a repeatable point of reference, which is the general purpose of preconditioning. In the current research, recovery to a baseline thickness under a static preload after cyclic loading was used to define the reference state of the cartilage. In future *ex vivo* investigations of cartilage mechanical properties, it is recommended that similar preconditioning profiles are used to standardize the loading history experienced by cartilage specimens and improve study repeatability.

Additionally, Section 3. A New Stress Test for Knee Joint Cartilage (Paranjape et al., 2019) and Section 5. In Vivo Cartilage Strain and Recovery After 30 Minutes of Walking (Cutcliffe et al., In Prep) quantify the *in vivo* strain response of healthy cartilage to various bouts of walking and recovery after walking, respectively, which supports the development of exercise-based interventions for OA. As specific doses of loading may promote cartilage health (Sun, 2010), walking exercise is a common clinical recommendation for OA patients (Focht, 2006). Towards this end, the normative data

from these studies describing the response of healthy cartilage to 30 minutes of walking helps inform clinical targets for use in exercise-based OA therapies.

7.2. Future Work

Overall, the noninvasive imaging technique developed here for the in vivo assessment of cartilage mechanical properties is useful for future studies investigating cartilage mechanical response and its relationship to cartilage health. This methodology has diverse applications and can assess in vivo joint biomechanics across a range of populations (healthy, OA, acutely injured, chronically injured, aging, obese) in a patient-specific manner. Detailed studies of these populations and characterization of changes in their cartilage mechanical properties over time would improve the understanding of OA etiology in general, as well as how different risk factors contribute to the onset and progression of the disease. Furthermore, this technique may help define a pre-OA cartilage state or may be used clinically to earlier detect OA pathology. As such, this technique can be applied in future work to identify additional populations at risk of OA or to assess the efficacy of treatment strategies in preventing or reversing OA degeneration.

Appendix A

Equivalency of Equations 11 and 12 is based on equivalency of the first term in each equation.

$$-\varphi^f \operatorname{div}(pI) - K(\vec{v}^f - \vec{v}^s) = 0 \quad (\text{Eq. 11})$$

$$-\varphi^f \operatorname{grad}(p) - K(\vec{v}^f - \vec{v}^s) = 0 \quad (\text{Eq. 12})$$

As both expressions include $-K(\vec{v}^f - \vec{v}^s)$ on the left-hand side and both equal zero on the right-hand side, the two expressions are equivalent if the first terms of each expression are equivalent. Because the first term in each expression includes multiplication by $-\varphi^f$, equivalency is demonstrated if Equations A1 and A2 are equal:

$$\operatorname{div}(pI) \quad \text{from Equation 11} \quad (\text{Eq. A1})$$

$$\operatorname{grad}(p) \quad \text{from Equation 12} \quad (\text{Eq. A2})$$

As p represents the magnitude of the hydrostatic pressure, $\operatorname{grad}(p)$ (from Equation A2) represents a vector:

$$\operatorname{grad}(p) = \frac{\partial p}{\partial x} \hat{x} + \frac{\partial p}{\partial y} \hat{y} + \frac{\partial p}{\partial z} \hat{z} \quad (\text{Eq. A3})$$

where $\hat{x}, \hat{y}, \hat{z} =$ unit vectors representing the three orthogonal directions of a Cartesian coordinate system

Likewise, as I represents the identity matrix, pI (from Equation A1) represents a matrix, denoted B :

$$pI = \begin{bmatrix} p & 0 & 0 \\ 0 & p & 0 \\ 0 & 0 & p \end{bmatrix} = B \quad (\text{Eq. A4})$$

Therefore, $div(pI)$ represents a vector:

$$\begin{aligned}
 div(pI) &= div(B) = \\
 &\left(\frac{\partial B_{xx}}{\partial x} + \frac{\partial B_{xy}}{\partial y} + \frac{\partial B_{xz}}{\partial z}\right) \hat{x} + \dots \\
 &\left(\frac{\partial B_{yx}}{\partial x} + \frac{\partial B_{yy}}{\partial y} + \frac{\partial B_{yz}}{\partial z}\right) \hat{y} + \dots \\
 &\left(\frac{\partial B_{zx}}{\partial x} + \frac{\partial B_{zy}}{\partial y} + \frac{\partial B_{zz}}{\partial z}\right) \hat{z}
 \end{aligned} \tag{Eq. A5}$$

As the non-diagonal elements of B equal zero (from Equation A4), Equation A5 simplifies to:

$$div(pI) = div(B) = \frac{\partial B_{xx}}{\partial x} \hat{x} + \frac{\partial B_{yy}}{\partial y} \hat{y} + \frac{\partial B_{zz}}{\partial z} \hat{z} \tag{Eq. A6}$$

Substituting Equation A4 into A6 results in:

$$div(pI) = \frac{\partial p}{\partial x} \hat{x} + \frac{\partial p}{\partial y} \hat{y} + \frac{\partial p}{\partial z} \hat{z} \tag{Eq. A7}$$

Comparison of Equations A3 and A7 illustrates their equivalency.

Appendix B

Equivalency of Equations 14 and 15 is based on equivalency of each of the terms in the equations.

$$\text{div}(-\phi^s p I) + \text{div}(\lambda_s \text{tr}(\tilde{\varepsilon}) I + 2\mu_s \tilde{\varepsilon}) + K(\vec{v}^f - \vec{v}^s) = 0 \quad (\text{Eq. 14})$$

$$-\phi^s \text{grad}(p) + (\lambda_s + \mu_s) \text{grad}(\text{div}(\vec{u})) + \dots$$

$$\mu_s \nabla^2 \vec{u} + K(\vec{v}^f - \vec{v}^s) = 0 \quad (\text{Eq. 15})$$

Comparison of the last terms, Equations B1 and B2, demonstrates their equivalency:

$$K(\vec{v}^f - \vec{v}^s) = 0 \quad \text{from Equation 14} \quad (\text{Eq. B1})$$

$$K(\vec{v}^f - \vec{v}^s) = 0 \quad \text{from Equation 15} \quad (\text{Eq. B2})$$

Equivalency of the first terms, Equations B3 and B4, may be shown with some rearrangement of Equation B3:

$$\text{div}(-\phi^s p I) \quad \text{from Equation 14} \quad (\text{Eq. B3})$$

$$-\phi^s \text{grad}(p) \quad \text{from Equation 15} \quad (\text{Eq. B4})$$

Since $-\phi^s$ is a scalar, it may be pulled out of the divergence operation:

$$\text{div}(-\phi^s p I) = -\phi^s \text{div}(p I) \quad (\text{Eq. B5})$$

Comparison of Equations B4 and B5 shows their equivalency, for an analogous demonstration as that given in Appendix A.

This leaves comparison of the middle terms, Equations B6 and B7:

$$\operatorname{div}(\lambda_s \operatorname{tr}(\tilde{\varepsilon})I + 2\mu_s \tilde{\varepsilon}) \quad \text{from Equation 14} \quad (\text{Eq. B6})$$

$$(\lambda_s + \mu_s) \operatorname{grad}(\operatorname{div}(\bar{u})) + \mu_s \nabla^2 \bar{u} \quad \text{from Equation 15} \quad (\text{Eq. B7})$$

Starting with Equation B6: this equation represents the divergence of the elastic stress tensor of the solid phase, denoted $\tilde{\sigma}^e$ (Equation 5):

$$\operatorname{div}(\lambda_s \operatorname{tr}(\tilde{\varepsilon})I + 2\mu_s \tilde{\varepsilon}) = \operatorname{div}(\tilde{\sigma}^e) \quad (\text{Eq. B8})$$

Therefore, $\operatorname{div}(\tilde{\sigma}^e)$ represents a vector, where $\tilde{\sigma}^e$ is denoted as R for visual simplification:

$$\begin{aligned} \operatorname{div}(\tilde{\sigma}^e) = \operatorname{div}(R) = & \\ & \left(\frac{\partial R_{xx}}{\partial x} + \frac{\partial R_{xy}}{\partial y} + \frac{\partial R_{xz}}{\partial z} \right) \hat{x} + \dots \\ & \left(\frac{\partial R_{yx}}{\partial x} + \frac{\partial R_{yy}}{\partial y} + \frac{\partial R_{yz}}{\partial z} \right) \hat{y} + \dots \\ & \left(\frac{\partial R_{zx}}{\partial x} + \frac{\partial R_{zy}}{\partial y} + \frac{\partial R_{zz}}{\partial z} \right) \hat{z} \end{aligned} \quad (\text{Eq. B9})$$

The nine components of $\tilde{\sigma}^e$ (or, equivalently, R) are given as follows, from Equation 5:

$$\begin{aligned} R_{xx} &= (\lambda_s + 2\mu_s)\varepsilon_{xx} + \lambda_s(\varepsilon_{yy} + \varepsilon_{zz}) \\ R_{xy} &= R_{yx} = 2\mu_s\varepsilon_{xy} = 2\mu_s\varepsilon_{yx} \\ R_{xz} &= R_{zx} = 2\mu_s\varepsilon_{xz} = 2\mu_s\varepsilon_{zx} \\ R_{yy} &= (\lambda_s + 2\mu_s)\varepsilon_{yy} + \lambda_s(\varepsilon_{xx} + \varepsilon_{zz}) \\ R_{yz} &= R_{zy} = 2\mu_s\varepsilon_{yz} = 2\mu_s\varepsilon_{zy} \\ R_{zz} &= (\lambda_s + 2\mu_s)\varepsilon_{zz} + \lambda_s(\varepsilon_{xx} + \varepsilon_{yy}) \end{aligned} \quad (\text{Eq. B10})$$

Substitution of Equation B10 into Equation B9 yields:

$$\begin{aligned}
& \left(\frac{\partial[(\lambda_s+2\mu_s)\varepsilon_{xx}+\lambda_s(\varepsilon_{yy}+\varepsilon_{zz})]}{\partial x} + \frac{\partial 2\mu_s\varepsilon_{xy}}{\partial y} + \frac{\partial 2\mu_s\varepsilon_{xz}}{\partial z} \right) \hat{x} + \dots \\
& \left(\frac{\partial 2\mu_s\varepsilon_{xy}}{\partial x} + \frac{\partial[(\lambda_s+2\mu_s)\varepsilon_{yy}+\lambda_s(\varepsilon_{xx}+\varepsilon_{zz})]}{\partial y} + \frac{\partial 2\mu_s\varepsilon_{yz}}{\partial z} \right) \hat{y} + \dots \\
& \left(\frac{\partial 2\mu_s\varepsilon_{xz}}{\partial x} + \frac{\partial 2\mu_s\varepsilon_{yz}}{\partial y} + \frac{\partial[(\lambda_s+2\mu_s)\varepsilon_{zz}+\lambda_s(\varepsilon_{xx}+\varepsilon_{yy})]}{\partial z} \right) \hat{z} \tag{Eq. B11}
\end{aligned}$$

Next, $\vec{\varepsilon}$ represents the infinitesimal strain tensor, which is a function of \vec{u} , the solid matrix displacement vector. The nine components of $\vec{\varepsilon}$ are given as follows:

$$\begin{aligned}
\varepsilon_{xx} &= \frac{\partial u_x}{\partial x} \\
\varepsilon_{xy} &= \varepsilon_{yx} = \frac{1}{2} \frac{\partial u_x}{\partial y} + \frac{1}{2} \frac{\partial u_y}{\partial x} \\
\varepsilon_{xz} &= \varepsilon_{zx} = \frac{1}{2} \frac{\partial u_x}{\partial z} + \frac{1}{2} \frac{\partial u_z}{\partial x} \\
\varepsilon_{yy} &= \frac{\partial u_y}{\partial y} \\
\varepsilon_{yz} &= \varepsilon_{zy} = \frac{1}{2} \frac{\partial u_y}{\partial z} + \frac{1}{2} \frac{\partial u_z}{\partial y} \\
\varepsilon_{zz} &= \frac{\partial u_z}{\partial z}
\end{aligned} \tag{Eq. B12}$$

Substituting Equation B12 into each component (the \hat{x} , \hat{y} , and \hat{z} components, respectively) of Equation B11 results in the below:

For \hat{x} :

$$\begin{aligned}
& \frac{\partial}{\partial x} \left(\lambda_s \frac{\partial u_x}{\partial x} + 2\mu_s \frac{\partial u_x}{\partial x} + \lambda_s \frac{\partial u_y}{\partial y} + \lambda_s \frac{\partial u_z}{\partial z} \right) + \dots \\
& \frac{\partial}{\partial y} \left(2\mu_s \left(\frac{1}{2} \frac{\partial u_x}{\partial y} + \frac{1}{2} \frac{\partial u_y}{\partial x} \right) \right) + \frac{\partial}{\partial z} \left(2\mu_s \left(\frac{1}{2} \frac{\partial u_x}{\partial z} + \frac{1}{2} \frac{\partial u_z}{\partial x} \right) \right)
\end{aligned}$$

which equals:

$$\begin{aligned} \lambda_s \frac{\partial}{\partial x} \frac{\partial u_x}{\partial x} + 2\mu_s \frac{\partial}{\partial x} \frac{\partial u_x}{\partial x} + \lambda_s \frac{\partial}{\partial x} \frac{\partial u_y}{\partial y} + \lambda_s \frac{\partial}{\partial x} \frac{\partial u_z}{\partial z} + \dots \\ \mu_s \frac{\partial}{\partial y} \frac{\partial u_x}{\partial y} + \mu_s \frac{\partial}{\partial y} \frac{\partial u_y}{\partial x} + \mu_s \frac{\partial}{\partial z} \frac{\partial u_x}{\partial z} + \mu_s \frac{\partial}{\partial z} \frac{\partial u_z}{\partial x} \end{aligned} \quad (\text{Eq. B13a})$$

For \hat{y} :

$$\begin{aligned} \frac{\partial}{\partial x} \left(2\mu_s \left(\frac{1}{2} \frac{\partial u_x}{\partial y} + \frac{1}{2} \frac{\partial u_y}{\partial x} \right) \right) + \dots \\ \frac{\partial}{\partial y} \left(\lambda_s \frac{\partial u_y}{\partial y} + 2\mu_s \frac{\partial u_y}{\partial y} + \lambda_s \frac{\partial u_x}{\partial x} + \lambda_s \frac{\partial u_z}{\partial z} \right) + \frac{\partial}{\partial z} \left(2\mu_s \left(\frac{1}{2} \frac{\partial u_y}{\partial z} + \frac{1}{2} \frac{\partial u_z}{\partial y} \right) \right) \end{aligned}$$

which equals:

$$\begin{aligned} \mu_s \frac{\partial}{\partial x} \frac{\partial u_x}{\partial y} + \mu_s \frac{\partial}{\partial x} \frac{\partial u_y}{\partial x} + \lambda_s \frac{\partial}{\partial y} \frac{\partial u_y}{\partial y} + 2\mu_s \frac{\partial}{\partial y} \frac{\partial u_y}{\partial y} + \dots \\ \lambda_s \frac{\partial}{\partial y} \frac{\partial u_x}{\partial x} + \lambda_s \frac{\partial}{\partial y} \frac{\partial u_z}{\partial z} + \mu_s \frac{\partial}{\partial z} \frac{\partial u_y}{\partial z} + \mu_s \frac{\partial}{\partial z} \frac{\partial u_z}{\partial y} \end{aligned} \quad (\text{Eq. B13b})$$

For \hat{z} :

$$\begin{aligned} \frac{\partial}{\partial x} \left(2\mu_s \left(\frac{1}{2} \frac{\partial u_x}{\partial z} + \frac{1}{2} \frac{\partial u_z}{\partial x} \right) \right) + \frac{\partial}{\partial y} \left(2\mu_s \left(\frac{1}{2} \frac{\partial u_y}{\partial z} + \frac{1}{2} \frac{\partial u_z}{\partial y} \right) \right) + \dots \\ \frac{\partial}{\partial z} \left(\lambda_s \frac{\partial u_z}{\partial z} + 2\mu_s \frac{\partial u_z}{\partial z} + \lambda_s \frac{\partial u_x}{\partial x} + \lambda_s \frac{\partial u_y}{\partial y} \right) \end{aligned}$$

which equals:

$$\begin{aligned} \mu_s \frac{\partial}{\partial x} \frac{\partial u_x}{\partial z} + \mu_s \frac{\partial}{\partial x} \frac{\partial u_z}{\partial x} + \mu_s \frac{\partial}{\partial y} \frac{\partial u_y}{\partial z} + \mu_s \frac{\partial}{\partial y} \frac{\partial u_z}{\partial y} + \dots \\ \lambda_s \frac{\partial}{\partial z} \frac{\partial u_z}{\partial z} + 2\mu_s \frac{\partial}{\partial z} \frac{\partial u_z}{\partial z} + \lambda_s \frac{\partial}{\partial z} \frac{\partial u_x}{\partial x} + \lambda_s \frac{\partial}{\partial z} \frac{\partial u_y}{\partial y} \end{aligned} \quad (\text{Eq. B13c})$$

Moving on to Equation B7: expansion of this equation involves both the divergence of \vec{u} and the gradient of the divergence of \vec{u} . The quantity \vec{u} is a vector, and can be written as:

$$\vec{u} = u_x \hat{x} + u_y \hat{y} + u_z \hat{z} \quad (\text{Eq. B14})$$

As such, $div(\vec{u})$ represents a scalar, while $grad(div(\vec{u}))$ represents a vector:

$$div(\vec{u}) = \frac{\partial}{\partial x} u_x + \frac{\partial}{\partial y} u_y + \frac{\partial}{\partial z} u_z \quad (\text{Eq. B15})$$

$$grad(div(\vec{u})) = \frac{\partial}{\partial x} [div(\vec{u})] \hat{x} + \frac{\partial}{\partial y} [div(\vec{u})] \hat{y} + \frac{\partial}{\partial z} [div(\vec{u})] \hat{z} \quad (\text{Eq. B16})$$

$$\begin{aligned} grad(div(\vec{u})) &= \frac{\partial}{\partial x} \left[\frac{\partial}{\partial x} u_x + \frac{\partial}{\partial y} u_y + \frac{\partial}{\partial z} u_z \right] \hat{x} + \dots \\ &\quad \frac{\partial}{\partial y} \left[\frac{\partial}{\partial x} u_x + \frac{\partial}{\partial y} u_y + \frac{\partial}{\partial z} u_z \right] \hat{y} + \dots \\ &\quad \frac{\partial}{\partial z} \left[\frac{\partial}{\partial x} u_x + \frac{\partial}{\partial y} u_y + \frac{\partial}{\partial z} u_z \right] \hat{z} \end{aligned} \quad (\text{Eq. B17})$$

Likewise, Equation B7 also involves the divergence of the gradient of \vec{u} , or the Laplacian of \vec{u} (given by the $\nabla^2 \vec{u}$ term). As \vec{u} is a vector, the gradient of \vec{u} represents a tensor (denoted as Q for visual simplification) while the Laplacian of \vec{u} represents a vector:

$$grad(\vec{u}) = Q = \begin{bmatrix} \partial u_x / \partial x & \partial u_x / \partial y & \partial u_x / \partial z \\ \partial u_y / \partial x & \partial u_y / \partial y & \partial u_y / \partial z \\ \partial u_z / \partial x & \partial u_z / \partial y & \partial u_z / \partial z \end{bmatrix} \quad (\text{Eq. B18})$$

$$\nabla^2 \vec{u} = div(grad(\vec{u})) = div(Q) =$$

$$\begin{aligned} &\left(\frac{\partial Q_{xx}}{\partial x} + \frac{\partial Q_{xy}}{\partial y} + \frac{\partial Q_{xz}}{\partial z} \right) \hat{x} + \left(\frac{\partial Q_{yx}}{\partial x} + \frac{\partial Q_{yy}}{\partial y} + \frac{\partial Q_{yz}}{\partial z} \right) \hat{y} + \dots \\ &\left(\frac{\partial Q_{zx}}{\partial x} + \frac{\partial Q_{zy}}{\partial y} + \frac{\partial Q_{zz}}{\partial z} \right) \hat{z} \end{aligned} \quad (\text{Eq. B19})$$

Substituting Equation B18 into B19 gives:

$$\begin{aligned}\nabla^2 \vec{u} = & \left(\frac{\partial}{\partial x} \frac{\partial u_x}{\partial x} + \frac{\partial}{\partial y} \frac{\partial u_x}{\partial y} + \frac{\partial}{\partial z} \frac{\partial u_x}{\partial z} \right) \hat{x} + \dots \\ & \left(\frac{\partial}{\partial x} \frac{\partial u_y}{\partial x} + \frac{\partial}{\partial y} \frac{\partial u_y}{\partial y} + \frac{\partial}{\partial z} \frac{\partial u_y}{\partial z} \right) \hat{y} + \dots \\ & \left(\frac{\partial}{\partial x} \frac{\partial u_z}{\partial x} + \frac{\partial}{\partial y} \frac{\partial u_z}{\partial y} + \frac{\partial}{\partial z} \frac{\partial u_z}{\partial z} \right) \hat{z}\end{aligned}\quad (\text{Eq. B20})$$

Plugging each component (the \hat{x} , \hat{y} , and \hat{z} components, respectively) of Equations B17 and B20 into each component of Equation B7 results in the below:

For \hat{x} :

$$(\lambda_s + \mu_s) \left(\frac{\partial}{\partial x} \left[\frac{\partial}{\partial x} u_x + \frac{\partial}{\partial y} u_y + \frac{\partial}{\partial z} u_z \right] \right) + \mu_s \left(\frac{\partial}{\partial x} \frac{\partial u_x}{\partial x} + \frac{\partial}{\partial y} \frac{\partial u_x}{\partial y} + \frac{\partial}{\partial z} \frac{\partial u_x}{\partial z} \right)$$

which equals:

$$\begin{aligned}\lambda_s \left(\frac{\partial}{\partial x} \frac{\partial u_x}{\partial x} + \frac{\partial}{\partial x} \frac{\partial u_y}{\partial y} + \frac{\partial}{\partial x} \frac{\partial u_z}{\partial z} \right) + \mu_s \left(\frac{\partial}{\partial x} \frac{\partial u_x}{\partial x} + \frac{\partial}{\partial x} \frac{\partial u_y}{\partial y} + \frac{\partial}{\partial x} \frac{\partial u_z}{\partial z} \right) + \dots \\ \mu_s \left(\frac{\partial}{\partial x} \frac{\partial u_x}{\partial x} + \frac{\partial}{\partial y} \frac{\partial u_x}{\partial y} + \frac{\partial}{\partial z} \frac{\partial u_x}{\partial z} \right)\end{aligned}$$

which equals:

$$\begin{aligned}\lambda_s \left(\frac{\partial}{\partial x} \frac{\partial u_x}{\partial x} + \frac{\partial}{\partial x} \frac{\partial u_y}{\partial y} + \frac{\partial}{\partial x} \frac{\partial u_z}{\partial z} \right) + \dots \\ \mu_s \left(2 \frac{\partial}{\partial x} \frac{\partial u_x}{\partial x} + \frac{\partial}{\partial x} \frac{\partial u_y}{\partial y} + \frac{\partial}{\partial x} \frac{\partial u_z}{\partial z} + \frac{\partial}{\partial y} \frac{\partial u_x}{\partial y} + \frac{\partial}{\partial z} \frac{\partial u_x}{\partial z} \right)\end{aligned}\quad (\text{Eq. B21a})$$

For \hat{y} :

$$(\lambda_s + \mu_s) \left(\frac{\partial}{\partial y} \left[\frac{\partial}{\partial x} u_x + \frac{\partial}{\partial y} u_y + \frac{\partial}{\partial z} u_z \right] \right) + \mu_s \left(\frac{\partial}{\partial x} \frac{\partial u_y}{\partial x} + \frac{\partial}{\partial y} \frac{\partial u_y}{\partial y} + \frac{\partial}{\partial z} \frac{\partial u_y}{\partial z} \right)$$

which equals:

$$\lambda_s \left(\frac{\partial}{\partial y} \frac{\partial u_x}{\partial x} + \frac{\partial}{\partial y} \frac{\partial u_y}{\partial y} + \frac{\partial}{\partial y} \frac{\partial u_z}{\partial z} \right) + \mu_s \left(\frac{\partial}{\partial y} \frac{\partial u_x}{\partial x} + \frac{\partial}{\partial y} \frac{\partial u_y}{\partial y} + \frac{\partial}{\partial y} \frac{\partial u_z}{\partial z} \right) \dots$$

$$\mu_s \left(\frac{\partial}{\partial x} \frac{\partial u_y}{\partial x} + \frac{\partial}{\partial y} \frac{\partial u_y}{\partial y} + \frac{\partial}{\partial z} \frac{\partial u_y}{\partial z} \right)$$

which equals:

$$\lambda_s \left(\frac{\partial}{\partial y} \frac{\partial u_x}{\partial x} + \frac{\partial}{\partial y} \frac{\partial u_y}{\partial y} + \frac{\partial}{\partial y} \frac{\partial u_z}{\partial z} \right) + \dots$$

$$\mu_s \left(2 \frac{\partial}{\partial y} \frac{\partial u_y}{\partial y} + \frac{\partial}{\partial y} \frac{\partial u_x}{\partial x} + \frac{\partial}{\partial y} \frac{\partial u_z}{\partial z} + \frac{\partial}{\partial x} \frac{\partial u_y}{\partial x} + \frac{\partial}{\partial z} \frac{\partial u_y}{\partial z} \right) \quad (\text{Eq. B21b})$$

For \hat{z} :

$$(\lambda_s + \mu_s) \left(\frac{\partial}{\partial z} \left[\frac{\partial}{\partial x} u_x + \frac{\partial}{\partial y} u_y + \frac{\partial}{\partial z} u_z \right] \right) + \mu_s \left(\frac{\partial}{\partial x} \frac{\partial u_z}{\partial x} + \frac{\partial}{\partial y} \frac{\partial u_z}{\partial y} + \frac{\partial}{\partial z} \frac{\partial u_z}{\partial z} \right)$$

which equals:

$$\lambda_s \left(\frac{\partial}{\partial z} \frac{\partial u_x}{\partial x} + \frac{\partial}{\partial z} \frac{\partial u_y}{\partial y} + \frac{\partial}{\partial z} \frac{\partial u_z}{\partial z} \right) + \mu_s \left(\frac{\partial}{\partial z} \frac{\partial u_x}{\partial x} + \frac{\partial}{\partial z} \frac{\partial u_y}{\partial y} + \frac{\partial}{\partial z} \frac{\partial u_z}{\partial z} \right) \dots$$

$$\mu_s \left(\frac{\partial}{\partial x} \frac{\partial u_z}{\partial x} + \frac{\partial}{\partial y} \frac{\partial u_z}{\partial y} + \frac{\partial}{\partial z} \frac{\partial u_z}{\partial z} \right)$$

which equals:

$$\lambda_s \left(\frac{\partial}{\partial z} \frac{\partial u_x}{\partial x} + \frac{\partial}{\partial z} \frac{\partial u_y}{\partial y} + \frac{\partial}{\partial z} \frac{\partial u_z}{\partial z} \right) + \dots$$

$$\mu_s \left(2 \frac{\partial}{\partial z} \frac{\partial u_z}{\partial z} + \frac{\partial}{\partial z} \frac{\partial u_x}{\partial x} + \frac{\partial}{\partial z} \frac{\partial u_y}{\partial y} + \frac{\partial}{\partial x} \frac{\partial u_z}{\partial x} + \frac{\partial}{\partial y} \frac{\partial u_z}{\partial y} \right) \quad (\text{Eq. B21c})$$

Term-by-term comparison of the components of Equations B13 and B21 (so comparing terms of B13a to B21a, terms of B13b to B21b, and terms of B13c to B21c) illustrates their equivalency.

Appendix C

Equation 21 can be simplified to 1D resulting in Equation 31, as detailed below.

$$-grad(p) + (\lambda_s + \mu_s)grad(div(\bar{u})) + \mu_s \nabla^2 \bar{u} = 0 \quad (\text{Eq. 21})$$

$$-\frac{\partial p}{\partial z} + (\lambda_s + \mu_s) \frac{\partial^2 u_z}{\partial z^2} + \mu_s \frac{\partial^2 u_z}{\partial z^2} = 0 \quad (\text{Eq. 31})$$

As p represents the magnitude of the hydrostatic pressure, $grad(p)$ represents a vector:

$$grad(p) = \frac{\partial p}{\partial x} \hat{x} + \frac{\partial p}{\partial y} \hat{y} + \frac{\partial p}{\partial z} \hat{z} \quad (\text{Eq. C1})$$

where $\hat{x}, \hat{y}, \hat{z}$ = unit vectors representing the three orthogonal directions of a Cartesian coordinate system

Therefore, in 1D (z), Equation C1 becomes:

$$grad(p) = \frac{\partial p}{\partial z} \hat{z} \quad (\text{Eq. C2})$$

Similarly, \bar{u} represents the displacement of the solid matrix and is a vector:

$$\bar{u} = u_x \hat{x} + u_y \hat{y} + u_z \hat{z} \quad (\text{Eq. C3})$$

As such, $div(\bar{u})$ represents a scalar, while $grad(div(\bar{u}))$ represents a vector:

$$div(\bar{u}) = \frac{\partial}{\partial x} u_x + \frac{\partial}{\partial y} u_y + \frac{\partial}{\partial z} u_z \quad (\text{Eq. C4})$$

$$grad(div(\bar{u})) = \frac{\partial}{\partial x} [div(\bar{u})] \hat{x} + \frac{\partial}{\partial y} [div(\bar{u})] \hat{y} + \frac{\partial}{\partial z} [div(\bar{u})] \hat{z} \quad (\text{Eq. C5})$$

$$\begin{aligned} grad(div(\bar{u})) &= \frac{\partial}{\partial x} \left[\frac{\partial}{\partial x} u_x + \frac{\partial}{\partial y} u_y + \frac{\partial}{\partial z} u_z \right] \hat{x} + \dots \\ &\quad \frac{\partial}{\partial y} \left[\frac{\partial}{\partial x} u_x + \frac{\partial}{\partial y} u_y + \frac{\partial}{\partial z} u_z \right] \hat{y} + \dots \\ &\quad \frac{\partial}{\partial z} \left[\frac{\partial}{\partial x} u_x + \frac{\partial}{\partial y} u_y + \frac{\partial}{\partial z} u_z \right] \hat{z} \end{aligned} \quad (\text{Eq. C6})$$

Therefore, in 1D (z) and as both u_x and u_y equal zero, Equation C6 becomes:

$$\mathit{grad}(\mathit{div}(\vec{u})) = \frac{\partial}{\partial z} \left[\frac{\partial}{\partial z} u_z \right] \hat{z} = \frac{\partial^2 u_z}{\partial z^2} \hat{z} \quad (\text{Eq. C7})$$

Next, as \vec{u} is a vector, the gradient of \vec{u} represents a tensor (denoted as Q for visual simplification) while the Laplacian of \vec{u} (denoted as $\nabla^2 \vec{u}$) represents a vector:

$$\mathit{grad}(\vec{u}) = Q = \begin{bmatrix} \partial u_x / \partial x & \partial u_x / \partial y & \partial u_x / \partial z \\ \partial u_y / \partial x & \partial u_y / \partial y & \partial u_y / \partial z \\ \partial u_z / \partial x & \partial u_z / \partial y & \partial u_z / \partial z \end{bmatrix} \quad (\text{Eq. C8})$$

$$\begin{aligned} \nabla^2 \vec{u} &= \mathit{div}(\mathit{grad}(\vec{u})) = \mathit{div}(Q) = \\ & \left(\frac{\partial Q_{xx}}{\partial x} + \frac{\partial Q_{xy}}{\partial y} + \frac{\partial Q_{xz}}{\partial z} \right) \hat{x} + \left(\frac{\partial Q_{yx}}{\partial x} + \frac{\partial Q_{yy}}{\partial y} + \frac{\partial Q_{yz}}{\partial z} \right) \hat{y} + \dots \\ & \left(\frac{\partial Q_{zx}}{\partial x} + \frac{\partial Q_{zy}}{\partial y} + \frac{\partial Q_{zz}}{\partial z} \right) \hat{z} \end{aligned} \quad (\text{Eq. C9})$$

Substituting Equation C8 into C9 gives:

$$\begin{aligned} \nabla^2 \vec{u} &= \left(\frac{\partial}{\partial x} \frac{\partial u_x}{\partial x} + \frac{\partial}{\partial y} \frac{\partial u_x}{\partial y} + \frac{\partial}{\partial z} \frac{\partial u_x}{\partial z} \right) \hat{x} + \dots \\ & \left(\frac{\partial}{\partial x} \frac{\partial u_y}{\partial x} + \frac{\partial}{\partial y} \frac{\partial u_y}{\partial y} + \frac{\partial}{\partial z} \frac{\partial u_y}{\partial z} \right) \hat{y} + \dots \\ & \left(\frac{\partial}{\partial x} \frac{\partial u_z}{\partial x} + \frac{\partial}{\partial y} \frac{\partial u_z}{\partial y} + \frac{\partial}{\partial z} \frac{\partial u_z}{\partial z} \right) \hat{z} \end{aligned} \quad (\text{Eq. C10})$$

Therefore, in 1D (z) and as both u_x and u_y equal zero, Equation C10 becomes:

$$\nabla^2 \vec{u} = \frac{\partial^2 u_z}{\partial z^2} \hat{z} \quad (\text{Eq. C11})$$

Substituting Equations C2, C7, and C11 back into Equation 21 yields:

$$-\frac{\partial p}{\partial z} + (\lambda_s + \mu_s) \frac{\partial^2 u_z}{\partial z^2} + \mu_s \frac{\partial^2 u_z}{\partial z^2} = 0 \quad (\text{Eq. C12})$$

Equation C12 is identical to Equation 31.

Appendix D

Equation 29 can be simplified to 1D resulting in Equation 35, as detailed below.

$$\text{div}(\vec{v}^s + \vec{w}) = 0 \quad (\text{Eq. 29})$$

$$\frac{\partial}{\partial z} \left(\frac{\partial u_z}{\partial t} + w_z \right) = 0 \quad (\text{Eq. 35})$$

As both \vec{v}^s and \vec{w} are vectors, $\text{div}(\vec{v}^s + \vec{w})$ is a scalar:

$$\text{div}(\vec{v}^s + \vec{w}) = \frac{\partial}{\partial x} (v_x^s + w_x) + \frac{\partial}{\partial y} (v_y^s + w_y) + \frac{\partial}{\partial z} (v_z^s + w_z) \quad (\text{Eq. D1})$$

In 1D (z), Equation D1 becomes:

$$\text{div}(\vec{v}^s + \vec{w}) = \frac{\partial}{\partial z} (v_z^s + w_z) \quad (\text{Eq. D2})$$

Next, the velocity in the z direction is equal to the change in displacement over time:

$$v_z^s = \frac{\partial u_z}{\partial t} \quad (\text{Eq. D3})$$

Plugging Equation D3 into D2 results in:

$$\text{div}(\vec{v}^s + \vec{w}) = \frac{\partial}{\partial z} \left(\frac{\partial u_z}{\partial t} + w_z \right) \quad (\text{Eq. D4})$$

Finally, substituting Equation D4 back into Equation 29 yields:

$$\frac{\partial}{\partial z} \left(\frac{\partial u_z}{\partial t} + w_z \right) = 0 \quad (\text{Eq. D5})$$

Equation D5 is identical to Equation 35.

Appendix E

As stated in Section 2.3.1.4, the confined compression creep problem is given by Equation 45, subject to Equations 46, 47, and 50 (Ateshian, 2017; Mow et al., 1980):

$$\frac{\partial^2 u_z}{\partial z^2} - \frac{1}{H_A k} \frac{\partial u_z}{\partial t} = 0 \quad (\text{governing PDE}) \quad (\text{Eq. 45})$$

$$u_z(z, t = 0) = 0 \quad (\text{initial condition}) \quad (\text{Eq. 46})$$

$$u_z(z = h, t) = 0 \quad (\text{boundary condition}) \quad (\text{Eq. 47})$$

$$-\sigma_0 = H_A \frac{\partial u_{z=0}}{\partial z} \quad (\text{boundary condition}) \quad (\text{Eq. 50})$$

Equation 45 can be expressed as a formulation of the heat equation:

$$\frac{\partial u}{\partial t} = \alpha^2 \frac{\partial^2 u}{\partial z^2} \quad (\text{Eq. E1a})$$

$$\text{where } \alpha^2 = H_A k \quad (\text{Eq. E1b})$$

This heat equation can be solved using eigenfunction expansion to reformulate the given PDE (Equations E1, 46, 47, and 50) in a form that can be solved via separation of variables (steps 1 and 2), and then using separation of variables (step 3) to solve the reformulated PDE, as presented below. In the following, the symbol “∴” represents “therefore”.

1) Look for a steady-state solution; denote as $u_\infty(z)$

As such, Equation E1a becomes:

$$0 = \alpha^2 \frac{\partial^2 u_\infty(z)}{\partial z^2} \quad (\text{Eq. E2})$$

$$\text{Let } u_\infty(z) = A_1 z + B_1 \quad (\text{Eq. E3a})$$

$$\therefore \frac{\partial u_{\infty}(z)}{\partial z} = A_1 \quad (\text{Eq. E3b})$$

where $A_1, B_1 =$ values to be determined from the boundary conditions

Applying the boundary condition of Equation 50 gives:

$$H_A \frac{\partial u_{\infty}(0)}{\partial z} = -\sigma_0 \quad (\text{Eq. E4})$$

$$\frac{\partial u_{\infty}(0)}{\partial z} = -\frac{\sigma_0}{H_A} \quad (\text{Eq. E5})$$

Substituting Equation E3b into Equation E5 results in:

$$A_1 = -\frac{\sigma_0}{H_A} \quad (\text{Eq. E6})$$

Applying the boundary condition of Equation 47 gives:

$$u_{\infty}(h) = 0 \quad (\text{Eq. E7})$$

Substituting Equation E3a into Equation E7 results in:

$$A_1(h) + B_1 = 0 \quad (\text{Eq. E8})$$

Plugging Equation E6 into E8 yields:

$$-\frac{\sigma_0}{H_A}(h) + B_1 = 0 \quad (\text{Eq. E9})$$

$$B_1 = \frac{\sigma_0}{H_A}(h) \quad (\text{Eq. E10})$$

Using the results of Equations E6 and E10 to re-express Equation E3a yields:

$$u_{\infty}(z) = -\frac{\sigma_0}{H_A}z + \frac{\sigma_0}{H_A}(h) \quad (\text{Eq. E11})$$

$$u_{\infty}(z) = -\frac{\sigma_0}{H_A}(z - h) \quad (\text{Eq. E12})$$

2) Express the full solution ($u(z, t)$) as a linear combination of the steady-state ($u_\infty(z)$) and transient solutions ($v(z, t)$)

$$\therefore u(z, t) = u_\infty(z) + v(z, t) \quad (\text{Eq. E13})$$

In this formulation, $u_\infty(z)$ represents the steady-state solution while $v(z, t)$ is an eigenfunction representing the transient solution.

Plugging Equation E12 into Equation E13 results in:

$$u(z, t) = -\frac{\sigma_0}{H_A}(z - h) + v(z, t) \quad (\text{Eq. E14})$$

$$\therefore \frac{\partial}{\partial z}(u(z, t)) = \frac{\partial}{\partial z}\left(-\frac{\sigma_0}{H_A}(z - h)\right) + \frac{\partial}{\partial z}(v(z, t)) \quad (\text{Eq. E15})$$

$$\frac{\partial}{\partial z}(u(z, t)) = -\frac{\sigma_0}{H_A} + \frac{\partial}{\partial z}(v(z, t)) \quad (\text{Eq. E16})$$

Substituting Equation E14 into Equation E1a yields:

$$\frac{\partial u(z, t)}{\partial t} = \alpha^2 \frac{\partial^2 u(z, t)}{\partial z^2} \quad (\text{Eq. E17})$$

$$\frac{\partial}{\partial t}\left(-\frac{\sigma_0}{H_A}(z - h) + v(z, t)\right) = \alpha^2 \frac{\partial^2}{\partial z^2}\left(-\frac{\sigma_0}{H_A}(z - h) + v(z, t)\right) \quad (\text{Eq. E18})$$

$$\frac{\partial}{\partial t}\left(-\frac{\sigma_0}{H_A}(z - h)\right) + \frac{\partial}{\partial t}(v(z, t)) = \dots$$

$$\dots \alpha^2 \frac{\partial^2}{\partial z^2}\left(-\frac{\sigma_0}{H_A}(z - h)\right) + \alpha^2 \frac{\partial^2}{\partial z^2}(v(z, t)) \quad (\text{Eq. E19})$$

$$0 + \frac{\partial}{\partial t}(v(z, t)) = 0 + \alpha^2 \frac{\partial^2}{\partial z^2}(v(z, t)) \quad (\text{Eq. E20})$$

$$\therefore \frac{\partial}{\partial t}(v(z, t)) = \alpha^2 \frac{\partial^2}{\partial z^2}(v(z, t)) \quad (\text{new PDE}) \quad (\text{Eq. E21})$$

Similarly, substituting Equation E14 into Equation 46 (the initial condition) gives:

$$-\frac{\sigma_0}{H_A}(z - h) + v(z, 0) = 0 \quad (\text{Eq. E22})$$

$$\therefore v(z, 0) = \frac{\sigma_0}{H_A} (z - h) \quad (\text{new initial condition}) \quad (\text{Eq. E23})$$

Likewise, substituting Equation E14 into Equation 47 results in:

$$-\frac{\sigma_0}{H_A} (h - h) + v(h, t) = 0 \quad (\text{Eq. E24})$$

$$0 + v(h, t) = 0 \quad (\text{Eq. E25})$$

$$\therefore v(h, t) = 0 \quad (\text{new boundary condition}) \quad (\text{Eq. E26})$$

Finally, plugging Equation E14 into Equation 50 yields:

$$-\sigma_0 = H_A \frac{\partial}{\partial z} (u(0, t)) \quad (\text{Eq. E27})$$

$$-\sigma_0 = H_A \left[-\frac{\sigma_0}{H_A} + \frac{\partial}{\partial z} (v(0, t)) \right] \quad (\text{Eq. E28})$$

$$-\sigma_0 = -\sigma_0 + H_A \frac{\partial}{\partial z} (v(0, t)) \quad (\text{Eq. E29})$$

$$0 = H_A \frac{\partial}{\partial z} (v(0, t)) \quad (\text{Eq. E30})$$

$$\therefore 0 = \frac{\partial}{\partial z} (v(0, t)) \quad (\text{new boundary condition}) \quad (\text{Eq. E31})$$

Together, Equations E21, E23, E26, and E31 represent a PDE reformulated in terms of the eigenfunction $v(z, t)$ that can be solved using separation of variables.

3) Use separation of variables to solve reformulated PDE

The reformulated PDE is as follows:

$$\frac{\partial}{\partial t} (v(z, t)) = \alpha^2 \frac{\partial^2}{\partial z^2} (v(z, t)) \quad (\text{new PDE}) \quad (\text{Eq. E21})$$

$$v(z, 0) = \frac{\sigma_0}{H_A} (z - h) \quad (\text{new initial condition}) \quad (\text{Eq. E23})$$

$$v(h, t) = 0 \quad (\text{new boundary condition}) \quad (\text{Eq. E26})$$

$$\frac{\partial}{\partial z}(v(0, t)) = 0 \quad (\text{new boundary condition}) \quad (\text{Eq. E31})$$

Let the eigenfunction $v(z, t)$ be separable into two functions, each solely dependent on one variable only (either space, z , or time, t):

$$v(z, t) = Z(z)T(t) \quad (\text{Eq. E32})$$

Plugging Equation E32 back into Equation E21 results in:

$$Z(z) \frac{d}{dt}(T(t)) = \alpha^2 T(t) \frac{d^2}{dz^2}(Z(z)) \quad (\text{Eq. E33})$$

$$\frac{d}{dt}(T(t)) / \alpha^2 T(t) = \frac{d^2}{dz^2}(Z(z)) / Z(z) \quad (\text{Eq. E34})$$

The only way Equation E34 can be true is if both the right and left sides equal the same constant, denoted as $-\lambda^2$:

$$\frac{d}{dt}(T(t)) / \alpha^2 T(t) = \frac{d^2}{dz^2}(Z(z)) / Z(z) = -\lambda^2 \quad (\text{Eq. E35})$$

In this way, the PDE represented by Equation E21 (and Equation E33) can be separated into two ordinary differential equations (ODEs) (Equations E36 and E37):

$$\frac{d}{dt}(T(t)) / \alpha^2 T(t) = -\lambda^2$$

which equals

$$\frac{dT(t)}{dt} + \lambda^2 \alpha^2 T(t) = 0 \quad (\text{Eq. E36})$$

$$\frac{d^2}{dz^2}(Z(z)) / Z(z) = -\lambda^2$$

which equals

$$\frac{d^2 Z(z)}{dz^2} + \lambda^2 Z(z) = 0 \quad (\text{Eq. E37})$$

Equation E36 represents a well-known ODE with the following solution:

$$T(t) = be^{-\alpha^2 \lambda^2 t} \quad (\text{Eq. E38})$$

where b is a constant to be determined from the boundary conditions.

For Equation E37, a general solution is:

$$Z(z) = A_2 \cos(\lambda z) + B_2 \sin(\lambda z) \quad (\text{Eq. E39})$$

$$\therefore \frac{dZ(z)}{dz} = -\lambda A_2 \sin(\lambda z) + \lambda B_2 \cos(\lambda z) \quad (\text{Eq. E40})$$

Plugging the first derivative of the general solution (Equation E40) into the second boundary condition, Equation E31, gives:

$$-\lambda A_2 \sin(\lambda(0)) + \lambda B_2 \cos(\lambda(0)) = 0 \quad (\text{Eq. E41})$$

$$-\lambda A_2 \sin(0) + \lambda B_2 \cos(0) = 0 \quad (\text{Eq. E42})$$

$$0 + \lambda B_2 = 0 \quad (\text{Eq. E43})$$

$$\therefore B_2 = 0 \quad (\text{Eq. E44})$$

Substituting this result (Equation E44) back into Equation E39 yields:

$$Z(z) = A_2 \cos(\lambda z) \quad (\text{Eq. E45})$$

Next, plugging the simplified general solution (Eq. E45) into the first boundary condition, Equation E26, results in:

$$A_2 \cos(\lambda h) = 0 \quad (\text{Eq. E46})$$

In Equation E46, A_2 must be strictly nonzero, as otherwise this would result in the trivial solution ($Z(z) = 0 \therefore v(z, t) = 0$). As a result, A_2 can be chosen for convenience:

$$A_2 = 1 \quad (\text{Eq. E47})$$

Therefore, the following (Equation E48) must be true to satisfy Equation E46:

$$\cos(\lambda h) = 0 \quad (\text{Eq. E48})$$

Equation E48 is satisfied when $\lambda = \frac{\pi}{2h}, \frac{3\pi}{2h}, \frac{5\pi}{2h}, \dots$. This can be represented as:

$$\lambda_n = \frac{(2n+1)\pi}{2h} \quad n = 0, 1, 2, 3 \dots \quad (\text{Eq. E49})$$

Substituting Equations E47 and E49 back into Equation E45 gives:

$$Z(z) = (1)\cos(\lambda_n z) \quad (\text{Eq. E50})$$

$$Z(z) = \cos\left(\frac{(2n+1)\pi}{2h} z\right) \quad (\text{Eq. E51})$$

Now, both separable functions comprising $v(z, t)$ (Equation E32) have been determined, so they (Equations E38 and E51, together with Equation E49) can be plugged back into Equation E32 to define the eigenfunction:

$$v(z, t) = b e^{-\alpha^2 \left(\frac{(2n+1)\pi}{2h}\right)^2 t} \cos\left(\frac{(2n+1)\pi}{2h} z\right) \quad (\text{Eq. E52a})$$

or equivalently,

$$v(z, t) = b e^{-\alpha^2 \left(\frac{(n+\frac{1}{2})\pi}{h}\right)^2 t} \cos\left(\left(n + \frac{1}{2}\right)\pi \frac{z}{h}\right) \quad (\text{Eq. E52b})$$

To obtain a solution that also satisfies the initial condition (Equation E23), a Fourier series of the eigenfunctions $v(z, t)$ is considered:

$$v(z, t) = \sum_{n=0}^{\infty} b_n e^{-\alpha^2 \left(\frac{(2n+1)\pi}{2h}\right)^2 t} \cos\left(\frac{(2n+1)\pi}{2h} z\right) \quad (\text{Eq. E53a})$$

or equivalently,

$$v(z, t) = \sum_{n=0}^{\infty} b_n e^{-\alpha^2 \left(\frac{(n+\frac{1}{2})\pi}{h}\right)^2 t} \cos\left(\left(n + \frac{1}{2}\right) \pi \frac{z}{h}\right) \quad (\text{Eq. E53b})$$

Substituting Equation E53a into Equation E23, the initial condition, gives:

$$\sum_{n=0}^{\infty} b_n e^{-\alpha^2 \lambda_n^2(0)} \cos\left(\frac{(2n+1)\pi}{2h} z\right) = \frac{\sigma_a}{H_A} (z - h) \quad (\text{Eq. E54})$$

$$\sum_{n=0}^{\infty} b_n (1) \cos\left(\frac{(2n+1)\pi}{2h} z\right) = \frac{\sigma_a}{H_A} (z - h) \quad (\text{Eq. E55})$$

$$\sum_{n=0}^{\infty} b_n \cos\left(\frac{(2n+1)\pi}{2h} z\right) = \frac{\sigma_a}{H_A} (z - h) \quad (\text{Eq. E56})$$

Equation E56 represents a Fourier cosine series as it is an even function. In this manner, the coefficients of the Fourier cosine series (b_n) are determined as:

$$b_n = \frac{2}{h} \int_0^h \frac{\sigma_0}{H_A} (z - h) \cos\left(\frac{(2n+1)\pi}{2h} z\right) dz \quad (\text{Eq. E57})$$

$$b_n = \frac{2\sigma_0}{H_A h} \int_0^h (z - h) \cos\left(\frac{(2n+1)\pi}{2h} z\right) dz \quad (\text{Eq. E58})$$

For visual simplification, define the following term:

$$\gamma_n = \frac{(2n+1)\pi}{2} = \left(n + \frac{1}{2}\right) \pi \quad (\text{Eq. E59})$$

Using Equation E59, Equation E58 becomes:

$$b_n = \frac{2\sigma_0}{H_A h} \int_0^h (z - h) \cos\left(\gamma_n \frac{z}{h}\right) dz \quad (\text{Eq. E60})$$

Equation E60 is an integral that can be solved using integration by parts:

$$\int f(z) \frac{dg(z)}{dz} dz = g(z)f(z) - \int g(z) \frac{df(z)}{dz} dz \quad (\text{Eq. E61a})$$

$$\text{where } f(z) = (z - h) \quad (\text{Eq. E61b})$$

$$\frac{df(z)}{dz} = 1 \quad (\text{Eq. E61c})$$

$$g(z) = \frac{h}{\gamma_n} \sin\left(\gamma_n \frac{z}{h}\right) \quad (\text{Eq. E61d})$$

$$\frac{dg(z)}{dz} = \cos\left(\gamma_n \frac{z}{h}\right) \quad (\text{Eq. E61e})$$

Plugging Equation E61 (a-e) into Equation E60 results in:

$$b_n = \frac{2\sigma_0}{H_A h} \left[\frac{h}{\gamma_n} (z - h) \sin\left(\gamma_n \frac{z}{h}\right) \Big|_0^h - \int_0^h \frac{h}{\gamma_n} \sin\left(\gamma_n \frac{z}{h}\right) dz \right] \quad (\text{Eq. E62})$$

$$b_n = \frac{2\sigma_0}{H_A} \left[\frac{1}{\gamma_n} (z - h) \sin\left(\gamma_n \frac{z}{h}\right) \Big|_0^h + \int_0^h -\frac{1}{\gamma_n} \sin\left(\gamma_n \frac{z}{h}\right) dz \right] \quad (\text{Eq. E63})$$

$$b_n = \frac{2\sigma_0}{H_A} \left[\left(\frac{1}{\gamma_n} (h - h) \sin\left(\gamma_n \frac{h}{h}\right) - \frac{1}{\gamma_n} (0 - h) \sin\left(\gamma_n \frac{0}{h}\right) \right) \right] + \dots$$

$$\frac{2\sigma_0}{H_A} \left[\int_0^h -\frac{1}{\gamma_n} \sin\left(\gamma_n \frac{z}{h}\right) dz \right] \quad (\text{Eq. E64})$$

$$b_n = \frac{2\sigma_0}{H_A} \left[\left(\frac{1}{\gamma_n} (0) \sin(\gamma_n(1)) + \frac{1}{\gamma_n} (h) \sin(\gamma_n(0)) \right) \right] + \dots$$

$$\frac{2\sigma_0}{H_A} \left[\int_0^h -\frac{1}{\gamma_n} \sin\left(\gamma_n \frac{z}{h}\right) dz \right] \quad (\text{Eq. E65})$$

$$b_n = \frac{2\sigma_0}{H_A} [0 + 0] + \frac{2\sigma_0}{H_A} \left[\int_0^h -\frac{1}{\gamma_n} \sin\left(\gamma_n \frac{z}{h}\right) dz \right] \quad (\text{Eq. E66})$$

$$b_n = \frac{2\sigma_0}{H_A} \left[\int_0^h -\frac{1}{\gamma_n} \sin\left(\gamma_n \frac{z}{h}\right) dz \right] \quad (\text{Eq. E67})$$

$$b_n = \frac{2\sigma_0}{H_A} \left[\left(\frac{h}{\gamma_n^2} \right) \cos\left(\gamma_n \frac{z}{h}\right) \Big|_0^h \right] \quad (\text{Eq. E68})$$

$$b_n = \frac{2\sigma_0}{H_A} \left[\left(\frac{h}{\gamma_n^2} \right) \cos\left(\gamma_n \frac{h}{h}\right) - \left(\frac{h}{\gamma_n^2} \right) \cos\left(\gamma_n \frac{0}{h}\right) \right] \quad (\text{Eq. E69})$$

$$b_n = \frac{2\sigma_0}{H_A} \left[\left(\frac{h}{\gamma_n^2} \right) \cos(\gamma_n(1)) - \left(\frac{h}{\gamma_n^2} \right) \cos(\gamma_n(0)) \right] \quad (\text{Eq. E70})$$

$$b_n = \frac{2\sigma_0}{H_A} \left[\left(\frac{h}{\gamma_n^2} \right) \cos(\gamma_n) - \left(\frac{h}{\gamma_n^2} \right) \cos(0) \right] \quad (\text{Eq. E71})$$

$$b_n = \frac{2\sigma_0}{H_A} \left(\frac{h}{\gamma_n^2} \right) [\cos(\gamma_n) - 1] \quad (\text{Eq. E72})$$

Plugging Equation E59 back into Equation E72 yields:

$$b_n = \frac{2\sigma_0}{H_A} \left(\frac{h}{\left(n + \frac{1}{2}\right)^2 \pi^2} \right) \left[\cos \left(\left(n + \frac{1}{2}\right) \pi \right) - 1 \right] \quad (\text{Eq. E73})$$

$$\text{where } \cos \left(\left(n + \frac{1}{2}\right) \pi \right) = 0 \quad \text{for all } n \quad (\text{Eq. E74})$$

$$b_n = \frac{2\sigma_0 h}{H_A \left(n + \frac{1}{2}\right)^2 \pi^2} [0 - 1] \quad (\text{Eq. E75})$$

$$b_n = \frac{-2\sigma_0 h}{H_A \left(n + \frac{1}{2}\right)^2 \pi^2} \quad (\text{Eq. E76})$$

Simplification of Equation E76 is made by defining Equation E77 below:

$$M = \pi^2 \left(n + \frac{1}{2} \right)^2 \quad (\text{Eq. E77})$$

Plugging Equation E77 into Equation E76 results in:

$$b_n = \frac{-2\sigma_0 h}{H_A M} \quad (\text{Eq. E78})$$

Plugging Equation E78 and Equation E1b into Equation E53b gives:

$$v(z, t) = \sum_{n=0}^{\infty} \left(\frac{-2\sigma_0 h}{H_A M} \right) e^{-\left(\frac{H_A k}{h}\right)^2 M t} \cos \left(\left(n + \frac{1}{2}\right) \pi \frac{z}{h} \right) \quad (\text{Eq. E79})$$

Next, defining the following equation (Equation E80) allows for further simplification of Equation E79:

$$\tau = \frac{h^2}{H_A k} \quad (\text{Eq. E80})$$

Therefore,

$$v(z, t) = \sum_{n=0}^{\infty} \left(\frac{-2\sigma_0 h}{H_A M} \right) e^{-\left(\frac{M}{\tau}\right)t} \cos\left(\left(n + \frac{1}{2}\right) \pi \frac{z}{h}\right) \quad (\text{Eq. E81})$$

Finally, putting it all together by plugging in the expressions for $u_{\infty}(z)$ (Equation E12) and $v(z, t)$ (Equation E81) into the expression for $u(z, t)$ (Equation E13) results in:

$$u(z, t) = \frac{-\sigma_0}{H_A} (z - h) + \sum_{n=0}^{\infty} \left(\frac{-2\sigma_0 h}{H_A M} \right) e^{-\left(\frac{M}{\tau}\right)t} \cos\left(\left(n + \frac{1}{2}\right) \pi \frac{z}{h}\right) \quad (\text{Eq. E82})$$

Equation E82 represents the solution to the PDE given by Equation 45, subject to Equations 46, 47, and 50 (Ateshian, 2017; Mow et al., 1980). However, the displacement of the solid matrix is most easily measured at $z = 0$, the surface where the load is applied (Figure 10). Plugging this value of z into Equation E82 yields:

$$u(0, t) = \frac{-\sigma_0}{H_A} (0 - h) + \sum_{n=0}^{\infty} \left(\frac{-2\sigma_0 h}{H_A M} \right) e^{-\left(\frac{M}{\tau}\right)t} \cos\left(\left(n + \frac{1}{2}\right) \pi \frac{0}{h}\right) \quad (\text{Eq. E83})$$

$$u(0, t) = \frac{\sigma_0 h}{H_A} + \sum_{n=0}^{\infty} \left(\frac{-2\sigma_0 h}{H_A M} \right) e^{-\left(\frac{M}{\tau}\right)t} \cos(0) \quad (\text{Eq. E84})$$

$$u(0, t) = \frac{\sigma_0 h}{H_A} + \sum_{n=0}^{\infty} \left(\frac{-2\sigma_0 h}{H_A M} \right) e^{-\left(\frac{M}{\tau}\right)t} (1) \quad (\text{Eq. E85})$$

$$u(0, t) = \frac{\sigma_0 h}{H_A} + \left(\frac{-2\sigma_0 h}{H_A} \right) \sum_{n=0}^{\infty} \frac{1}{M} e^{-\left(\frac{M}{\tau}\right)t} \quad (\text{Eq. E86})$$

$$u(0, t) = \frac{\sigma_0 h}{H_A} \left[1 - 2 \sum_{n=0}^{\infty} \frac{1}{M} e^{-\left(\frac{M}{\tau}\right)t} \right] \quad (\text{Eq. E87a})$$

or equivalently,

$$\frac{u(t)}{h} = \frac{\sigma_0}{H_A} \left[1 - 2 \sum_{n=0}^{\infty} \frac{1}{M} e^{-\left(\frac{M}{\tau}\right)t} \right] \quad (\text{Eq. E87b})$$

Equation E87b is identical to Equation 51, with both equations having identical definitions for M (Equations E77 and 52) and τ (Equations E80 and 53a).

References

- Aaboe, J., Henriksen, M., Bartholdy, C., Leonardis, J., Rider, P., Jørgensen, L., Christensen, R., Bliddal, H., Devita, P., 2014. The effect of quadriceps-strengthening exercise on quadriceps and knee biomechanics during walking in adults with knee osteoarthritis: a randomized controlled trial. *Osteoarthritis and Cartilage* 22, S80-S81.
- Akella, S.V., Reddy Regatte, R., Gougoutas, A.J., Borthakur, A., Shapiro, E.M., Kneeland, J.B., Leigh, J.S., Reddy, R., 2001. Proteoglycan-induced changes in T1ρ-relaxation of articular cartilage at 4T. *Magnetic Resonance in Medicine: An Official Journal of the International Society for Magnetic Resonance in Medicine* 46, 419-423.
- Akizuki, S., Mow, V., Lai, W., Pita, J., Howell, D., 1986a. Topographical variations of the biphasic indentation properties of human tibial plateau cartilage. *Trans. Orthop. Res. Soc* 11, 406.
- Akizuki, S., Mow, V.C., Müller, F., Pita, J.C., Howell, D.S., Manicourt, D.H., 1986b. Tensile properties of human knee joint cartilage: I. Influence of ionic conditions, weight bearing, and fibrillation on the tensile modulus. *Journal of Orthopaedic Research* 4, 379-392.
- Alexander, R., Jayes, A., 1983. A dynamic similarity hypothesis for the gaits of quadrupedal mammals. *Journal of Zoology* 201, 135-152.
- Alford, J.W., Cole, B.J., 2005a. Cartilage restoration, part 1: basic science, historical perspective, patient evaluation, and treatment options. *The American journal of sports medicine* 33, 295-306.
- Alford, J.W., Cole, B.J., 2005b. Cartilage restoration, part 2: techniques, outcomes, and future directions. *The American journal of sports medicine* 33, 443-460.
- Armstrong, C., Lai, W., Mow, V., 1984. An analysis of the unconfined compression of articular cartilage. *Journal of Biomechanical Engineering* 106, 165-173.
- Armstrong, C., Mow, V., 1982. Variations in the intrinsic mechanical properties of human articular cartilage with age, degeneration, and water content. *J Bone Joint Surg Am* 64, 88-94.
- Ateshian, G., Warden, W., Kim, J., Grelsamer, R., Mow, V., 1997. Finite deformation biphasic material properties of bovine articular cartilage from confined compression experiments. *Journal of Biomechanics* 30, 1157-1164.
- Ateshian, G.A., 2017. Mixture theory for modeling biological tissues: illustrations from articular cartilage, *Biomechanics: Trends in Modeling and Simulation*. Springer, pp. 1-51.

- Athanasίου, K., Agarwal, A., Dzida, F., 1994. Comparative study of the intrinsic mechanical properties of the human acetabular and femoral head cartilage. *Journal of Orthopaedic Research* 12, 340-349.
- Athanasίου, K., Agarwal, A., Muffoletto, A., Dzida, F., Constantinides, G., Clem, M., 1995a. Biomechanical properties of hip cartilage in experimental animal models. *Clinical orthopaedics and related research*, 254-266.
- Athanasίου, K., Niederauer, G., Schenck, R., 1995b. Biomechanical topography of human ankle cartilage. *Annals of biomedical engineering* 23, 697-704.
- Athanasίου, K., Rosenwasser, M., Buckwalter, J., Malinin, T., Mow, V., 1991. Interspecies comparisons of in situ intrinsic mechanical properties of distal femoral cartilage. *Journal of Orthopaedic Research* 9, 330-340.
- Atkinson, H.F., Birmingham, T.B., Moyer, R.F., Yacoub, D., Kanko, L.E., Bryant, D.M., Thiessen, J.D., Thompson, R.T., 2019. MRI T2 and T1ρ relaxation in patients at risk for knee osteoarthritis: a systematic review and meta-analysis. *BMC musculoskeletal disorders* 20, 182.
- Berger, M.J., McKenzie, C.A., Chess, D.G., Goela, A., Doherty, T.J., 2012. Quadriceps neuromuscular function and self-reported functional ability in knee osteoarthritis. *Journal of Applied Physiology* 113, 255-262.
- Best, B.A., Guilak, F., Setton, L.A., Zhu, W., Saed-Nejad, F., Ratcliffe, A., Weidenbaum, M., 1994. I Compressive mechanical properties of the human anulus fibrosus and their relationship to biochemical composition. *Spine* 19, 212-221.
- Beswick, A.D., Wylde, V., Gooberman-Hill, R., Blom, A., Dieppe, P., 2012. What proportion of patients report long-term pain after total hip or knee replacement for osteoarthritis? A systematic review of prospective studies in unselected patients. *BMJ open* 2, e000435.
- Bonassar, L.J., Frank, E.H., Murray, J.C., Pagnio, C.G., Moore, V.L., Lark, M.W., Sandy, J.D., Wu, J.J., Eyre, D.R., Grodzinsky, A.J., 1995. Changes in cartilage composition and physical properties due to stromelysin degradation. *Arthritis & Rheumatism: Official Journal of the American College of Rheumatology* 38, 173-183.
- Bonassar, L.J., Stinn, J.L., Pagnio, C.G., Frank, E.H., Moore, V.L., Lark, M.W., Sandy, J.D., Hollander, A.P., Poole, A.R., Grodzinsky, A.J., 1996. Activation and inhibition of endogenous matrix metalloproteinases in articular cartilage: effects on composition and biophysical properties. *Archives of biochemistry and biophysics* 333, 359-367.

- Boocock, M., McNair, P., Cicuttini, F., Stuart, A., Sinclair, T., 2009. The short-term effects of running on the deformation of knee articular cartilage and its relationship to biomechanical loads at the knee. *Osteoarthritis and Cartilage* 17, 883-890.
- Borthakur, A., Wheaton, A., Charagundla, S.R., Shapiro, E.M., Regatte, R.R., Akella, S.V., Kneeland, J.B., Reddy, R., 2003. Three-dimensional T1 ρ -weighted MRI at 1.5 Tesla. *Journal of Magnetic Resonance Imaging* 17, 730-736.
- Boschetti, F., Pennati, G., Gervaso, F., Peretti, G.M., Dubini, G., 2004. Biomechanical properties of human articular cartilage under compressive loads. *Biorheology* 41, 159-166.
- Bureau of Labor Statistics, U.S.D.o.L., 2016. Sports and exercise among Americans. *The Economics Daily*.
- Buschmann, M.D., Gluzband, Y.A., Grodzinsky, A.J., Hunziker, E.B., 1995. Mechanical compression modulates matrix biosynthesis in chondrocyte/agarose culture. *Journal of Cell Science* 108, 1497-1508.
- Callaghan, J.J., Insall, J.N., Greenwald, A.S., Dennis, D.A., Komistek, R.D., Murray, D.W., Bourne, R.B., Rorabeck, C.H., Dorr, L.D., 2000. Mobile-bearing knee replacement: concepts and results. *JBJS* 82, 1020-1041.
- Carballido-Gamio, J., Blumenkrantz, G., Lynch, J.A., Link, T.M., Majumdar, S., 2010. Longitudinal analysis of MRI T2 knee cartilage laminar organization in a subset of patients from the osteoarthritis initiative. *Magnetic Resonance in Medicine: An Official Journal of the International Society for Magnetic Resonance in Medicine* 63, 465-472.
- Carter, T.E., Taylor, K.A., Spritzer, C.E., Utturkar, G.M., Taylor, D.C., Moorman, C.T., Garrett, W.E., Guilak, F., McNulty, A.L., DeFrate, L.E., 2015. In vivo cartilage strain increases following medial meniscal tear and correlates with synovial fluid matrix metalloproteinase activity. *Journal of Biomechanics* 48, 1461-1468.
- Chan, D.D., Cai, L., Butz, K.D., Trippel, S.B., Nauman, E.A., Neu, C.P., 2016. In vivo articular cartilage deformation: noninvasive quantification of intratissue strain during joint contact in the human knee. *Scientific reports* 6, 19220.
- Chen, A., Bae, W., Schinagl, R., Sah, R., 2001. Depth- and strain-dependent mechanical and electromechanical properties of full-thickness bovine articular cartilage in confined compression. *Journal of biomechanics* 34, 1-12.
- Cher, W.L., Utturkar, G.M., Spritzer, C.E., Nunley, J.A., DeFrate, L.E., Collins, A.T., 2016. An analysis of changes in in vivo cartilage thickness of the healthy ankle following dynamic activity. *Journal of Biomechanics*.

- Chin, H.C., Khayat, G., Quinn, T.M., 2011. Improved characterization of cartilage mechanical properties using a combination of stress relaxation and creep. *Journal of Biomechanics* 44, 198-201.
- Cohen, J., 1962. The statistical power of abnormal-social psychological research: a review. *The Journal of Abnormal and Social Psychology* 65, 145.
- Coleman, J.L., Widmyer, M.R., Leddy, H.A., Utturkar, G.M., Spritzer, C.E., Moorman, C.T., Guilak, F., DeFrate, L.E., 2013. Diurnal variations in articular cartilage thickness and strain in the human knee. *Journal of Biomechanics* 46, 541-547.
- Collins, A.T., Hatcher, C., Kim, S., Ziemian, S., Spritzer, C., Guilak, F., DeFrate, L., McNulty, A., 2018a. Selective enzymatic digestion of proteoglycans and collagens alters cartilage T1rho and T2 relaxation times. *Annals of biomedical engineering*, 1-12.
- Collins, A.T., Kulvaranon, M.L., Cutcliffe, H.C., Utturkar, G.M., Smith, W.A., Spritzer, C.E., Guilak, F., DeFrate, L.E., 2018b. Obesity alters the in vivo mechanical response and biochemical properties of cartilage as measured by MRI. *Arthritis Research & Therapy* 20, 232.
- Collins, D., McElligott, T., 1960. Sulphate (35SO_4) uptake by chondrocytes in relation to histological changes in osteo-arthritic human articular cartilage. *Annals of the rheumatic diseases* 19, 318.
- Comets, E., Lavenu, A., Lavielle, M., 2017. Parameter estimation in nonlinear mixed effect models using saemix, and R implementation of the SAEM algorithm. *Journal of Statistical Software* 80, 1-41.
- Cowin, S.C., Doty, S.B., 2007. *Tissue mechanics*. Springer Science & Business Media.
- Cutcliffe, H.C., Davis, K.M., Spritzer, C.E., DeFrate, L.E., In Prep. In vivo Cartilage Strain and Recovery After 30 Minutes of Walking.
- Cutcliffe, H.C., DeFrate, L.E., In Review. Comparison of Cartilage Mechanical Properties Measured During Creep and Recovery. *Scientific Reports*.
- David-Vaudey, E., Ghosh, S., Ries, M., Majumdar, S., 2004. T2 relaxation time measurements in osteoarthritis. *Magnetic resonance imaging* 22, 673-682.
- DeFrate, L.E., 2017. Effects of ACL graft placement on in vivo knee function and cartilage thickness distributions. *Journal of Orthopaedic Research* 35, 1160-1170.
- Doyran, B., Tong, W., Li, Q., Jia, H., Zhang, X., Chen, C., Enomoto-Iwamoto, M., Lu, X.L., Qin, L., Han, L., 2017. Nanoindentation modulus of murine cartilage: a sensitive indicator of the initiation and progression of post-traumatic osteoarthritis. *Osteoarthritis and cartilage* 25, 108-117.

- Dunn, T.C., Lu, Y., Jin, H., Ries, M.D., Majumdar, S., 2004. T2 relaxation time of cartilage at MR imaging: comparison with severity of knee osteoarthritis. *Radiology* 232, 592-598.
- Duvvuri, U., Kudchodkar, S., Reddy, R., Leigh, J., 2002. T1 ρ relaxation can assess longitudinal proteoglycan loss from articular cartilage in vitro. *Osteoarthritis and cartilage* 10, 838-844.
- Duvvuri, U., Reddy, R., Patel, S.D., Kaufman, J.H., Kneeland, J.B., Leigh, J.S., 1997. T1 ρ -relaxation in articular cartilage: Effects of enzymatic degradation. *Magnetic resonance in medicine* 38, 863-867.
- Eckstein, F., Lemberger, B., Gratzke, C., Hudelmaier, M., Glaser, C., Englmeier, K., Reiser, M., 2005. In vivo cartilage deformation after different types of activity and its dependence on physical training status. *Annals of the Rheumatic Diseases* 64, 291-295.
- Eckstein, F., Lemberger, B., Stammberger, T., Englmeier, K., Reiser, M., 2000. Patellar cartilage deformation in vivo after static versus dynamic loading. *Journal of Biomechanics* 33, 819-825.
- Eckstein, F., Tieschky, M., Faber, S., Englmeier, K.-H., Reiser, M., 1999. Functional analysis of articular cartilage deformation, recovery, and fluid flow following dynamic exercise in vivo. *Anatomy and Embryology* 200, 419-424.
- Eckstein, F., Tieschky, M., Faber, S.C., Haubner, M., Kolem, H., Englmeier, K.-H., Reiser, M., 1998. Effect of physical exercise on cartilage volume and thickness in vivo: MR imaging study. *Radiology* 207, 243-248.
- Ettinger, W.H., Burns, R., Messier, S.P., Applegate, W., Rejeski, W.J., Morgan, T., Shumaker, S., Berry, M.J., O'toole, M., Monu, J., 1997. A randomized trial comparing aerobic exercise and resistance exercise with a health education program in older adults with knee osteoarthritis: the Fitness Arthritis and Seniors Trial (FAST). *JAMA* 277, 25-31.
- Ewers, B., Dvoracek-Driksna, D., Orth, M., Haut, R., 2001. The extent of matrix damage and chondrocyte death in mechanically traumatized articular cartilage explants depends on rate of loading. *Journal of Orthopaedic Research* 19, 779-784.
- Focht, B.C., 2006. Effectiveness of exercise interventions in reducing pain symptoms among older adults with knee osteoarthritis: a review. *Journal of Aging and Physical Activity* 14, 212-235.
- Fromson, M.I., Ratcliffe, A., Gardner, T.R., Mow, V.C., 1997. Differences in patellofemoral joint cartilage material properties and their significance to the etiology of cartilage surface fibrillation. *Osteoarthritis and Cartilage* 5, 377-386.

- Gabbard, C., Hart, S., 1996. A question of foot dominance. *The Journal of general psychology* 123, 289-296.
- Gao, L.-L., Qin, X.-Y., Zhang, C.-Q., Gao, H., Ge, H.-Y., Zhang, X.-Z., 2015. Ratcheting behavior of articular cartilage under cyclic unconfined compression. *Materials Science and Engineering: C* 57, 371-377.
- Glyn-Jones, S., Palmer, A., Agricola, R., Price, A., Vincent, T., Weinans, H., Carr, A., 2015. Osteoarthritis. *The Lancet* 386, 376-387.
- Grenier, S., Bhargava, M.M., Torzilli, P.A., 2014. An in vitro model for the pathological degradation of articular cartilage in osteoarthritis. *Journal of Biomechanics* 47, 645-652.
- Grodzinsky, F., Frank, E., 2011. *Fields, forces, and flows in biological systems*. Garland Science. Taylor & Francis Group, London & New York.
- Guermazi, A., Alizai, H., Crema, M., Trattnig, S., Regatte, R., Roemer, F., 2015. Compositional MRI techniques for evaluation of cartilage degeneration in osteoarthritis. *Osteoarthritis and cartilage* 23, 1639-1653.
- Guilak, F., 2011. Biomechanical factors in osteoarthritis. *Best Practice & Research Clinical Rheumatology* 25, 815-823.
- Guilak, F., Ratcliffe, A., Mow, V.C., 1995. Chondrocyte deformation and local tissue strain in articular cartilage: a confocal microscopy study. *Journal of Orthopaedic Research* 13, 410-421.
- Guo, X.E., Lu, H.H., Likhitpanichkul, M., Mow, V.C., 2003. The role of biomechanics in functional tissue engineering for articular cartilage, *Frontiers in Biomedical Engineering*. Springer, pp. 37-60.
- Gupta, R., Virayavanich, W., Kuo, D., Su, F., Link, T., Ma, B., Li, X., 2014. MR T1 ρ quantification of cartilage focal lesions in acutely injured knees: correlation with arthroscopic evaluation. *Magnetic resonance imaging* 32, 1290-1296.
- Hannila, I., Räänä, S.S., Tervonen, O., Ojala, R., Nieminen, M., 2009. Topographical variation of T2 relaxation time in the young adult knee cartilage at 1.5 T. *Osteoarthritis and cartilage* 17, 1570-1575.
- Harkey, M., Blackburn, J., Davis, H., Sierra-Arévalo, L., Nissman, D., Pietrosimone, B., 2017. Ultrasonographic assessment of medial femoral cartilage deformation acutely following walking and running. *Osteoarthritis and cartilage* 25, 907-913.
- Harkey, M.S., Blackburn, J.T., Hackney, A.C., Lewek, M.D., Schmitz, R.J., Nissman, D., Pietrosimone, B., 2018. Comprehensively assessing the acute femoral cartilage

- response and recovery after walking and drop-landing: an ultrasonographic study. *Ultrasound in medicine & biology* 44, 311-320.
- Hatcher, C.C., Collins, A.T., Kim, S.Y., Michel, L.C., Mostertz, W.C., Ziemian, S.N., Spritzer, C.E., Guilak, F., DeFrate, L.E., McNulty, A.L., 2017. Relationship between T1rho magnetic resonance imaging, synovial fluid biomarkers, and the biochemical and biomechanical properties of cartilage. *Journal of Biomechanics* 55, 18-26.
- Heckelman, L.N., Smith, W.A., Riofrio, A.D., Collins, A.T., Gwynn, O.R., Utturkar, G.M., Spritzer, C.E., DeFrate, L.E., In Prep. Quantifying the Biochemical State of Knee Cartilage in Response to Running using T1rho Magnetic Resonance Imaging.
- Herzog, W., Diet, S., Suter, E., Mayzus, P., Leonard, T., Müller, C., Wu, J., Epstein, M., 1998. Material and functional properties of articular cartilage and patellofemoral contact mechanics in an experimental model of osteoarthritis. *Journal of Biomechanics* 31, 1137-1145.
- Hollander, A., Pidoux, I., Reiner, A., Rorabeck, C., Bourne, R., Poole, A.R., 1995. Damage to type II collagen in aging and osteoarthritis starts at the articular surface, originates around chondrocytes, and extends into the cartilage with progressive degeneration. *Journal of Clinical Investigation* 96, 2859.
- Hudelmaier, M., Glaser, C., Hohe, J., Englmeier, K.H., Reiser, M., Putz, R., Eckstein, F., 2001. Age-related changes in the morphology and deformational behavior of knee joint cartilage. *Arthritis & Rheumatology* 44, 2556-2561.
- Hurley, M., Scott, D., 1998. Improvements in quadriceps sensorimotor function and disability of patients with knee osteoarthritis following a clinically practicable exercise regime. *Rheumatology* 37, 1181-1187.
- Ihaka, R., Gentleman, R., 1996. R: a language for data analysis and graphics. *Journal of Computational and Graphical Statistics* 5, 299-314.
- Jurvelin, J., Buschmann, M., Hunziker, E., 2003. Mechanical anisotropy of the human knee articular cartilage in compression. *Proceedings of the Institution of Mechanical Engineers, Part H: Journal of Engineering in Medicine* 217, 215-219.
- Jurvelin, J., Kiviranta, I., Säämänen, A.M., Tammi, M., Helminen, H., 1989. Partial restoration of immobilization-induced softening of canine articular cartilage after remobilization of the knee (stifle) joint. *Journal of Orthopaedic Research* 7, 352-358.
- Jurvelin, J., Kiviranta, I., Tammi, M., Helminen, J., 1986. Softening of canine articular cartilage after immobilization of the knee joint. *Clinical Orthopaedics and Related Research* 207, 246-252.

- Keenan, K.E., Besier, T.F., Pauly, J.M., Han, E., Rosenberg, J., Smith, R.L., Delp, S.L., Beaupre, G.S., Gold, G.E., 2011. Prediction of glycosaminoglycan content in human cartilage by age, T1 ρ and T2 MRI. *Osteoarthritis and cartilage* 19, 171-179.
- Kellgren, J., Lawrence, J., 1957. Radiological assessment of osteo-arthrosis. *Annals of the Rheumatic Diseases* 16, 494.
- Kersting, U.G., Stubendorff, J.J., Schmidt, M.C., Brüggemann, G.-P., 2005. Changes in knee cartilage volume and serum COMP concentration after running exercise. *Osteoarthritis and cartilage* 13, 925-934.
- Kessler, M.A., Glaser, C., Tittel, S., Reiser, M., Imhoff, A.B., 2006. Volume changes in the menisci and articular cartilage of runners. *The American Journal of Sports Medicine* 34, 832-836.
- Kessler, M.A., Glaser, C., Tittel, S., Reiser, M., Imhoff, A.B., 2008. Recovery of the menisci and articular cartilage of runners after cessation of exercise Additional aspects of in vivo investigation based on 3-dimensional magnetic resonance imaging. *The American Journal of Sports Medicine* 36, 966-970.
- Knecht, S., Vanwanseele, B., Stüssi, E., 2006. A review on the mechanical quality of articular cartilage—implications for the diagnosis of osteoarthritis. *Clinical biomechanics* 21, 999-1012.
- Korhonen, R., Laasanen, M., Töyräs, J., Rieppo, J., Hirvonen, J., Helminen, H., Jurvelin, J., 2002. Comparison of the equilibrium response of articular cartilage in unconfined compression, confined compression and indentation. *Journal of Biomechanics* 35, 903-909.
- Kramer, P.A., Sylvester, A.D., 2012. Humans, geometric similarity and the Froude number: is “reasonably close” really close enough? *Biology Open*, BIO20122691.
- Lad, N.K., Liu, B., Ganapathy, P.K., Utturkar, G.M., Sutter, E.G., Moorman, C.T., 3rd, Garrett, W.E., Spritzer, C.E., DeFrate, L.E., 2016. Effect of normal gait on in vivo tibiofemoral cartilage strains. *Journal of Biomechanics* 49, 2870-2876.
- Lai, W.M., Rubin, D.H., Krempl, E., 1999. *Introduction to continuum mechanics*, 3rd ed. Butterworth-Heinemann.
- Larsson, T., Aspden, R.M., Heinegård, D., 1991. Effects of mechanical load on cartilage matrix biosynthesis in vitro. *Matrix* 11, 388-394.
- Lawrence, R.C., Felson, D.T., Helmick, C.G., Arnold, L.M., Choi, H., Deyo, R.A., Gabriel, S., Hirsch, R., Hochberg, M.C., Hunder, G.G., 2008. Estimates of the prevalence of arthritis and other rheumatic conditions in the United States: Part II. *Arthritis & Rheumatism* 58, 26-35.

- Lee, D.A., Bader, D.L., 1997. Compressive strains at physiological frequencies influence the metabolism of chondrocytes seeded in agarose. *Journal of Orthopaedic Research* 15, 181-188.
- Legare, A., Garon, M., Guardo, R., Savard, P., Poole, A., Buschmann, M., 2002. Detection and analysis of cartilage degeneration by spatially resolved streaming potentials. *Journal of orthopaedic research* 20, 819-826.
- Lewek, M.D., Rudolph, K.S., Snyder-Mackler, L., 2004. Quadriceps femoris muscle weakness and activation failure in patients with symptomatic knee osteoarthritis. *Journal of Orthopaedic Research* 22, 110-115.
- Li, X., Cheng, J., Lin, K., Saadat, E., Bolbos, R.I., Jobke, B., Ries, M.D., Horvai, A., Link, T.M., Majumdar, S., 2011a. Quantitative MRI using T1 ρ and T2 in human osteoarthritic cartilage specimens: correlation with biochemical measurements and histology. *Magnetic resonance imaging* 29, 324-334.
- Li, X., Kuo, D., Theologis, A., Carballido-Gamio, J., Stehling, C., Link, T.M., Ma, C.B., Majumdar, S., 2011b. Cartilage in anterior cruciate ligament-reconstructed knees: MR imaging T1 ρ and T2—initial experience with 1-year follow-up. *Radiology* 258, 505-514.
- Li, X., Ma, B., Thomas, L., Castillo, D., Blumenkrantz, G., Lozano, J., Carballido-Gamio, J., Ries, M., Majumdar, S., 2007. In vivo T1 ρ and T2 mapping of articular cartilage in osteoarthritis of the knee using 3 tesla MRI. *Osteoarthritis Cartilage* 15, 789-797.
- Li, X., Pai, A., Blumenkrantz, G., Carballido-Gamio, J., Link, T., Ma, B., Ries, M., Majumdar, S., 2009. Spatial distribution and relationship of T1 ρ and T2 relaxation times in knee cartilage with osteoarthritis. *Magnetic resonance in medicine* 61, 1310-1318.
- Litwic, A., Edwards, M.H., Dennison, E.M., Cooper, C., 2013. Epidemiology and burden of osteoarthritis. *British medical bulletin*, lds038.
- Liu, B., Lad, N.K., Collins, A.T., Ganapathy, P.K., Utturkar, G.M., McNulty, A.L., Spritzer, C.E., Moorman III, C.T., Sutter, E.G., Garrett, W.E., 2017. In vivo tibial cartilage strains in regions of cartilage-to-cartilage contact and cartilage-to-meniscus contact in response to walking. *The American journal of sports medicine* 45, 2817-2823.
- Loeser, R.F., Goldring, S.R., Scanzello, C.R., Goldring, M.B., 2012. Osteoarthritis: a disease of the joint as an organ. *Arthritis & Rheumatism* 64, 1697-1707.

- Lorenz, H., Richter, W., 2006. Osteoarthritis: cellular and molecular changes in degenerating cartilage. *Progress in Histochemistry and Cytochemistry* 40, 135-163.
- Lu, X., Mow, V., 2008. Biomechanics of articular cartilage and determination of material properties. *Medicine+ Science in Sports+ Exercise* 40, 193.
- Mak, A., Lai, W., Mow, V., 1987. Biphasic indentation of articular cartilage—I. Theoretical analysis. *Journal of Biomechanics* 20, 703-714.
- Mansour, J.M., 2003. Biomechanics of cartilage. *Kinesiology: the mechanics and pathomechanics of human movement*, 66-79.
- Matzat, S.J., van Tiel, J., Gold, G.E., Oei, E.H., 2013. Quantitative MRI techniques of cartilage composition. *Quantitative imaging in medicine and surgery* 3, 162.
- Mauck, R.L., Soltz, M.A., Wang, C.C., Wong, D.D., Chao, P.-H.G., Valhmu, W.B., Hung, C.T., Ateshian, G.A., 2000. Functional tissue engineering of articular cartilage through dynamic loading of chondrocyte-seeded agarose gels. *Journal of Biomechanical Engineering* 122, 252-260.
- Maurer, B.T., Stern, A.G., Kinossian, B., Cook, K.D., Schumacher, H.R., 1999. Osteoarthritis of the knee: isokinetic quadriceps exercise versus an educational intervention. *Archives of physical medicine and rehabilitation* 80, 1293-1299.
- Menezes, N.M., Gray, M.L., Hartke, J.R., Burstein, D., 2004. T2 and T1 ρ MRI in articular cartilage systems. *Magnetic resonance in medicine* 51, 503-509.
- Michaud, C.M., McKenna, M.T., Begg, S., Tomijima, N., Majmudar, M., Bulzacchelli, M.T., Ebrahim, S., Ezzati, M., Salomon, J.A., Kreiser, J.G., 2006. The burden of disease and injury in the United States 1996. *Population health metrics* 4, 1.
- Milentijevic, D., Torzilli, P.A., 2005. Influence of stress rate on water loss, matrix deformation and chondrocyte viability in impacted articular cartilage. *Journal of Biomechanics* 38, 493-502.
- Miller, G.J., Morgan, E.F., 2010. Use of microindentation to characterize the mechanical properties of articular cartilage: comparison of biphasic material properties across length scales. *Osteoarthritis and Cartilage* 18, 1051-1057.
- Mosher, T.J., Liu, Y., Torok, C.M., 2010. Functional cartilage MRI T2 mapping: evaluating the effect of age and training on knee cartilage response to running. *Osteoarthritis and cartilage* 18, 358-364.
- Mow, V.C., Gibbs, M., Lai, W.M., Zhu, W., Athanasiou, K.A., 1989. Biphasic indentation of articular cartilage—II. A numerical algorithm and an experimental study. *Journal of Biomechanics* 22, 853-861.

- Mow, V.C., Guo, X.E., 2002. Mechano-electrochemical properties of articular cartilage: their inhomogeneities and anisotropies. *Annual Review of Biomedical Engineering* 4, 175-209.
- Mow, V.C., Holmes, M.H., Lai, W.M., 1984. Fluid transport and mechanical properties of articular cartilage: a review. *Journal of Biomechanics* 17, 377-394.
- Mow, V.C., Huiskes, R., 2005. *Basic Orthopaedic Biomechanics & Mechano-biology*. Lippincott Williams & Wilkins.
- Mow, V.C., Kuei, S., Lai, W.M., Armstrong, C.G., 1980. Biphasic creep and stress relaxation of articular cartilage in compression: theory and experiments. *Journal of Biomechanical Engineering* 102, 73-84.
- Murphy, L., Helmick, C.G., 2012. The impact of osteoarthritis in the United States: a population-health perspective: A population-based review of the fourth most common cause of hospitalization in US adults. *Orthopaedic Nursing* 31, 85-91.
- Murphy, L., Schwartz, T.A., Helmick, C.G., Renner, J.B., Tudor, G., Koch, G., Dragomir, A., Kalsbeek, W.D., Luta, G., Jordan, J.M., 2008. Lifetime risk of symptomatic knee osteoarthritis. *Arthritis Care & Research: Official Journal of the American College of Rheumatology* 59, 1207-1213.
- Nia, H.T., Han, L., Li, Y., Ortiz, C., Grodzinsky, A., 2011. Poroelasticity of cartilage at the nanoscale. *Biophysical journal* 101, 2304-2313.
- Niehoff, A., Müller, M., Brüggemann, L., Savage, T., Zaucke, F., Eckstein, F., Müller-Lung, U., Brüggemann, G.-P., 2011. Deformational behaviour of knee cartilage and changes in serum cartilage oligomeric matrix protein (COMP) after running and drop landing. *Osteoarthritis and Cartilage* 19, 1003-1010.
- Nieminen, M.T., Rieppo, J., Töyräs, J., Hakumäki, J.M., Silvennoinen, J., Hyttinen, M.M., Helminen, H.J., Jurvelin, J.S., 2001. T2 relaxation reveals spatial collagen architecture in articular cartilage: a comparative quantitative MRI and polarized light microscopic study. *Magnetic Resonance in Medicine: An Official Journal of the International Society for Magnetic Resonance in Medicine* 46, 487-493.
- Nilsson, J., Thorstensson, A., 1989. Ground reaction forces at different speeds of human walking and running. *Acta Physiologica* 136, 217-227.
- Nishimura, D.G., 2010. *Principles of magnetic resonance imaging*. Stanford Univ.
- Nishioka, H., Hirose, J., Nakamura, E., Okamoto, N., Karasugi, T., Taniwaki, T., Okada, T., Yamashita, Y., Mizuta, H., 2013. Detecting ICRS grade 1 cartilage lesions in anterior cruciate ligament injury using T1 ρ and T2 mapping. *European journal of radiology* 82, 1499-1505.

- Nishioka, H., Hirose, J., Nakamura, E., Oniki, Y., Takada, K., Yamashita, Y., Mizuta, H., 2012. T1 ρ and T2 mapping reveal the in vivo extracellular matrix of articular cartilage. *Journal of Magnetic Resonance Imaging* 35, 147-155.
- O'Reilly, S.C., Jones, A., Muir, K.R., Doherty, M., 1998. Quadriceps weakness in knee osteoarthritis: the effect on pain and disability. *Annals of the rheumatic diseases* 57, 588-594.
- Okafor, E.C., Utturkar, G.M., Widmyer, M.R., Abebe, E.S., Collins, A.T., Taylor, D.C., Spritzer, C.E., Moorman 3rd, C., Garrett, W.E., DeFrate, L.E., 2014. The effects of femoral graft placement on cartilage thickness after anterior cruciate ligament reconstruction. *Journal of Biomechanics* 47, 96-101.
- Owusu-Akyaw, K.A., Heckelman, L.N., Cutcliffe, H.C., Sutter, E.G., Englander, Z.A., Spritzer, C.E., Garrett, W.E., DeFrate, L.E., 2018. A comparison of patellofemoral cartilage morphology and deformation in anterior cruciate ligament deficient versus uninjured knees. *Journal of biomechanics* 67, 78-83.
- Paranjape, C.S., Cutcliffe, H.C., Grambow, S.C., Utturkar, G.M., Collins, A.T., Garrett, W.E., Spritzer, C.E., DeFrate, L.E., 2019. A New Stress Test for Knee Joint Cartilage. *Scientific Reports* 9, 2283.
- Park, S., Krishnan, R., Nicoll, S.B., Ateshian, G.A., 2003. Cartilage interstitial fluid load support in unconfined compression. *Journal of biomechanics* 36, 1785-1796.
- Peterfy, C., Guermazi, A., Zaim, S., Tirman, P., Miaux, Y., White, D., Kothari, M., Lu, Y., Fye, K., Zhao, S., 2004. Whole-organ magnetic resonance imaging score (WORMS) of the knee in osteoarthritis. *Osteoarthritis and Cartilage* 12, 177-190.
- Quinn, T., Allen, R., Schalet, B., Perumbuli, P., Hunziker, E., 2001. Matrix and cell injury due to sub-impact loading of adult bovine articular cartilage explants: effects of strain rate and peak stress. *Journal of Orthopaedic Research* 19, 242-249.
- Regatte, R.R., Akella, S.V., Borthakur, A., Reddy, R., 2003. Proton spin-lock ratio imaging for quantitation of glycosaminoglycans in articular cartilage. *Journal of Magnetic Resonance Imaging: An Official Journal of the International Society for Magnetic Resonance in Medicine* 17, 114-121.
- Rivers, P., Rosenwasser, M., Mow, V., Pawluk, R., Strauch, R., Sugalski, M., Ateshian, G., 2000. Osteoarthritic changes in the biochemical composition of thumb carpometacarpal joint cartilage and correlation with biomechanical properties. *Journal of Hand Surgery* 25, 889-898.
- Roberts, S., Weightman, B., Urban, J., Chappell, D., 1986. Mechanical and biochemical properties of human articular cartilage in osteoarthritic femoral heads and in

- autopsy specimens. *The Journal of bone and joint surgery. British* volume 68, 278-288.
- Roos, E.M., Dahlberg, L., 2005. Positive effects of moderate exercise on glycosaminoglycan content in knee cartilage: A four-month, randomized, controlled trial in patients at risk of osteoarthritis. *Arthritis & Rheumatology* 52, 3507-3514.
- Sah, R.L., Yang, A.S., Chen, A.C., Hant, J.J., Halili, R.B., Yoshioka, M., Amiel, D., Coutts, R.D., 1997. Physical properties of rabbit articular cartilage after transection of the anterior cruciate ligament. *Journal of Orthopaedic Research* 15, 197-203.
- Sah, R.L.Y., Kim, Y.J., Doong, J.Y.H., Grodzinsky, A.J., Plass, A.H., Sandy, J.D., 1989. Biosynthetic response of cartilage explants to dynamic compression. *Journal of Orthopaedic Research* 7, 619-636.
- Salaffi, F., Carotti, M., Stancati, A., Grassi, W., 2005. Health-related quality of life in older adults with symptomatic hip and knee osteoarthritis: a comparison with matched healthy controls. *Aging clinical and experimental research* 17, 255-263.
- Schinagl, R.M., Gurskis, D., Chen, A.C., Sah, R.L., 1997. Depth-dependent confined compression modulus of full-thickness bovine articular cartilage. *Journal of Orthopaedic Research* 15, 499-506.
- Setton, L., Mow, V., Müller, F., Pita, J., Howell, D., 1994. Mechanical properties of canine articular cartilage are significantly altered following transection of the anterior cruciate ligament. *Journal of Orthopaedic Research* 12, 451-463.
- Setton, L.A., Zhu, W., Mow, V.C., 1993. The biphasic poroviscoelastic behavior of articular cartilage: role of the surface zone in governing the compressive behavior. *Journal of Biomechanics* 26, 581-592.
- Shelton, J.C., Bader, D.L., Lee, D.A., 2003. Mechanical conditioning influences the metabolic response of cell-seeded constructs. *Cells Tissues Organs* 175, 140-150.
- Slemenda, C., Brandt, K.D., Heilman, D.K., Mazzuca, S., Braunstein, E.M., Katz, B.P., Wolinsky, F.D., 1997. Quadriceps weakness and osteoarthritis of the knee. *Annals of internal medicine* 127, 97-104.
- Soltz, M.A., Ateshian, G.A., 1998. Experimental verification and theoretical prediction of cartilage interstitial fluid pressurization at an impermeable contact interface in confined compression. *Journal of Biomechanics* 31, 927-934.
- Soltz, M.A., Ateshian, G.A., 2000. Interstitial fluid pressurization during confined compression cyclical loading of articular cartilage. *Annals of biomedical engineering* 28, 150-159.

- Sophia Fox, A.J., Bedi, A., Rodeo, S.A., 2009. The basic science of articular cartilage: structure, composition, and function. *Sports health* 1, 461-468.
- Souza, R., Stehling, C., Wyman, B., Le Graverand, M.-P.H., Li, X., Link, T., Majumdar, S., 2010. The effects of acute loading on T1rho and T2 relaxation times of tibiofemoral articular cartilage. *Osteoarthritis and cartilage* 18, 1557-1563.
- Souza, R.B., Feeley, B.T., Zarins, Z.A., Link, T.M., Li, X., Majumdar, S., 2013. T1rho MRI relaxation in knee OA subjects with varying sizes of cartilage lesions. *The knee* 20, 113-119.
- Stahl, R., Luke, A., Li, X., Carballido-Gamio, J., Ma, C.B., Majumdar, S., Link, T.M., 2009. T1rho, T2 and focal knee cartilage abnormalities in physically active and sedentary healthy subjects versus early OA patients—a 3.0-Tesla MRI study. *European radiology* 19, 132-143.
- Stolberg-Stolberg, J., Foehr, P., Pflieger, I., Kuntz, L., von Deimling, C., Obermeier, A., Prodinger, P.M., Grosse, C.U., Burgkart, R., 2018. Analysis of Cartilage Creep Recovery Using a Highly Dynamic Closed-loop Test System. *Journal of Bionic Engineering* 15, 1057-1066.
- Suh, J.-K., Li, Z., Woo, S.L., 1995. Dynamic behavior of a biphasic cartilage model under cyclic compressive loading. *Journal of biomechanics* 28, 357-364.
- Sun, H.B., 2010. Mechanical loading, cartilage degradation, and arthritis. *Annals of the New York Academy of Sciences* 1211, 37-50.
- Sutter, E.G., Liu, B., Utturkar, G.M., Widmyer, M.R., Spritzer, C.E., Cutcliffe, H.C., Englander, Z.A., Goode, A.P., Garrett Jr, W.E., DeFrate, L.E., 2019. Effects of anterior cruciate ligament deficiency on tibiofemoral cartilage thickness and strains in response to hopping. *The American Journal of Sports Medicine*, 0363546518802225.
- Sutter, E.G., Widmyer, M.R., Utturkar, G.M., Spritzer, C.E., Garrett, W.E., DeFrate, L.E., 2015. In vivo measurement of localized tibiofemoral cartilage strains in response to dynamic activity. *The American Journal of Sports Medicine* 43, 370-376.
- Taylor, C., Carballido-Gamio, J., Majumdar, S., Li, X., 2009. Comparison of quantitative imaging of cartilage for osteoarthritis: T2, T1 ρ , dGEMRIC and contrast-enhanced computed tomography. *Magnetic resonance imaging* 27, 779-784.
- Taylor, K.A., Collins, A.T., Heckelman, L.N., Kim, S.Y., Utturkar, G.M., Spritzer, C.E., Garrett, W.E., DeFrate, L.E., 2018. Activities of daily living influence tibial cartilage T1rho relaxation times. *Journal of biomechanics* 82, 228-233.
- Teng, H.-L., Calixto, N., MacLeod, T., Nardo, L., Link, T., Majumdar, S., Souza, R., 2016. Associations between patellofemoral joint cartilage T1 ρ and T2 and knee flexion

- moment and impulse during gait in individuals with and without patellofemoral joint osteoarthritis. *Osteoarthritis and cartilage* 24, 1554-1564.
- Thompson, R., Oegema, T., 1979. Metabolic activity of articular cartilage in osteoarthritis. An in vitro study. *J Bone Joint Surg Am* 61, 407-416.
- Treppo, S., Koepp, H., Quan, E.C., Cole, A.A., Kuettner, K.E., Grodzinsky, A.J., 2000. Comparison of biomechanical and biochemical properties of cartilage from human knee and ankle pairs. *Journal of Orthopaedic Research* 18, 739-748.
- Utturkar, G., Iribarra, L., Taylor, K., Spritzer, C., Taylor, D., Garrett, W., DeFrate, L.E., 2013. The effects of a valgus collapse knee position on in vivo ACL elongation. *Annals of biomedical engineering* 41, 123-130.
- Van Baar, M.E., Dekker, J., Oostendorp, R., Bijl, D., Voorn, T.B., 1998. The effectiveness of exercise therapy in patients with osteoarthritis of the hip or knee: A randomized clinical trial. *The Journal of Rheumatology* 25, 12.
- Van de Velde, S.K., Bingham, J.T., Hosseini, A., Kozanek, M., DeFrate, L.E., Gill, T.J., Li, G., 2009. Increased tibiofemoral cartilage contact deformation in patients with anterior cruciate ligament deficiency. *Arthritis & Rheumatism* 60, 3693-3702.
- Van Ginckel, A., Roosen, P., Almqvist, K., Verstraete, K., Witvrouw, E., 2011. Effects of in vivo exercise on ankle cartilage deformation and recovery in healthy volunteers: an experimental study. *Osteoarthritis and Cartilage* 19, 1123-1131.
- Van Ginckel, A., Verdonk, P., Victor, J., Witvrouw, E., 2013. Cartilage status in relation to return to sports after anterior cruciate ligament reconstruction. *The American Journal of Sports Medicine* 41, 550-559.
- Van Manen, M.D., Nace, J., Mont, M.A., 2012. Management of primary knee osteoarthritis and indications for total knee arthroplasty for general practitioners. *The Journal of the American Osteopathic Association* 112, 709-715.
- Waterton, J.C., Solloway, S., Foster, J.E., Keen, M.C., Gandy, S., Middleton, B.J., Maciewicz, R.A., Watt, I., Dieppe, P.A., Taylor, C.J., 2000. Diurnal variation in the femoral articular cartilage of the knee in young adult humans. *Magnetic resonance in medicine* 43, 126-132.
- Wayne, J.S., Kraft, K.A., Shields, K.J., Yin, C., Owen, J.R., Disler, D.G., 2003. MR imaging of normal and matrix-depleted cartilage: correlation with biomechanical function and biochemical composition. *Radiology* 228, 493-499.
- Widmyer, M.R., Utturkar, G.M., Leddy, H.A., Coleman, J.L., Spritzer, C.E., Moorman, C.T., DeFrate, L.E., Guilak, F., 2013. High body mass index is associated with increased diurnal strains in the articular cartilage of the knee. *Arthritis & Rheumatism* 65, 2615-2622.

- Wirth, W., Le Graverand, M.-P.H., Wyman, B.T., Maschek, S., Hudelmaier, M., Hitzl, W., Nevitt, M., Eckstein, F., Group, O.I., 2009. Regional analysis of femorotibial cartilage loss in a subsample from the Osteoarthritis Initiative progression subcohort. *Osteoarthritis and Cartilage* 17, 291-297.
- Yuan, X., Meng, H., Wang, Y., Peng, J., Guo, Q., Wang, A., Lu, S., 2014. Bone–cartilage interface crosstalk in osteoarthritis: potential pathways and future therapeutic strategies. *Osteoarthritis and Cartilage* 22, 1077-1089.

Biography

Hattie Christine Cutcliffe grew up in Denver, Colorado where she attended Lakewood High School, earning an International Baccalaureate diploma in 2007. As an avid fan of athletics, Hattie participated extensively in gymnastics and track prior to college, and was a cheerleader at Duke University for four years as an undergraduate. Her lifelong love of athletics and interest in the biomechanical factors relating to sports injuries led her to pursue degrees in Biomedical Engineering, beginning with her Bachelor's degree (2007-2011) and culminating in her Doctor of Philosophy degree (2011-2019).

EDUCATION

Duke University, Durham, NC

Ph.D. Biomedical Engineering	December 2019
M.S. Biomedical Engineering	December 2015
B.S.E. Biomedical Engineering	May 2011

PUBLISHED JOURNAL ARTICLES (PEER-REVIEWED)

Cutcliffe HC*, Paranjape CS* (*co-first authors), Grambow SC, Utturkar GM, Collins AT, Garrett WE, Spritzer CE, DeFrate LE (2019). A new stress test for knee joint cartilage. *Nature Scientific Reports* 9:2283 DOI: 10.1038/s41598-018-38104-2.

Cutcliffe HC, Schmidt AL, Lucas JE, Bass CR (2012). How Few? Bayesian statistics in injury biomechanics. *Stapp Car Crash Journal* 56:349-386.

- Englander ZA, **Cutcliffe HC**, Utturkar GM, Taylor KA, Spritzer CE, Garrett WE, DeFrate LE (2019). In vivo assessment of the interaction of patellar tendon tibial shaft angle and anterior cruciate ligament elongation during flexion. *Journal of Biomechanics* 90:123-127. DOI: <https://doi.org/10.1016/j.jbiomech.2019.04.034>
- Englander ZA, **Cutcliffe HC**, Utturkar GM, Garrett WE, Spritzer CE, DeFrate LE (2019). A comparison of knee abduction angles measured by a 3D anatomic coordinate system versus videographic analysis. *The Orthopaedic Journal of Sports Medicine* DOI: 10.1177/2325967118819831.
- Dibb AT, **Cutcliffe HC**, Luck JF, Cox CA, Myers BS, Bass CR, Arbogast KB, Seacrist T, Nightingale RW (2014). Pediatric head and neck dynamics in frontal impact: Analysis of important mechanical factors and proposed neck performance corridors for six and ten year old ATDs. *Traffic Injury Prevention* 15(4):386-394.
- Rafaels KA, **Cutcliffe HC**, Salzar RS, Davis M, Boggess B, Bush B, Harris R, Rountree MS, Sanderson TE, Campman S, Koch S, Bass CR (2014). Injuries of the head from backface deformation of ballistic protective helmets under ballistic impact. *Journal of Forensic Sciences* DOI: 10.1111/1556-4029.12570.
- Taylor KA, **Cutcliffe HC**, Queen RM, Utturkar GM, Spritzer CE, Garrett WE, DeFrate LE (2013). In vivo measurement of ACL length and relative strain during walking. *Journal of Biomechanics* 46(3):478-483.
- Collins AT, Kulvaranon ML, **Cutcliffe HC**, Utturkar GM, Smith WAR, Spritzer CE, Guilak F, DeFrate LE (2018). Obesity alters the in vivo mechanical response and biochemical properties of cartilage as measured by MRI. *Arthritis Research & Therapy* 20(1):232 DOI: 10.1186/s13075-018-1727-4.
- Eckersley CP, White TR, **Cutcliffe HC**, Shridharani JK, Wood GW, Bass CR (2018). Foul tip impact attenuation of baseball catcher masks using head impact metrics. *PLOS One* 6(13):e0198316.

- Owusu-Akyaw KA, Heckelman LN, **Cutcliffe HC**, Sutter EG, Englander ZA, Spritzer CE, Garrett WE, DeFrate LE (2018). A comparison of patellofemoral cartilage morphology and deformation in anterior cruciate ligament deficient versus uninjured knees. *Journal of Biomechanics* 67:78-83.
- Nightingale RW, Sganga J, **Cutcliffe HC**, Bass CR (2016). Impact responses of the cervical spine: The effects of muscle activity, torso constraint, and initial position. *Journal of Biomechanics* 49:558-564.
- Lloyd AM, Nightingale RW, Luck JF, Bass CR, **Cutcliffe HC**, Myers BS (2019). The response of the pediatric head to impacts onto a rigid surface. *Journal of Biomechanics* 93:167-176.
- Kuo C, Wu LC, Hammor BT, Luck JF, **Cutcliffe HC**, Lynall RC, Kait JR, Campbell KR, Mihalik JP, Bass CR, Camarillo DB (2016). Effect of the mandible on mouthguard measurements of head kinematics. *Journal of Biomechanics* 49:1845-1853.
- Lloyd AM, Nightingale RW, Song Y, Luck JF, **Cutcliffe HC**, Myers BS, Bass CR (2014). The response of the adult and ATD heads to impacts onto a rigid surface. *Accident Analysis & Prevention* 72:219-229.
- Dibb AT, Cox CA, Nightingale RW, Luck JF, **Cutcliffe HC**, Myers BS, Arbogast KB, Seacrist T, Bass CR (2013). Importance of muscle activation for biofidelic pediatric neck response. *Traffic Injury Prevention* 14(Sup 1):S116-S127.
- Kwak YH, Barrientos T, Furman B, Zhang H, Puvindran V, **Cutcliffe HC**, Herfarth J, Nwankwo E, Alman BA (2019). Pharmacologic targeting of β -catenin improves fracture healing in old mice. *Nature Scientific Reports* 9:9005 DOI: 10.1038/s41598-019-45339-0.
- Sutter EG, Liu B, Utturkar GM, Widmyer MR, Spritzer CE, **Cutcliffe HC**, Englander ZA, Goode AP, Garrett WE, DeFrate LE (2018). Effects of anterior cruciate ligament deficiency on tibiofemoral cartilage thickness and strains in response to hopping. *The American Journal of Sports Medicine* 47(1):96-103. DOI: 10.1177/0363546518802225.

Loyd AM, Nightingale RW, Luck JF, Song Y, Fronheiser L, **Cutcliffe HC**, Myers BS, Bass CR (2015). The compressive stiffness of human pediatric heads. *Journal of Biomechanics* 48:3766-3775.

HONORS

2016 Stansell-Klein-Gardner Duke TIP STEM Summer Fellowship

2013 Whitaker International Summer Grant Awardee

2013 National Science Foundation Graduate Research Fellowship—Honorable Mention

2012 Stapp Student Paper Award – 3rd place, 56th Stapp Car Crash Conference

2012-2013 James McElhaney Fellowship in BME from Duke University

2010-2011 Pratt Undergraduate Research Fellowship from Duke University